University of Trento – Italy

Department of Industrial Engineering

Preparation and characterization of $Cu_{2-x}Zn_{1+y}SnS_4$ for thin films solar cells

Doctoral School in Materials Science and Engineering

Ciclo XVIII: Renato D'Angelo Bandres

PREPARATION AND CHARACTERIZATION OF

$Cu_{2-X}Zn_{1+Y}SnS_4$ FOR THIN FILMS SOLAR CELLS

Renato D'Angelo Bandres

E-mail: r.dangelobandres@unitn.it

Advisor:

Prof. Matteo Leoni

Department of Civil, Environmental and Mechanical Engineering

University of Trento, Italy.

Provide by:

Prof. Paolo Scardi, Co-Advisor

Department of Civil, Environmental and Mechanical Engineering

University of Trento, Italy.

Ph.D. Commission:

Prof. Riccardo Ceccato,

Department of Industrial Engineering

University of Trento, Italy.

Prof. Giovanni Predieri,

Department of Chemical

University of Parma

Prof. Claudio Ferone,

Department of Engineering

University of Napoli Parthenope

University of Trento,

Department of Industrial Engineering

Doctoral Thesis

September 2016

ACKNOWLEDGMENTS

ABSTRACT

CZTS non-stoichiometric thin films [$Cu_{2-x}Zn_{1+x}SnS_4$)] for solar cells applications have been successfully deposited on glass substrates using two different types of synthesis and two effective deposition methods: dip-coating into a sol or drop-wise ink spin-coating. For dip-coating, a sol was prepared by mixing a solution of metal chlorides dissolved in methanol together with thiourea dissolved in ethylene glycol; tin chloride (either pentahydrate or anhydrous) was used as a tin source. The ink for spin-coating was prepared by hot-injection, starting from metal (copper, tin and zinc) chlorides like in the previous synthesis: the salts, dissolved in oleylamine, were heated at 130 °C, when a solution of pure sulfur in oleylamine was injected. The CZTS thin films samples from both methods have been recrystallized by two thermal treatments, respectively with and without an extra sulfur powder at 550 °C in Ar atmosphere. Treatment duration was shown to affect both structure and microstructure of CZTS coatings. Moreover, the optical properties of the final absorbing layers were also deeply affected by the type and length of thermal treatments. Spurious phases like SnO_2, SnS and ZnS, were produced in some cases, and identified as a possible culprit for poor CZTS photovoltaic device efficiency.

Based on the extensive evidence collected during this research work, the present Thesis provides a rationale for an effective preparation of kesterite thin films for photovoltaic applications.

INDEX

Table of Contents

List of Figure

List of Tables

Chapter 1

INTRODUCTION

1.1 Colloidal synthesis

Between 1853 and 1857 M. Faraday observed the first colloidal sols particles in Au solution [1]. Then in 1861 Graham further developed the colloidal science, but at that time the study of colloids did not seem as important for the scientific community as in the following century. Only in the 20th century scientists started considering the importance of colloidal systems for preparing ceramic materials in mild conditions, as they allow a fine control of the size of particles starting from inorganic salts [1].

The electrostatic theory developed by B. Derjaguin et al. (1930-1950, DVLO theory), which combined the effect of Van der Waals and double layer forces, is the first scientific result in the science of stable colloidal suspensions [1]. Low-cost synthesis of organic-inorganic hybrids materials was not much a concern until the early '80s of the past century [1]; since then the colloidal synthesis (called also sol-gel process and schematically shown in Figure 1) from earth-abundant elements is the most widespread method to obtain a good control over microstructural parameters, such as particle size and shape, and a gram-scale production. Synthesis can be performed either at room temperature, leading to sols [2], or at high temperatures (e.g., by hot-injection [3]), leading to nanocrystals. In both cases nucleation and growth processes form a stable dispersion of colloidal or nanometric crystals in a solvent, which can later evaporate. Among the many options and case studies, the production of semiconducting nanocrystals for photovoltaic applications has become of great interest to reduce costs and select better performing materials. Therefore, the main

goal of the present work is to outline and improve the synthesis via sol-gel of quaternary compound Cu_2ZnSnS_4 (CZTS).
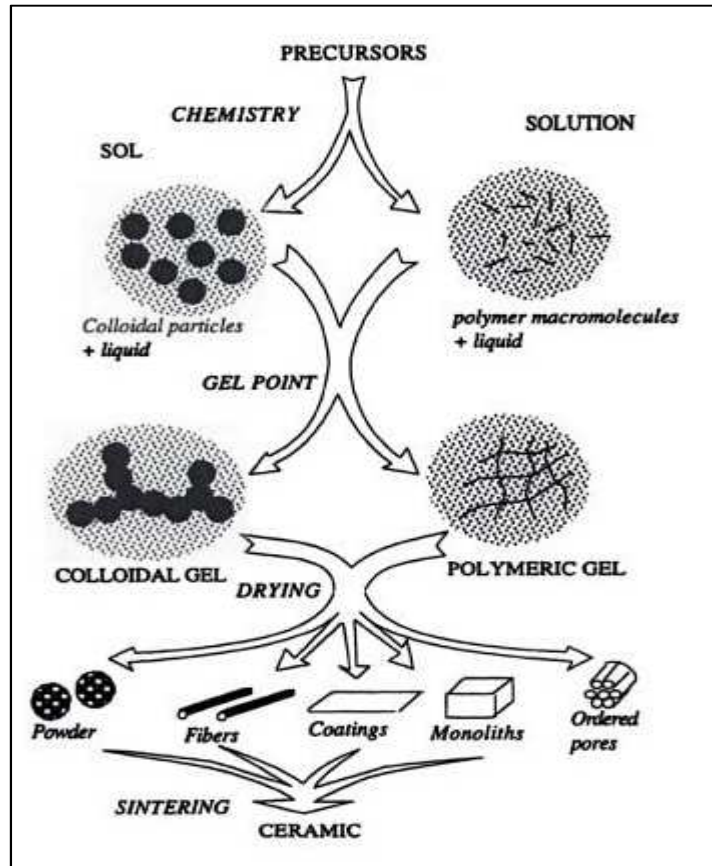
Figure 1. Simplified chart of sol-gel processes (reproduced from [1]).

1.2 Sol-gel and hot-injection methods

Nowadays, the demand of fine nanocrystals (NCs) is increasing, along with better synthesis methods, which are economically viable and suitable for an industrial scale-up. A rich literature describes the colloidal approach as a possible alternative to other synthetic methods, such as ceramic method [1], electrodeposition [4] and spray pyrolysis [5], highlighting the economic benefits of this choice. The study of electrokinetics, corrosion, optical and catalytic properties of this colloidal matter has a wide scientific interest [1], [3]. In the present work the production of solid particles of kesterite by nucleation and growth in a colloidal liquid medium (ink) is the main

goal, for obtaining definite shape and a narrow mono-modal size distribution [2, 3]. This synthesis route uses organic solvents (e.g., oleylamine, OLA), also acting as surfactants, and in some cases involves high temperature (hot-injection synthesis [3]). Chapters 2 and 4, respectively, describe theory and our results regarding the preparation of nanoparticles by the hot-injection method. The particles can be both precipitated from the liquid suspension, [1] or left dispersed in the liquid medium forming a colloidal suspension (without any heating) known as "sol" [1, 2].

Sol process is correlated with the sol-gel method, since after producing the sol a consecutive gel can be formed in one-step. The sol-gel could be described as: "Formation of an oxide network through polycondensation reactions of a molecular precursor in a liquid" [6]. The final particles can be amorphous or crystalline. Generally, the sol or colloidal suspensions of particles are ruled by the van der Waals forces or hydrogen bonds. The basis of sol-gel synthesis is "to dissolve a precursor compound in a liquid in order to bring it back as a solid in a controlled manner" [6, 7]. Sol-gel synthesis allows us to produce multi-component systems with a controlled stoichiometry by mixing sols of different compounds [2]; preventing problems of co-precipitation; and realizing an intimate mixing of reagents at atomic level, thus producing small particles.

As it can be noticed, hot-injection and sol-gel methods are useful, viable tools for reducing time and temperature during the synthesis of particles, controlling their crystallinity and size.

1.3   Semiconducting materials for photovoltaic applications

The electrical properties of a semiconductor material can be modified either by controlled addition of impurities or by the application of electrical fields or light, and thus one can use these properties to develop a broad range of functional devices, e.g., for signal amplification, switching, and energy conversion [8]. The one-way conductivity of semiconducting junctions provides the basic diode mechanism, which coupled with the sensitivity to light and heat and variable resistivity is the main property exploited to build photovoltaic cells. [8, 9].

A list of most common elements and compounds with useful semiconducting properties is shown below:

- Silicon and germanium are the most commercially relevant elements: they both have four valence electrons and form crystal lattices in which substituted atoms (dopants) can change the electrical properties.

- Many binary compounds, such as gallium arsenide (GaAs), AlAs, GaP, GaN, InP, InAs InSb, ZnS, ZnSe, ZnTe, CdS, CdSe, CdTe and SiC, to cite the most common ones.

- Certain ternary and quaternary compounds, including oxides, sulfides and alloys such as $FeTiO_3$, Cu_2ZnSnS_4 and Cu_2GeTe_3.

- Organic semiconductors made up of organometallic compounds like PPV: poly (p-phenylene vinylene), PFO: polyfluorene, P3AT: poly (3-alkylthiophene) and CuPc: Cu-phthalocyanine.

The most common semiconducting materials are crystalline solids, but amorphous and liquid semiconductors are also used [8, 9].

1.4 Quaternary semiconducting materials based on CZTS

Much of the current research efforts are directed toward the fabrications of thin film solar devices based on direct-gap absorbers belonging to a large family of quaternary metal sulfides with the general formula A_2BCX_4. Specifically, Cu_2ZnSnS_4 (CZTS) can be considered in close relationship with the previously developed binary and ternary compounds (see figure 2), [9]. A. Walsh et al (2012) [9] indicated that besides CZTS also $Cu_2ZnSnSe_4$ and its alloys $Cu_2ZnSn(Se,S)_4$ are promising candidates, related to the zinc-blende structure, but "the complexity associated with the multi-component system introduces difficulties in material growth, characterization, and application", which deserve to be examined in depth [9]. First of all, S. Schorr et al. [10] showed that the atoms in the Cu/Zn (001) layer of basic kesterite are disordered. According to A. Walsh et al. (2012), the random displacement of atoms in Cu/Zn sub-lattice can turn Cu_2ZnSnS_4 into the stannite

structure. A further point of interest regards the synthesis of homogeneous or multi-phase materials. In fact, within restricted stoichiometric constraints, single phase CZTS is obtained, otherwise ZnS, with Zn-rich precursors, and $CuSnS_3$, with Zn-poor ones, can be obtained. All these aspects affect the material's performance in the light-to-electricity conversion phenomena which are underlie all photovoltaic devices based on thin-films [9].
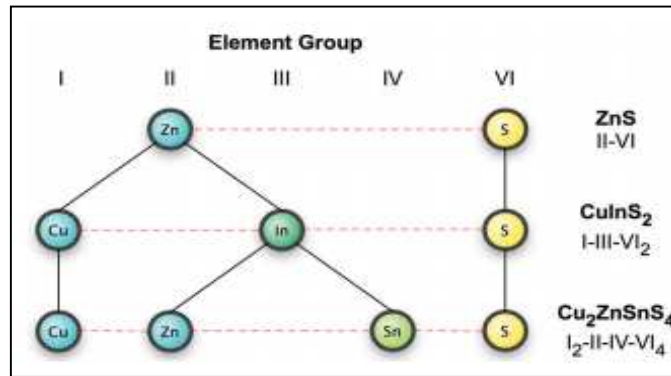
Figure 2. Relationship between binary, ternary, and quaternary semiconductors to produce Cu_2ZnSnS_4, starting from a II–VI parent compound [3].

CZTS, having a configuration I2–II–IV–V4 (see Figure 2), gives suitable and tunable bandgaps [9, 11]. The band gaps of configurations like I–III–VI2 and I2–II–IV–V4 are narrower than those of II–VI compound. Recent works on Cu (In, Ga) Se_2 (CIGS) material showed that the substitutions of Se for S, and Ga for In, allowed for an optimization of the final band gap. [9], [12, 13, 14, 15]. Analogously, A. Walsh et al (2012) [9] described that CZTS-based compounds, like $Cu_2ZnSnSe_4$, Cu_2FeSnS_4 and $Cu_2ZnGeSe_4$ have increased band gaps of 1.45 eV, [16, 17] 1.51 eV, [18] and 2.27 eV, [19], [9], respectively. Although alloying these CZTS compounds can improve band gap, their V_{oc} can still be low. Therefore H. Zhou et al. (2013) [20] reported that by "introducing more defects like antisites and vacancies species, some of which may act as recombination centers like different S/Se and/or Sn/Ge ratios" it is possible to change the bandgap meanwhile increasing the output voltage [20].

1.5 Chronology efficiency of CZTS by solar cells applications

The photovoltaic applications of CZTS have increased in recent years, in an attempt to gradually substitute the analogous CIGS (and CdTe). Since 1988 [21] several scientific reports considered CZTS as an alternative to CIGS for commercial solar cell systems. CZTS has a similar structure to the chalcopyrite of CIGS, but the raw materials of CZTS, based on earth-abundant elements, are five times cheaper than CIGS [21]. Moreover, unlike CIGS and CdTe devices, CZTS does not involve toxic elements.

CZTS was first synthesized in 1966 [22], but only in 1988 was it demonstrated to exhibit the photovoltaic effect [23]. Figure 3 shows a diagram promoted by the National Renewable Energy Laboratory (NREL) with the chronology of efficiency growth of several semiconducting cells. In particular it is shown: 1) efficiency of different cell types – single-crystal, thin film polycrystalline or amorphous; 2) the types and number of junctions used (single- or multi-junctions); and 3) some emerging PV devices. In the diagram the evolution of solar cell efficiency in CZTS devices can be followed: from 2.3% in 1997 to 5.7% in 2005. The last results were obtained just through the optimization of the deposition process [24].

In 2014, a bifacial device with CZTInS absorber material and transparent conducting back contact was reported to have 3.4% of efficiency [25]. In 2010, a solar energy conversion efficiency of about 10% (red route in Figure 3) was achieved by a CZTS device [25]. In August 2012 IBM announced a CZTS solar cell capable of converting 11.1% of solar energy to electricity [26]. In November 2013, the Japanese thin-film solar company Solar Frontier announced that in joint research with IBM and Tokyo Ohka Kogyo (TOK), they have developed a world-record CZTS solar cell with 12.6% energy conversion efficiency [27]. However, it should be noticed that all these excellent efficiency values were obtained by rather expensive synthesis procedures. In the present work the red route (Emerging PV: ◊ inorganic cells - CZTSSe) will be followed, using low-cost synthesis and techniques, analyzing how it is possible to increase the present band gap 1.5 eV [24] by some inorganic chemical modification during the synthesis.
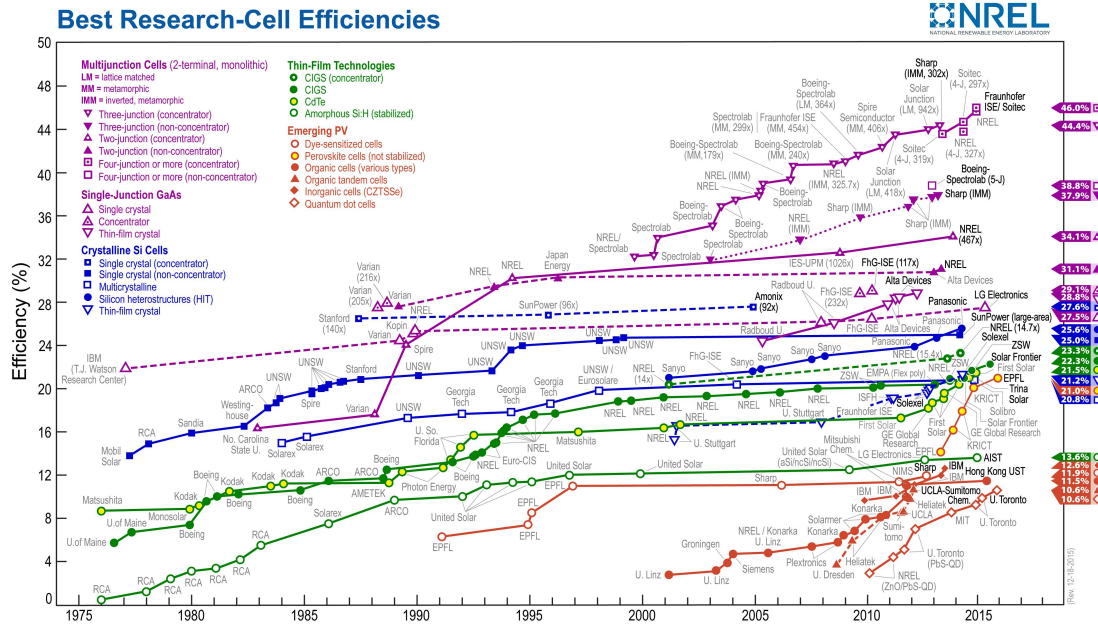
Figure 3. Chronology of record cell efficiency according to the National Renewable Energy laboratory (NREL, USA, http://www.nrel.gov/ncpv/images/efficiency_chart.jpg).

1.6 Objectives for this Research

The thesis work was organized according to the following ideas and guidelines:

- To produce high-quality CZTS thin films, e.g. with controlled composition and crystal structure in order to avoid phase separation, by low-cost methods, suitable for the industrial scale-up.

- To optimize the growth process of the CZTS layer exploring the effect of different post-deposition heat treatments, with or without sulfur.

- To coat and anneal CZTS thin layers on glass substrates for studying the growth of defects and optical properties also in correlation with possible formation of spurious secondary phases.

The most fundamental point in this investigation was to explore the routes to produce high-quality CZTS phase, showing the effect of spurious secondary phases on the microstructure and optical properties, to shed light on the correlation with the material composition.

1.7   Structure of the thesis

A brief overview of the basic properties of CZTS is presented in Chapter II. This thesis is then structured in three central experimental chapters:

- Chapter I is an Introduction to the topic.

- Chapter II is a brief overview of the basic properties of CZTS.

- Chapter III focuses on CZTS thin films produced by a water- and sulfurization-free solution route. Afterwards a description is presented of the growth process, together with a characterization of the optimized materials in terms of chemical composition. A detailed investigation of the stoichiometry effect on CZTS chemical properties, such as the differences induced by using a tin chloride precursor and and the final layer effects are also presented in this chapter.

- Chapter IV concerns the development of CZTS thin films by a hot-injection method, using spin-coating as a deposition technique. This chapter mainly focuses on the optimization of this material in view of its application as an absorber layer in solar cells.

- Chapter V is related to research activity on CZTS optical properties. Following the results of previous chapter IV, concerning synthesis processes and experimentation, this chapter focuses on: 1) effect of heat treatment time on the final layer, 2) structural characterization, and 3) optical properties of the absorbing layers.

- Chapter VI contains the Conclusions and some future perspectives.

Chapter 2

General overview of CZTS material

2.1   Stability of the solvents leads the synthesis of CZTS

CZTS nanoparticles can be produced by different methods using solvents as stabilizer or surfactant. According to the classic sol–gel method, primary particles can be grown in aqueous solution, if precursors metallic salts are soluble before the reactions of hydrolysis and condensation, which allow for the formation of inorganic polymers that eventually precipitate as amorphous particles [1] [28]. The processes of hydrolysis and condensation of precursors can occur also in different liquid media, for example alcohol or hydrocarbon solvents, depending on the chemical nature and reactivity of the precursors.

A pioneering work on the synthesis of CZTS NCs was published by Q. Guo et al. (2009 [29]), who injected a solution of elemental sulfur dissolved in OLA into a solution of the metal precursor (Cu, Sn and Zn) in OLA at 225 °C with a 30 min reaction time [29]. In fact, solution stability is a major issue. Cu, Sn and Zn ions from precursors salts dispersed among solvent molecules collide, as an effect of several mechanisms, like Brownian motion, convection and gravity [29], thus leading to condensation of new compounds. The forming particles of colloidal size should tend to attract each other by van der Waals [30] and Keesom forces [29], [31], [32] in absence of complexing stabilizing agents. If generally a complexing or chelating agent can be used to avoid precipitation of fast grown large particles, stability can be promoted by using solvents like oleylamine (OLA). The amine group forms ionic interactions with metallic ions and the long hydrocarbon chain can be effective in

avoiding agglomeration by steric hindrance [33]. Thus OLA is used to both activate the precursors and cover nuclei, from which nanocrystals (NCs) will be grown. As shown in the literature (e.g., see [34] and Figure 4), one of the effects of OLA is to create metal complexes and prevent agglomeration of the resulting nanoparticles [32], [34].

Current literature is poor on the issues arising from toxicity of solvents like OLA [32], which should be handled carefully, being corrosive and volatile at high temperatures [35].
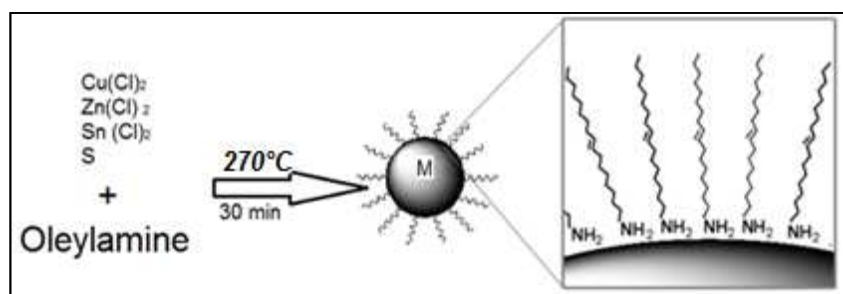
Figure 4. Oleylamine effects, creating metal complexes at high temperatures (over 230 °C) allowing the CZTS formation [32].

2.2   Development of ink Precursors

One of the most intriguing and promising ways of producing PV cells is to use inks for printing or spraying processes. In this regard the ink could be a hybrid sol containing nano-particles or amorphous inorganic 3D [32]. An appropriate ink should: 1) develop a large contact area between the two (liquid-solid) phases, 2) be produced by a large-scale process and 3) provide a continuous adherent "crack-free" layer of kesterite. [32].

S. Magdassi et al. (2010) [36] first underlined the possibility to inkjet and print this type of ink to prepare thin films. Ink requirements and formulation guidelines are extensively discussed in the literature. According to S. E. Habbas et al. [32], ink stability is a major point, achievable by properly designing its composition, stoichiometry and solvent. Regarding the latter, S. E. Habbas et al. (2010) [32] emphasized the importance of using low vapor-pressure solvents (like OLA), to

control evaporation during thin layer deposition [32]. In fact, a fast release of the solvent during the deposition process can cause a non-uniform surface, and a premature precipitation of reactants [32].
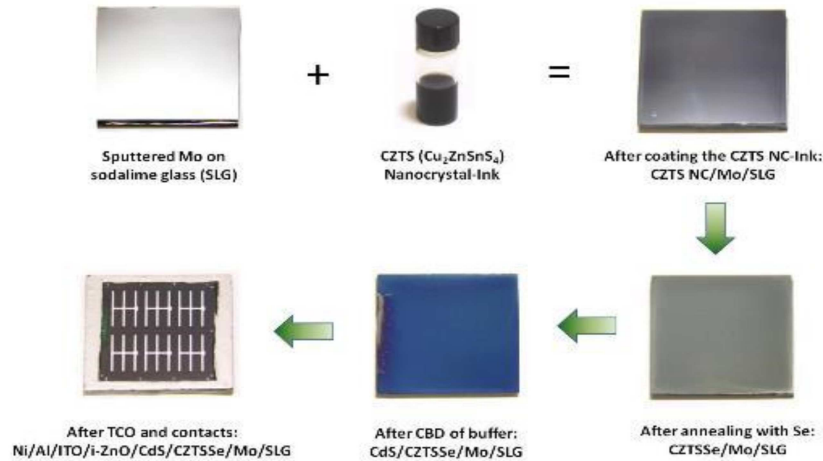
Figure 5. Fabrication of a nanocrystal-ink based copper zinc tin sulfoselenide solar cell starting from an ink of CZTS nanocrystals and ending with a 7% efficient photovoltaic device [37].

Figure 5 shows how to prepare a PV device using an ink [38, [39]. A further point of interest is the substrate. Organic polymeric substrates are largely used for their low cost and flexible features, although they are not as thermally resistant as metal foils or glasses [32].

2.3   Low cost deposition techniques

The most popular low cost techniques for preparing colloidal films are dip-coating and spin-coating, but other techniques may be applied, such as capillary-flow, spraying and electrophoresis [2], [3], [40].

2.3.1   Dip-coating

This well-known technique consists in dipping a substrate into a sol and withdrawing it at constant rate so that, as M. Guglielmi (2001) [40] reported, "a liquid layer remains on the substrate with a thickness profile that is determined by the effect of different

forces (described in the section 2.1) on its flow". M. Guglielmi et al. (1992) [41] also observed that, in the case of sols prepared by metal-organic precursors like metal alkoxides, during the process the sol "changes its rheological properties mainly due to evaporation of solvents, but also as a result of diffusion of water from the processing atmosphere", which promotes hydrolysis of precursors. Further to hydrolysis and condensation reactions occurring in the fresh sol layer, the viscosity increases quickly and the gel point is attained, so that the thickness of the deposited layer is fixed and does not change anymore [32]. Therefore, M. Guglielmi et al. (1992) stated that the withdrawal at constant speed could produce a film layer with constant thickness [41].

The thickness (h) of film prepared by dip-coating by using a sol-gel process can be determined by the following equation:

$$h = 0.94 \frac{H_\eta \upsilon^{2/3}}{\gamma^{1/6} \, (pg)^{1/2}}$$

where the withdrawal speed is υ, viscosity H_η, surface tension γ, and density p of the solution and gravity acceleration constant g. From this equation it can be deduced that the thickness of the layer can be controlled by varying the withdrawal rate. According to M. Guglielmi and S. Zenezini (1990) [42], "large planar substrates or axially symmetric substrates may be uniformly coated by the dip-coating technique with a batch or a continuous process (Figure 6 (a)). The coating could be also applied to a complex substrate. However, the thickness will not be uniform over the entire surface. Nevertheless, thickness uniformity will be achieved only if the driving mechanism for the withdrawal of the substrate acts smoothly and if any sources of mechanical or acoustic vibrations are eliminated" [42].

2.3.2   *Spin-coating*

In spin-coating (Figure 6(b)) a proper amount of sol is put onto the substrate, which, initially stationary, is then rotated at constant angular velocity ω. The excess of sol flows radially outward, driven by centrifugal force (calling spin-up stage) and

eliminated from the substrate (spin-off stage) [40]. At the latter stage, as mentioned by M. Guglielmi (2001) [40], "evaporation of the solvent, which occurs uniformly over the sample, increases the concentration of the solution" [31]. Due to the greater density and viscosity resulting at the end of the process, at this point gelation of sol or the deposition of a determined ink takes place, and the thickness of the material layer is fixed [40], [43]. The thickness is related to ω by the relation:

$$h = A\omega^{-B}$$

where A and B are constants. B ranges between 0.4 and 0.7. Spin-coating is a convenient technique for preparing films having uniform thickness, provided that a homogeneous sol with a constant viscosity is available. The main typical drawback of spin-coating is that only small samples with a planar and simple geometry can be coated uniformly [40].
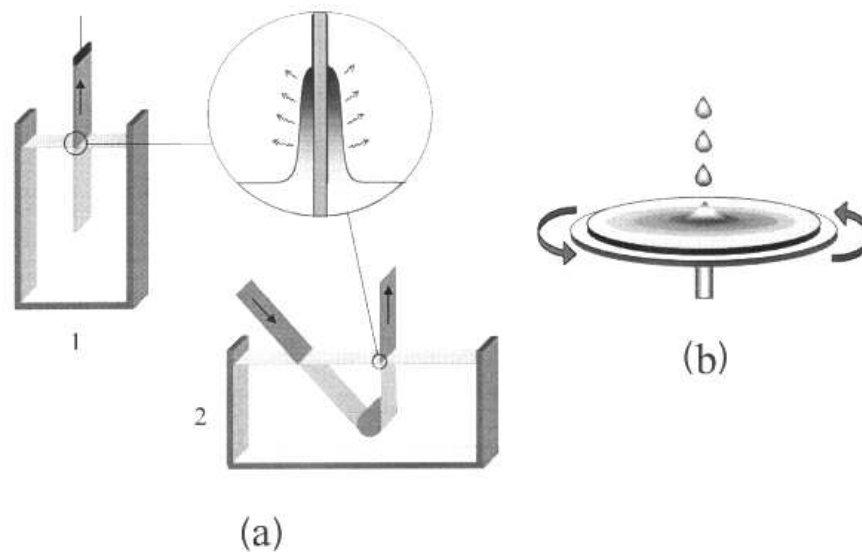
Figure 6. Processes used to make thin-film coatings: (a) dipcoating (1: batch process, 2: continuous process); and (b) spin-coating processes [38].

Once the deposition of the colloidal films is carried out, it is necessary to proceed with thermal treatment, in order to obtain the final desired material. The effects of this thermal treatment or annealing on the CZTS thin films are described below.

2.4   Annealing effects from the precursor CZTS thin film.

The sulfurization process, or the use of a sulfur source together with an inert atmosphere during annealing, can contribute to modify the elemental distribution through the entire CZTS layer, especially those of Sn, Ge, S and Na [44]. The surface morphology consists of several stacked layers, up to six in some cases. After each treatment [81], the surface morphology of each layer can be different, despite having similar composition ratios [45].

An appropriate annealing temperature could optimize quality, crystallization and crystal structure of the thin films. According to the literature, the substrate surface warps at high temperatures so that strains and defects increase, affecting the growth of the crystalline phase [46]. As a consequence, a proper heat treatment at the correct annealing temperature is one of the keys to improve the quality of the thin films.

Regarding the temperature of the annealing, literature reports that kesterite annealed at 450 °C shows the (112) diffraction peak and a good crystalline quality; moreover, higher annealing temperatures give larger grain size, and consequently lower extension of grain boundaries [46]. Quite importantly, grain boundaries, as many other defects, can act as carrier traps, decreasing mobility and conduction [47].

Figure 7 shows a system for annealing the precursor, with a sulfur source and inert atmosphere [53], [81]. A recent publication by A. Emrani et al. (2013) [48] shows the surface morphology of CZTS thin films annealed at temperatures between 500 and 575 °C. Increasing the annealing temperature improves the crystallinity of the CZTS thin films. Larger crystalline grains as well as compact and void-free structure reduces the number of secondary phases. The authors observed that at 500 °C the grains are smaller and some voids are also present [48]. Grains start to coalesce as the annealing temperature increases, with compact and larger grains observed at annealing temperature of 525 °C and 550 °C. At 550 °C, the grain size is approximately 1 µm [48]. However, beyond 550 °C grain coarsening starts, which seems to lower the film performance. Accordingly, 550 °C is the best temperature for the annealing in order to optimize the performance of the CZTS thin films. Moreover, Energy Dispersive Analysis X-ray (EDAX) measurements reveal a zinc rich and copper poor composition, with a Zn/Sn ratio ≈ 1.2 and Cu/(Zn + Sn) ratio ≈ 0.89. So far higher

efficiencies and optical properties have been obtained with zinc-rich and copper-poor compositions [49].
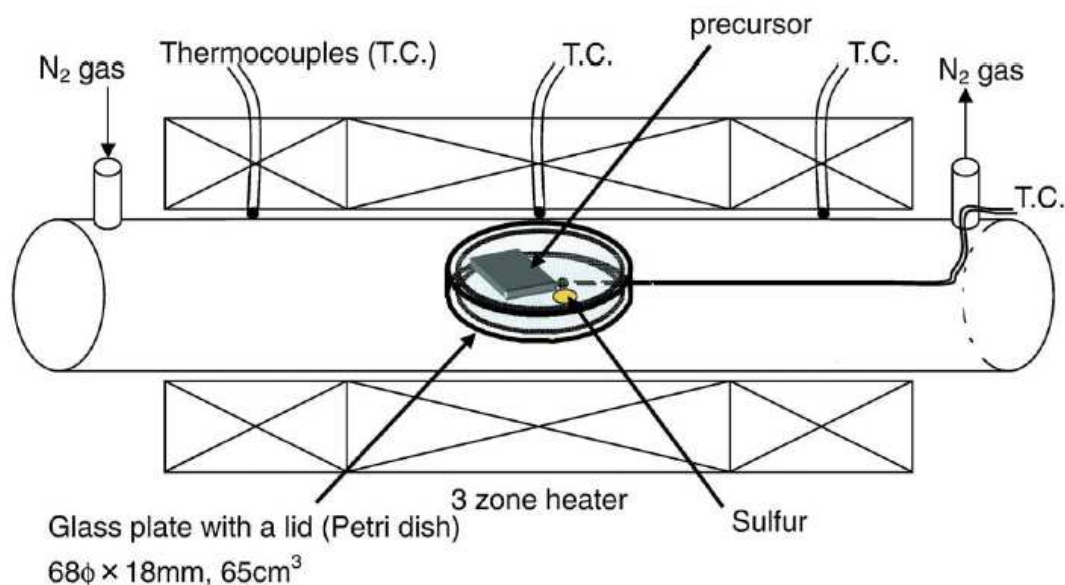
Figure 7. Schematic diagram of the sulfurization furnace [53].

2.4.1   *CZTS phase formation during the annealing process*

According to S. Delbos (2012) [50], CZTS is formed in a range of temperatures between 500 and 600 °C and, similarly to CIGS material, through chemical reactions not yet completely understood [50].

Two types of processes have been studied by S. Delbos (2012) [50], in order to assess the reactions forming CZTS: a one-step process (CZTS precursors already annealed with an elemental Cu-rich target) and a two-step process (CZTS non-annealed precursors, sulfur poor). In both processes the temperature and the presence of sulfur play a fundamental role. These authors clearly state the importance of a strict control on the annealing temperature, because a too-fast treatment can develop strain and Sn formation. These two effects hinder the formation of large grains, especially in the two-step process [50, 51], S. Delbos (2012) [50] also remark that reactions are "taking place in the bulk of the layer between the elements leading to binaries, ternaries and

finally the quaternary" phase [50]. "At room temperature only binary compounds" [50], such as Cu_6Sn_5 [52], Cu_5Zn_8 [53], Cu_3Sn and $CuZn$ are formed [54], [50], at higher temperature (200 to 450 °C), metal chalcogenide binaries such as CuX, Cu_2X, and SnX (X corresponds to the non-metal element) are formed [50], [55, 56, 57]. Beyond 450 °C, Cu_2X binaries react with Sn to form Cu_2SnS [50]. Only over 550-580 °C [58, 59], and prolonged annealing time (or one-step deposition and treatment at 500 °C [60], ZnX reacts with the ternaries Cu_2SnX_3 to finally form Cu_2SnZnX_4 according to the following equation [50]:

$$Cu_2SnX_3 + ZnX \rightarrow Cu_2ZnSnX_4. \quad (1)$$
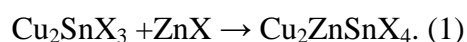
A further important feature of the annealing process, is the use of elemental sulfur (or selenium) or H_2S. The latter is less reactive than elemental sulfur and consequently requires a longer annealing time for forming binary compounds and large CZTS grains [50], [61, 62]. However, using H_2S requires quite demanding control standards for the environmental toxicity and hazards, so that the use of sulfur under inert atmosphere is usually preferred.

The one-step process favors the conditions for the growth of Cu-rich material [63], [50], whereas using an excess of sulfur does not promote the growth of large grains [50].
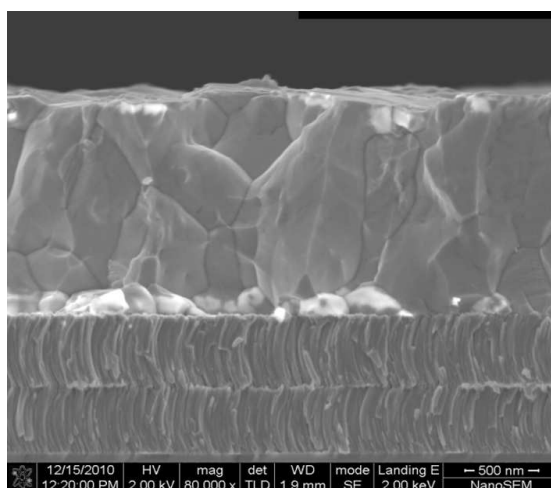
Figure 8. SEM cross-section of CZTSe with ZnSe segregation at the back contact (reproduced from [50]), [67].

16

Finally, both processes produce Zn-rich layers, and in particular Cu_2X-free binaries [64]. It is worth noting that if the film contains Cu_2X at the end of the synthesis process, a subsequent etching, e.g. using cyanide, leads the formation of voids and defects [50]. If Zn-rich growth conditions conditions are used, ZnX formation is promoted (Figure 8 shown the ZnX formation at the back contact) [50], [65, 66, 67].

2.4.2   The atmosphere control in the annealing process

Unlike CIGS, the reagents for a CZTS synthesis are prone to evaporation and sublimation [41]. According to S. Delbos et al. (2012) [50], the Zn compounds sublimate at 430 °C [68], SnSe at 350 °C [55], SnS at 370 °C and Sn at 460 °C [50], [69, 70]. It is necessary to be aware that both high temperatures and atmosphere control can promote CZTS decomposition pushing to the right the equilibrium of equation (2) [71, 72], [59].

$$Cu_2ZnSnX_4 \text{ (s)} \longleftrightarrow Cu_2X(s) + ZnX(s) + SnX(s) + 1/2X(g) \uparrow \text{ (2)}$$

If this equilibrium is shifted to the right, ZnX, SnX and X are formed, leading to Cu_2X-rich layers, which increase resistance and prevent good photovoltaic efficiencies [50]. Thus, in order to avoid CZTS decomposition, the atmosphere should be saturated with the products of the right-side of equation (2) [50]. During the thermal treatment, SnX can be introduced [50], or the partial pressure of chalcogen can be increased [73, 74], by using in both cases a lid to cover a small closed volume above the precursor layer [75], [82]. Alternatively, using a H_2S source during annealing, Zn loss can be prevented by using ZnS as a precursor [76]. In some cases it seems that the presence of MoX_2 from the molybdenum substrate pushes the reaction (2) to the right [77], [50].

Although it is known that fast annealing in inappropriate atmosphere leads to the decomposition of CZTS, an appropriate atmosphere and slow annealing also causes the formation of different secondary phases, including binary and ternary compounds [78].

As described in the previous section, S. Delbos (2012) et al. [50] elaborated two strategies of CZTS synthesis annealing: one-step (precursors with Cu-rich condition

with no sulfur excess) and two-steps (from precursors needing a sulfur excess). In the latter, the annealing step consists of a short step (a few minutes) for forming CZTS and a longer one (up to a few hours) for increasing grain size. Thus the atmosphere could also be different in each step [50], provided carrier gas and its pressure are well controlled. Actually the atmosphere control is not a simple task in sputtering systems, "because reaction chambers are designed for controlling the deposition rate and not the partial pressure of each element" [50], [82]. This simple consideration clearly adds more interest to chemical routes.

2.5 Use of the ternary phase diagram (TPD) to understand the CZTS phase stability and secondary phases

The complete phase diagram of CZTS, containing four atomic species, requires a complex three-dimensional representation. The amount of sulfur in the film depends on the reactions occurring with the metallic precursors, reducing the degrees of freedom of the system to three. The study of J. J. Scragg et al. (2010) [63] on phase diagram was based on comprehensive measurements done by D. Olekseyuk et al. (2004) [79]; ternary phase diagrams for a system at 400 °C with different regions of composition are shown in Figure 9 and 10. It is worth noting that the phase diagram of Figure 9 is valid in a quasi-equilibrium at 400 °C. However, other experiments carried out in comparable conditions (e.g. [80]) demonstrated the occurrence of secondary phases, predicted by the diagram. Therefore, it may be useful both to depict the compositions of the samples and to support assumptions concerning composition and secondary phases. The diagram shows ten fields, each of them implying the presence of CZTS with one or two secondary phases [63]. Around the middle (the point is labeled as "1" in Figure 9) only CZTS should exist. It is important to highlight that all the secondary phases are compounds of sulfur and there are no metallic phases [63] [79]. As described in the previous section, an excess amount of sulfur is provided during the sulfurization process. However, not all the secondary phases have been considered, because they depend on the thermal treatment conditions [79]. An

important secondary phase is SnS_2, which forms at 700 °C when an excess of Sn precursor is present, leading to a decrease in final efficiency of the CZTS layer [53]
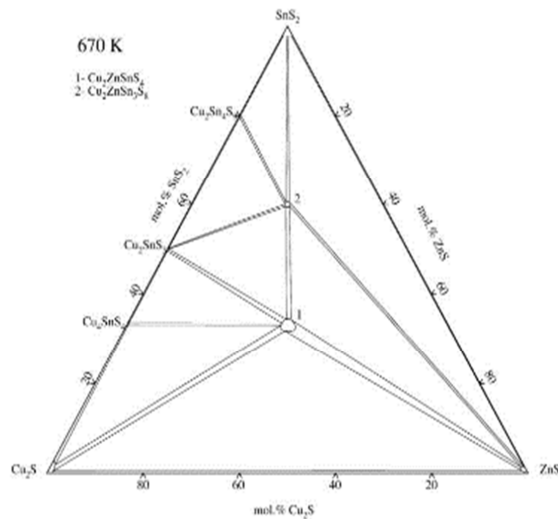
Figure 9. Ternary phase diagram of the Cu_2S–ZnS–SnS_2 quasi-ternary system at 400 °C [63] [79]. Secondary phases expected in the different regions of the phase diagram are also reported (see the Table 2).

The investigations of J. J Scragg et al (2010) [63], divide the phase diagram in regions already indicating the possible secondary phases (Figure 10) [63]. In the Zn-rich region, for example, ZnS is the expected secondary phase formed by an excess of Zn precursor. The Zn-poor region covers several fields with various possible secondary phases. One can notice that this notation is clear but unusual: in literature Cu-poor and Cu-rich are usually distinguished (e.g. [53]), without consideration for the ratio between the remaining metals.

At the end, it is important to consider that in an ideal phase diagram only secondary compounds with Cu(I), Zn(II) and Sn(IV) are taken into account, with no mention of ternary compounds such as Cu_2SnS_4, Cu_3SnS_4 or Cu_4SnS_6. According to Malerba (2014) [82], the main spurious phases are those of Table 1: some of these are just intermediate products of the reaction (at T <500 ° C), while others are also present in the final film [81, 82].
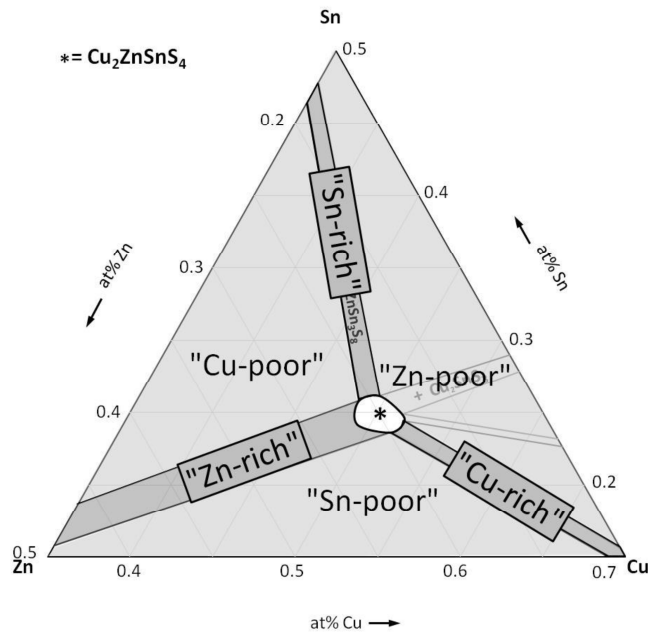
Figure 10. Ternary phase diagram with different regions of composition [63].

Table 1. Secondary phases for the Cu-Zn-Sn-S system for each material, stability region, crystal structure (hexagonal), bandgap energy Eg and XRD reference (ICDD) card number are reported [81, 82].

Chemical Formula	Mineral	Stability	Structure	Eg (eV)	XRD card
CuS	Covellite	$T < 507°C$	hexagonal	1.7	06-0464
					75-2233
Cu$_2$S	Low-Chalcocite	$0°C < T < 104°C$	orthorhombic	1.18 [83]	23-0961
					73-1138
Cu$_2$S	High-Chalcocite	$90°C < T < 435°C$	hexagonal		84-0206
Cu$_9$S$_5$	Digenite	$72°C < T < 1130°C$	rhombohedra	1.8 [84]	47-1748
					84-1770

Chemical Formula	Mineral	Stability	Structure	Eg (eV)	XRD card
$Cu_{31}S_{16}$	Djurleite	*T < 93°C*	orthorhombic	1.4	42-0564 83-1463
Cu_7S_4	Anilite	*T < 75°C*	orthorhombic		72-0617
$2H-ZnS$	Wurtzite		hexagonal	3.91	79-2204
ZnS	Sphalerite		cubic	3.54	05-0566 71-5975
$\alpha-SnS$	Herzenbergite	$T_{melt} < 605°C$	orthorhombic	1.3 [85]	83-1758 (Amnm)
$\beta-SnS$		$T_{melt} > 605°C$			73-1859 (Pbnm)
Sn_2S_3	Ottemanite			1 [85]	75-2183
$2H-SnS_2$	Berndtite	$T_{melt} = 870°C$	hexagonal	2.2 [85]	23-0677 83-1705
$4H-SnS_2$					21-1231
Cu_2SnS_3		T>400°C	Cubic	0.96 [86]	
Cu_2SnS_3		T<400°C	tetragonal	1.35 [86]	
Cu_3SnS_4	Isostanite		orthorhombic	1.60 [86]	36-0218
Cu_4SnS_6	Synthetic	$T_{melt} <537°C$	rhombohedra		36-0053
Cu_2ZnSnS_4	Kesterite		tetragonal	1.5	26-0575

Chapter 3

CZTS synthesis by non-vacuum process

This chapter describes the production of CZTS thin films deposited from a metal salt solution using two aqueous solutions. After mixing these solutions and obtaining the sol, a dip-coating method is used to deposit wet precursor films. After presenting the influence of different solutions and precursors, a study of phase formation using in situ and ex situ methods will be discussed. Moreover, the effects of tin chlorides and sulfur conditions with respect to the phase purity will be discussed and possible solutions to avoid them will be addressed. Finally a tentative test of a solar cell cross section is presented, together with an evaluation of optical properties.

Renato D'Angelo[a], Cristy Leonor Azanza Ricardoa, Alberto Mittiga[b], Paolo Scardi[a], Matteo Leoni[a].

[a] *University of Trento, DICAM, Via Mesiano 77, 38121, Trento, Italy.*

[b] *ENEA C.R. Casaccia, (S.P. 064), Via Anguillarese 301, 00123, Roma, Italy*

3.1   Introduction

Thin film solar cells aim to become competitive with traditional silicon-based devices, as a low cost per kW of the base materials is coupled to the possibility of building the cell on flexible and non-flat substrates. Energy harvesting in a thin film solar cell is obtained via electron-hole pair formation in a suitable absorber layer. The best absorbers so far contain cadmium (e.g. CdTe, max laboratory efficiency of 18.3% [87]) or indium (CIGS, $CuIn_xGa_{1-x}Se_2$, max efficiency 20% [88]), the first one being notoriously toxic and the other quite expensive.

The research is thus fostered towards finding alternative absorbers, based on non-toxic and inexpensive elements. The most interesting results are currently shown by a synthetic analog of the mineral kesterite with formula $Cu_2ZnSn(S,Se)_4$ (CZTS). An efficiency of 11% has been already achieved in the laboratory using a partially selenized CZTS [19]. Many processes have been proposed for the production of CZTS thin films and powders (for solar inks), most of them based on vacuum deposition, complex synthetic routes or requiring a sulfurization step, all of which are too expensive for mass production. Limiting the scope to cheap production routes, the best stoichiometry, morphology and band gap (1.44-1.51 eV) have been obtained with absorbers synthesized from liquid phase [89]. Conventional aqueous solution processes entail the possibility of forming M–O–M bonds in the precursor solution or during the annealing step, which can lead to the formation of unwanted extra phases if the incorrect solvent is employed. Recent studies [90-91] have shown the effects of water, ethanol, ethylene glycol and methanol as solvents: near stoichiometric CZTS films were obtained up to 500-550 °C. H. Park et al. [92] tested nitrogen to replace H_2S for heating treatment and confirm the optimal stoichiometry of sulfur in the material.Here we report a simple process to obtain CZTS without vacuum and without sulfurization. A Zn-rich/Cu-poor CZTS is obtained, beneficial e.g. for solar energy applications: previous reports [93,94] suggested that a Cu-poor material leads to the formation of Cu vacancies, which are shallow acceptors in CZTS, while a Zn-rich condition suppresses Cu substitution on the Zn sites, and thus decreases the quantity of deep acceptors. (cf. R. D'Angelo et al. 2014: 1 [2]).

3.2 Sol-gel experimental details

Two routes using water and sulfurization-free solution, similar to the one proposed in [90-92] are employed to obtain a stable stoichiometry of $Cu_{2-x}Zn_{1+x}SnS_4$ (where x=0.2). Copper chloride (Cu (II) $Cl_2 \cdot 2H_2O$), zinc chloride (Zn (II) Cl_2) and tin (IV) chloride were chosen as metal sources. Both the anhydrous and the pentahydrate tin (IV) chloride (Sn (IV) Cl_4 and Sn (IV) $Cl_4 \cdot 5H_2O$, respectively, were tested. Thiourea ($SC(NH_2)_2$, was chosen as sulfur source. (cf. R. D'Angelo et al. 2014: 2 [2]).

In this work, precursor composition was varied within the Cu-poor and Zn-rich stoichiometry region, which is known to give CZTS samples with the best performances as absorber layer described in the previous motivation and state of the art. Solutions were prepared by dissolving 0.45 mol of the copper source, 0.30 mol of the zinc source and 0.25 mol of the chosen tin source in 20 mL of solvent using a magnetic stirrer. Subsequently, 20 mL of a 0.60 M solution of thiourea was added. A brown sol is obtained that turns white after short stirring and then reverts to a transparent and limpid yellow liquid after around 5 minutes of continuous stirring, as shown in Figure 11. (cf. R. D'Angelo et al. 2014: 2 [2]).

Figure 11. Final solution after 5 minute of stirring (S2B)

The resulting solution can be employed for the production of both powders and films. Several combinations of solvents (water, ethanol, ethylene glycol and methanol) were tested. A detailed list of synthesis conditions is reported in Table 2.

Table 2. Details of the solutions and their corresponding ID's.

Sol	Solvent (Salts)	ratio	Solvent (thiourea)	Tin source	Thermal treatment	Other phases
S1A	Ethanol	1:1	H_2O	$Sn(IV)Cl_2$	T0-air + T1+S-1h	SnO_2++ Cu_2S+
S2A	Methanol	1:1	EG	$Sn(IV)Cl_2$	T0-air + T1+S-1h	SnO_2+
S3A	Ethanol	1:1	EG	$Sn(IV)Cl_2$	T0-air + T1+S-1h	SnO_2+ Cu_2S++
S4A	Ethanol	1:2	EG	$Sn(IV)Cl_2$	T0-air + T1+S-1h	SnO_2++ Cu_2S++
S1B	Ethanol	1:1	H_2O	$Sn(IV)Cl_2\cdot 5H_2O$	T0-Ar + T1-noS-3h	SnO_2++
S2B	Methanol	1:1	EG	$Sn(IV)Cl_2\cdot 5H_2O$	T0-Ar + T1-noS-3h	--------
S3B	Ethanol	1:1	EG	$Sn(IV)Cl_2\cdot 5H_2O$	T0-Ar + T1-noS-3h	Cu_2S+
S4B	Ethanol	1:2	EG	$Sn(IV)Cl_2\cdot 5H_2O$	T0-Ar + T1-noS-3h	SnO_2++

Following the literature and theory described in Chapter 2, the salts decompose, leading to the formation of CZTS by the steps described below:

Metal chlorides and thiourea dissolutions

$$Cu(Cl)_2 \longrightarrow Cu^{2+} + 2Cl^-$$

$$Zn(Cl)_2 \longrightarrow Zn^{2+} + 2Cl^-$$

$$Sn(Cl)_4 \longrightarrow Sn^{4+} + 4Cl^-$$

$$(CH_4N_2S) \longrightarrow S^{2-} + H^+ + NH_2\text{-}C\text{=}NH$$
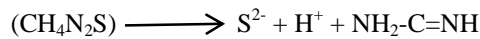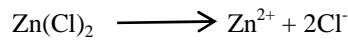
First solution: Reaction of metal chlorides in presence of solvent.

$$[M(Cl)x]XH2O \xrightarrow{CH3OH\ \Delta} M^+ + Cl^- + XH2O \xrightarrow{CH3OH} M - OCH3 + XHCl$$

S2B: $Cu(Cl)_2 + Zn(Cl)_2 + Sn(Cl)_4 + 7H2O \xrightarrow{\Delta+\ \mathbf{CH3OH}} Cu^{2+} + Zn^{2+} + Sn^{4+} + {}^-OCH3 + XHCl + XH_2O\uparrow$
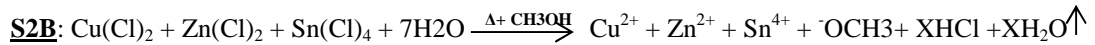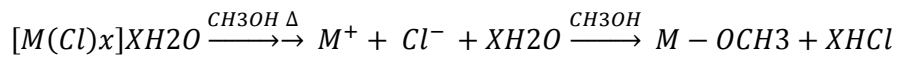
Second solution: Thiourea dissociation in presence of solvent

$$\underset{H2N - \underset{|}{\overset{|}{C}} - NH2}{\overset{S}{}} \xrightleftharpoons{C2H6O2} \underset{NH2 - C = N - H}{\overset{\ddot{S}-H}{}} \Longleftrightarrow N \equiv C - NH2 + H2S \longleftrightarrow S^= + 2H^+$$

S2B: $(CH_4N_2S) \xrightarrow{\mathbf{HO\text{-}CH_2\text{-}CH_2\text{-}OH}} S^{2-} + H^+ + NH_2\text{-}C\text{=}NH + OH\text{-}CH_2\text{-}CH_2\text{-}OH$
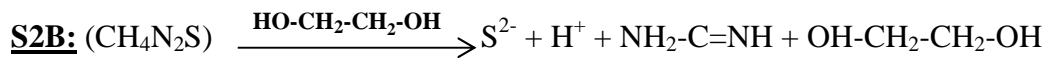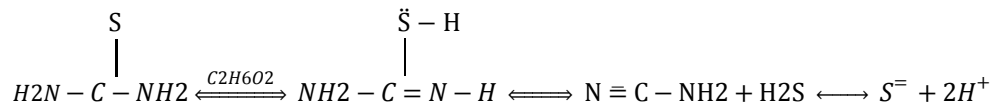
Final solution to CZTS formation: The nucleophile and coordination attack

$$XM1 - OCH3 + XM2 - OCH3 + XM3 - OCH3 + 4S^= + 2H^+ \xrightarrow{\quad 40° \quad}$$

$$S - M1 - \ddot{O} - CH3 \ + \ S - M2 - \ddot{O} - CH3 + S - M3 - \ddot{O} - CH3 \xRightarrow[560℃]{\Delta} \mathbf{Cu_{1\text{-}2}Zn_{1+2}SnS_4}$$
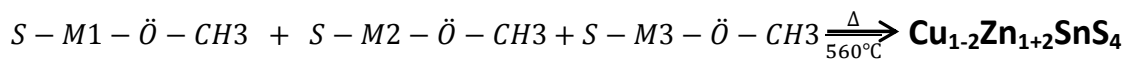
3.2.1 Deposition of precursors sols by dip-coating

Films were obtained by dip-coating (reported in section 2.3.1): an example is shown in Figure 12. Residual solvents were removed by heat, treating the film at 150 °C for 5 min. In the dip-coating process, substrates were dipped and retracted at 3000 mm/s with no yield time in the beaker. Soda lime glass slides (Corning 2947) were used as substrates.
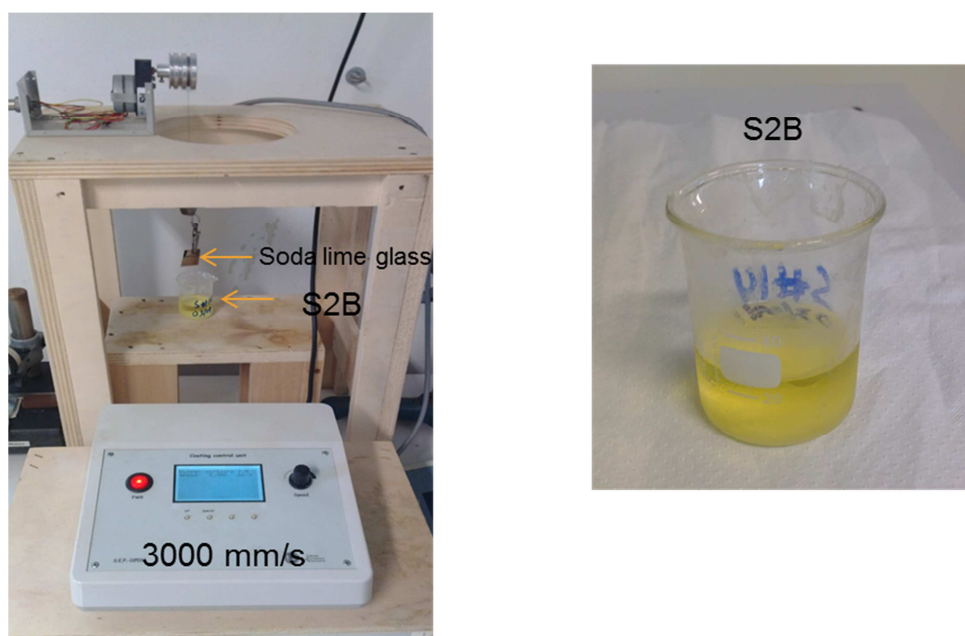
Figure 12. Example of the dip-coating deposition on a soda lime substrate using 3000 mm/s

The deposited and annealed samples were characterized by X-ray diffraction (XRD), Raman spectroscopy, SEM and EDX. The annealing process is described in the next section.

3.2.2 Annealing of the precursors CZTS thin film deposited

A two-step thermal annealing was employed. The first step, performed at 220 °C for 10 min in air (T0-air) or in Ar (T0-Ar), respectively for the set A and set B of specimens. The first step is aimed to remove the process solvents. The second step at 550 °C in Ar (T1-Ar) promotes the crystallization of the film and, if it is necessary,

completes the sulfurization. Two alternatives were employed for the second step: either with 400 mg sulfur for 1h (T1-S-1h) or without sulfur for 3h (T1-noS-3h). An example of the annealing system is shown in Figure 7 of chapter 2, section 2.4 and a picture of the real system is shown in Figure 13. For specific details of each annealing schedule, see Table 1.

The sintering of solution-deposited precursors within thin films with different types of atmosphere can influence the grain growth, metal ion distribution, formation of secondary phases and therefore the electronic properties of the resulting CZTS solar cells. Of special interest in the following sections is the evolution of different layer morphologies, as well as the bulk and surface composition when the precursor is annealed under inert atmosphere and contemporaneously in sulfur atmosphere.

Figure 13 Tubular furnace. Inside there is a sample to be annealed with 400 mg of sulfur for 1 h

3.3   Results and discussion of the sols (S2B) precursors

3.3.1   *Formation of Cu$_{1.8}$Zn$_{1.2}$SnS$_4$*

In order to understand the sequence of reactions leading to the formation of Cu$_{1.8}$Zn$_{1.2}$SnS$_4$ infrared absorption spectra (FT-IR) were from the precursor solutions. The instrument used was a PerkinElmer SPECTRUM ONE FT-IR spectrometer (633

nm Class 1 laser), on liquid droplets using an ATR (Attenuated Total Reflection) attachment (ZnSe crystal).

The study of the reactions of $Cu_{2-x}Zn_{1+x}SnS_4$ was done on the S2B solution as well as on the metal and the thiourea solutions leading to it (named, respectively, S2B-metal and S2B-thiourea). The methanol solution of the chlorides can be quite a complex system: at the given low molarity, the salt is totally decomposed and just coordination complexes are expected in S2B-metal. Some water should also be present due to the atmospheric moisture, the residual water in the alcohol, and the structural water released by the solids. Under those conditions, some alkoxides $(M(OR)_n)$ may form, but their condensation (thus the formation of a proper gel) is unlikely, at least for short processing times: the metal ions will be therefore coordinated by the alcohol and by the water molecules (M-O-R or M-O-H$_2$). The typical demonstration of this formation occurs when a green color is observed like that seen in Figure 14. (cf. R. D'Angelo et al. 2014: 3 [2]).

Figure 14. Metal solution, (S2B-metal)

The green color is typical for coordination compounds e.g. of Cu. The FT-IR spectrum of S2B-metal confirms this coordination, being very similar to the methanol one, but with the extra presence of a 1635 cm^{-1} peak compatible with the υ2 band of liquid water (see figure 15)
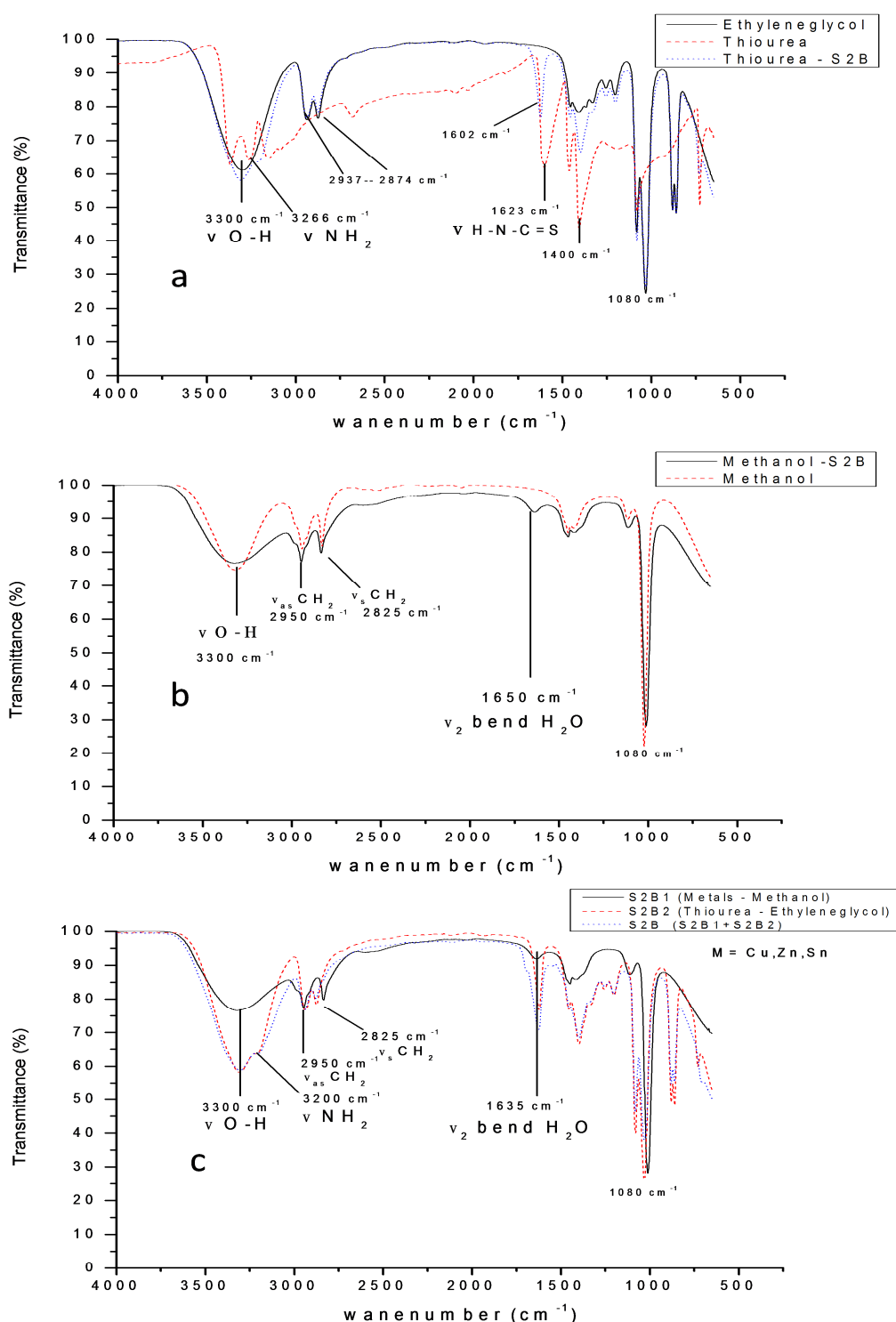
Figure 15. ATR-FTIR spectra. In (a) the precursors solution: Thiourea, Ethylene glycol, and thiurea on ethylene glycol (S2B-Thiurea). In (b) the methanol and the precursor solution: alkoxydes in methanol (S2B-Metals). (c) The final solution (S2B) CZTS samples with the methanol solvents: ethylene glycol and the precursors solutions: S2B-Thiurea and S2B-Metals

In the spectrum (Figure 15 a) for the thiourea solution it was possible to observe that the organosulfur compound (thiourea) is dissolved completely in the diol in an analogous way. The alcoholic dissolution of thiourea has already been reported in the literature [95]. The FT-IR spectrum of S2B-thiourea shows all the features of ethylene glycol solution plus some extra bands related to nitrogen of thiourea. The double band observed around 3300 cm^{-1} is in fact the combination of the OH signal from water and the diol with the doublet coming from the stretching of the NH$_2$ of thiourea [96].

Through this characterization it was possible to understand the role of the two mixed solutions, and as the lone pairs of sulfur in thiourea are attracted to the metal cations and it will likely substitute for at least some of the existing species coordinating the metal (more likely the alcohol and water molecules, as they are less bound to the metal ion).

Following literature [95, 96], the cations will be therefore octahedrally coordinated by the original anions (chlorine) plus a variable number of thiourea, methanol and water molecules. The number largely depends on the cation valence and on the steric hindrance. This coordination of the metal ion(s) with sulfur is likely to be responsible for the change of color of the S2B solution just after S2B-metals and S2B-thiourea are mixed. The coordination with the metal ion lowers the strength of the S-C bond in thiourea that becomes more prone to a nucleophilic attack and possible conversion into a O-C bond. A plausible type of attack involves the transformation of the complex into a thiol and the conversion of thiourea into urea mediated by hydroxide ions. It is possible that this second reaction step is responsible for the solution changing to a white color (opaque), creating a metastable sol. This is probably the starting step towards the production of the sulfide. An increase in the temperature is then necessary to promote the elimination of HCl and the formation of sulfide bonds. The FT-IR spectrum is unable to give a full confirmation to this process: thiourea is in excess, the solvents mask all other signals and sulfide bonds cannot be seen in the accessible range [96, 96]

Further insights are provided by Raman spectroscopy (see Figure 16). Raman spectra were collected on a LabRAM Aramis confocal microRaman system, using a

backscattering configuration at 532 nm and spectrometer with a grating of 1800 grooves/mm coupled to an air cooled 1024*256 VIS CCD.

The spectra show a downshift of the $\upsilon(CS)$ at ca. 700 cm^{-1} in S2B with respect to S2B-thiourea, compatible with a coordination of thiourea with the metal ion(s) [96]. The Raman spectrum at lower wavenumbers (see Figure 16) also shows a simultaneous reduction of the signal related to the coordination of the metal chlorides with the alcohol/water, and an increase in the signal from the metal-sulfur bond. Both observations are compatible with the proposed reaction scheme.
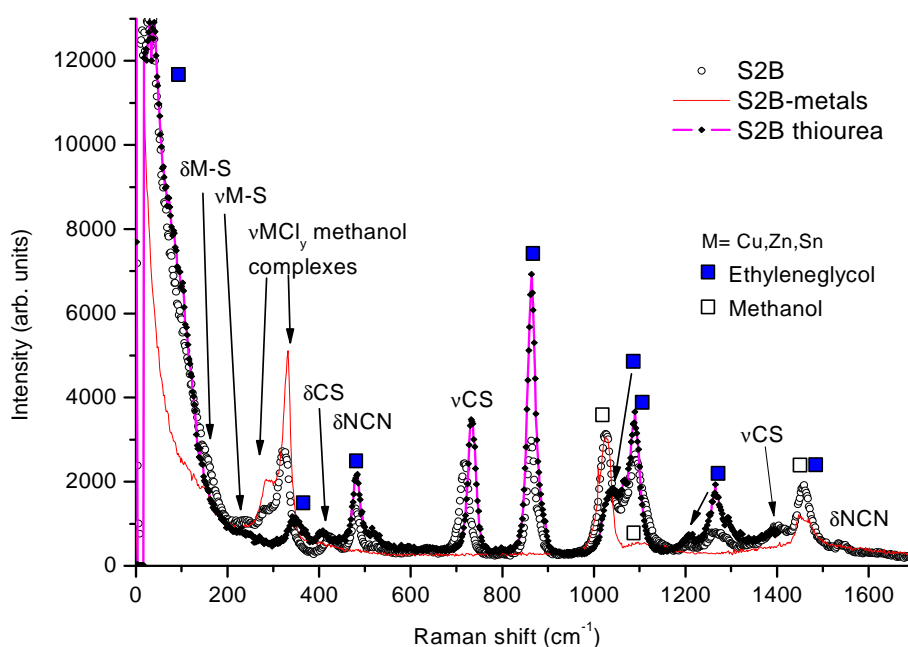
Figure 16. Raman spectra of the CZTS precursors S2B

It is possible that the increase in steric hindrance when moving from methanol to ethanol to ethylene glycol is responsible for the slowing down of the reactions in the corresponding cases and, ultimately, for the observed increase in stoichiometry control. The high density and polarity of the diol seems also the key for a better dissolution and stabilization of thiourea with respect to the water-based and

conventional sol-gel approaches usually proposed in the literature. (cf. R. D'Angelo et al. 2014: 3 [5]).

3.3.2   *Stability and formation of CZTS by DTA/TG*

To investigate the thermal stability of CZTS from the final solution S2B (yellow color, see Figure 11), samples were studied by DTA/TG in static air under atmospheric conditions. Approximately equal aliquots of ca. 23 mL of solution were placed in Al_2O_3 crucibles (100 mg capacity), subjected to a linear heating ramp between 25 °C to 900 °C at a heating rate of 10 °C/min in flushing nitrogen at 100 sml/min. A Setaram TG-DTA apparatus equipped with a LABSYS TG-ATD 1600 °C rod. The test measurements were made for the mass variation of the sample as a function of the temperature and the phase changes by the absorption or the emission of energy (heat flow) against temperature. Analyses of the heat-flow peaks were conducted using the Setaram proprietary software.

TG/DSC analyses were conducted in order to study the energy stability, decomposition and the phase transition behavior of the solution precursors S2B (Figure 17). All three metal precursors and thiourea showed the evaporation of the solvents (methanol, EG and H_2O complexes with the salt precursors) developing a weight loss of ~40 % at 160 °C (Endo process), after this step, the previous forms of CZTS will begin with the attack complex. Further annealing to 214 and 526 °C is accompanied by a slight weight loss of about 5 % (Exo process), ascribed to a loss of sulfur (from the thiourea) and chloride ions (from the metals precursor), which occur together with the probable formation of binary, ternary and the quaternary compounds like Cu_2SnS_3 +ZnS $\leftrightarrow$ $Cu_{2-x}Zn_{1+x}SnS_4$. At 525 °C formation of the quaternary CZTS compounds is completed, but above 550 °C the CZTS equilibrium is broken, and decomposition starts with a considerable weight loss [50], [97], [102].
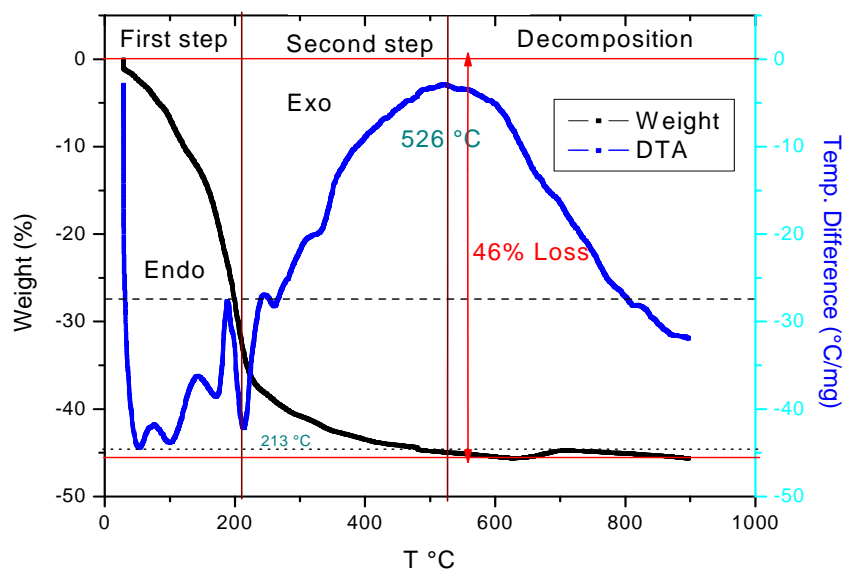
Figure 17. TGA (left) and DSC (right) of CZTS of the final precursor solution S2B (yellow solution). The heat treatment temperature should be 526 °C (crystalization completes, decomposition tremperature and the energy envolved).

However, this characterization confirmed how equilibrium has been achieved in one-step (cf. equation 2 in previous sections 2.4.1 and 2.4.2), to form non-stoichiometric CZTS by a non-vacuum method.

3.4   Results and discussion of the CZTS thin films from S2B after the annealing

3.4.1   Impurities from solutions with and without sulfur source

For an in situ study of crystallization and impurity phase identification by XRD, the CZTS sol precursor S2B was converted into crystalline kesterite by a high temperature annealing, as described in section 3.4.

All samples were characterized using grazing incidence X-ray diffraction with a fixed incidence angle $\Theta = 0.8°$. Diffraction data were collected on a PANalytical X'Pert MRD diffractometer, operated with a cobalt source (45 kV, 30 mA) and equipped with a polycapillary primary optics and a secondary flat graphite analyzer.

34

The X-ray diffraction patterns taken in grazing incidence on the films prepared from the proposed solutions (as described in Table 2) are shown in Figure 18 and 19. Kesterite (ICDD PDF2 card #26-0575) is present in all cases: impurities in some of the patterns are cassiterite (SnO_2, ICDD PDF2 card #41-1445) and copper sulfide (digenite Cu_xS, e.g. ICDD PDF2 card 24-0061). No further sulfide phase are directly identified, as their diffraction peaks might hide under (overlap with) those of CZTS, owing to a similarity between the CZTS and the zinc blende crystal structures [90], [97].
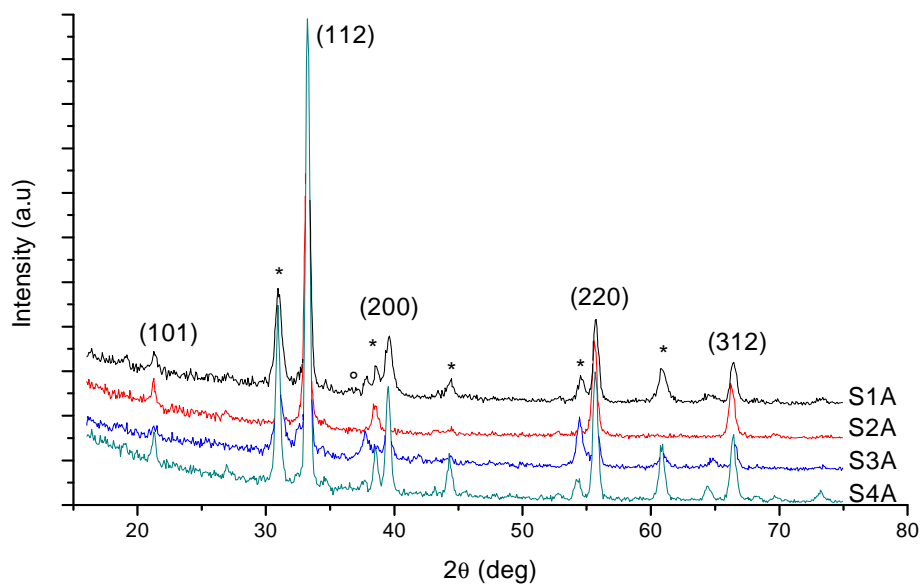
Figure 18. Grazing-incidence XRD patterns of CZTS films from the precursor SA starting with anhydrous tin chloride ($SnCl_4$) and with a excess on sulfur annealing.
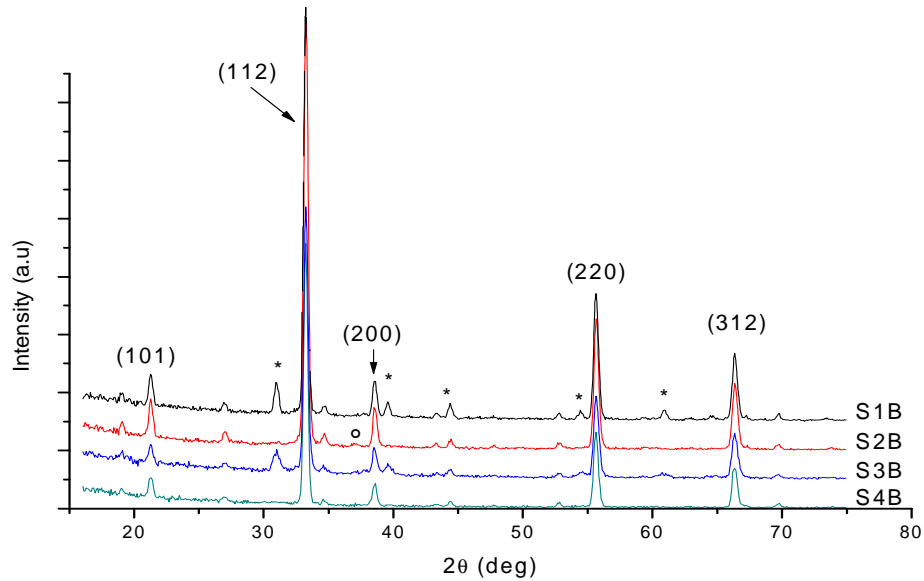
Figure 19. Grazing-incidence XRD patterns of CZTS films from the precursor SB starting with pentahydrate ($SnCl_4 \cdot 5H_2O$) and without a sulfur annealing.

A qualitative evaluation of the phase content is proposed in Table 1. The synthesis in methanol/ethylene glycol (S2B) leads to the formation of pure kesterite, as witnessed by the absence of peaks from spurious phases; this is also confirmed by Raman spectroscopy measurements and EDXS (Figure 20 and 21).

3.4.2 Surface composition

Raman spectroscopy was collected after the annealing step using an excitation wavelength of 532 nm. The same instrument described before (section 3.5.2), a LabRAM Aramis confocal micro-Raman system. Raman spectra do not reveal substantial information about the presence of secondary phases which are detectable by XRD (see Figures 18 and 19). The Raman spectrum (Figure 20) shows the main peaks of polycrystalline CZTS at 285 and 337 cm^{-1}, and a weak signal around 370 cm^{-1}, which are all as reported in literature (see Table 3) [86], [98].

The possible Raman modes of CZTS and other secondary phases are listed in table 3

Table 3. Raman peaks in $Cu_{1.8}Zn_{1.2}SnS_4$ thin film: CZTS and spurious phases.

Phase Raman shift (cm^{-1})	Phase Raman shift (cm^{-1})
CZTS	260, 289, 340, 366 (polycrystalline)
T-Cu_2SnS_3	297, 337, 352
Cubic- Cu_2SnS_3	267, 303, 356
Cubic ZnS	275, 352
Cu_2S	474
SnS	160, 190, 219 (not observed)
SnS_2	314, 215 (not observed)
Sn_2S_3	32, 60, 111, 224, 307-311

The presence of this weak peak reflects the remaining S in the absorber and therefore a mixed CZTS phase. The main CZTS (polycrystalline) is already weakly visible in the measurement at 366 cm^{-1} condition.
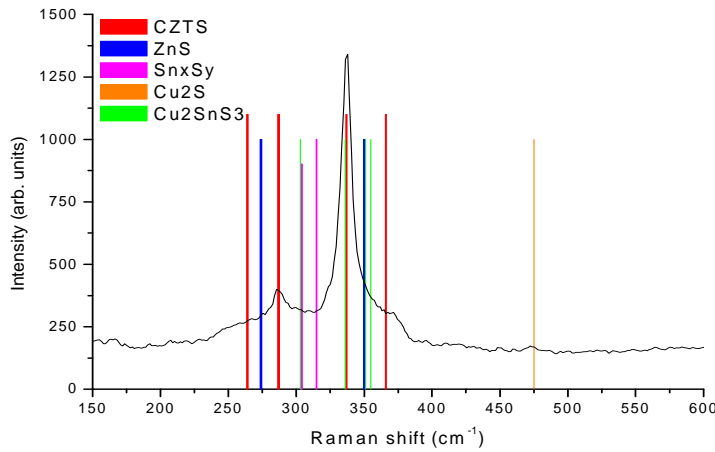
Figure 20. Raman spectrum of the S2B specimen deposited on glass and annealing without sulfur

The peak around 474 cm^{-1} probably stems from Cu_2S [50], [54-55] and not from a ZnS phase. The main peak corresponding to the ZnS phase is expected at 250 cm^{-1} [99]. It is still possible to detect at 274 cm^{-1} and a bit at 350 cm^{-1}, however, the probing depth of Raman is limited to less than a micron, and possible ZnS accumulation close to the

back contact may not be detected. This would be consistent with ZnS accumulation close to the back contact. XRD is not typically used to find this type of phase, since diffraction peaks overlap heavily with those of the principal kesterite phase [99].

If Zn is bound to S, UV Raman with a 325 nm excitation wavelength would be needed for resonant Raman measurement due to its higher optical band gap compared to ZnS [100]. The presence of the Cu_2SnSe_3 main Raman peaks around 302, 334 and 355 cm^{-1} cannot be excluded [63], although the ternary phase diagram (Figure 9) suggests its formation in this sample should be unfavorable (see Chapter 2 section 2.5).

EDXS was carried out with a Jeol JMS 7401F instrument, using the Bruker EDX. The study was aimed once again toward the spurious phases, especially in specimens SA (see Table 2), but also to have a better understanding of the ratio of different cations. In fact, it should be noticed that a slightly unbalanced ratio between Cu and Zn, favoring Zn (EDXS) led to the desired stoichiometry $Cu_{1.8}Zn_{1.2}SnS_4$ with a target ratio $Cu/(2 \times Zn)=0.75$, which can be advantageous for solar energy harvesting applications. Figure 21 shows a graphic with more details using the estimated EDXS result for every solution ID.
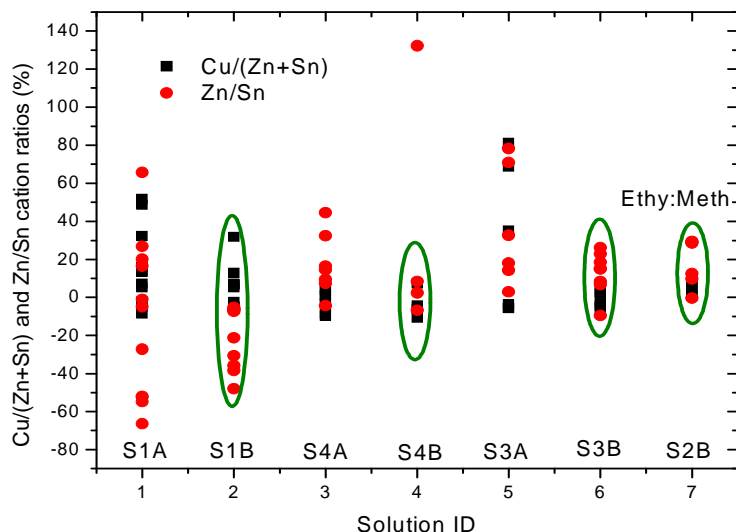
Figure 21. Estimetd stoichiometry for the different tested solvents (several measured were performed for each solution ID).

These data indicate that sulfurization is not always necessary to obtain an optimal stoichiometry, a point that can be verified with solutions S3B and S2B presenting less scattering. The resulting ratios of metal elements [Cu/(Zn+Sn) and Zn/Sn respectively] of the solutions with a closer stoichiometric distribution were around 0.82 and 1.35 for S3B and 0.84 and 1,29 for S2B (see Figure 21), showing that Cu-poor and Zn-rich compositions are sustained up to 550 °C with longer annealing times. Previous reports [100-101] have demonstrated that a Cu-poor condition leads to the formation of Cu vacancies, which generate shallow acceptors in CZTS, while a Zn-rich condition suppresses Cu substitutions at Zn sites, which increases the concentration of deep acceptors [27].

Moreover comparing the various specimens, the sulfurization step seems to be responsible for the formation of the extra copper sulfide. The choice of the solvent also has an effect on the stabilization of the tin ion, leading to the formation of tin oxide together with kesterite.

3.4.3   *Morphological study*

For compositional/morphological characterization, the samples were analyzed using A Jeol JMS 7401F Field-Emission SEM equipped with a Bruker EDX detector.

Figure 22 shows elemental mapping studies on $Cu_{1.8}Zn_{1.2}SnS_4$ thin films composition. No contrast is observed in elemental map images which imply that the films are chemically homogenous. According to the phases identified by the Raman studies ZnS is an insulator, SnS, Cu_2SnS_3, Cu_3SnS_4, Sn_2S_3 are semiconductors, whereas $Cu_{2-x}S$ is a degenerate semiconductor [3],[20], hence a separate segregation of any of these phases was anticipated from elemental mapping studies. However, elemental maps could not reveal any segregation of phases.
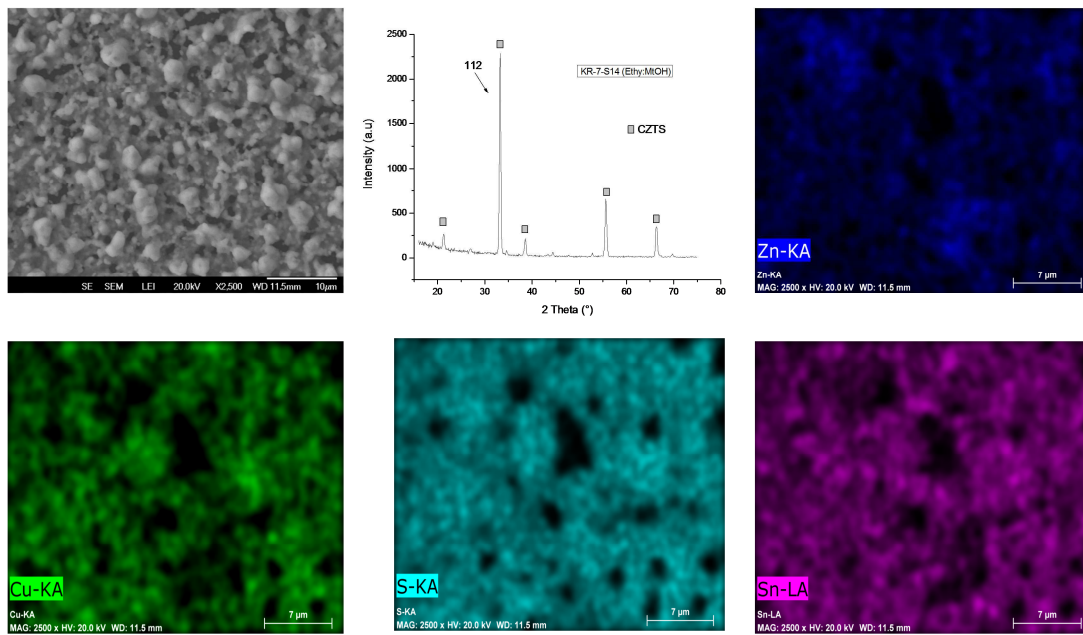
Figure 22. Elemental maps of Cu, Zn, Sn and S along with corresponding microstructure for $Cu_{1.8}Zn_{1.2}SnS_4$ thin film from the precursor solution S2B

Since the electron beam penetrates down to the substrate in elemental mapping, the applied voltage (20 kV) could be one of the possible reasons why the phase separation could not be revealed when the phases are isolated in spatial distribution [27]. The other possible reason could be that the secondary phases, which are quantitatively less or appear in isolated regions, could not be identified in the area under scan.

However, in Figure 23 (left) it can be observed that a micrograph collected at lower accelerating voltage gives same contrast and brightness, whereas the image collected at higher accelerating voltage shows clear contrast in the microstructure. This confirms that the secondary phase is buried under the surface which belongs to Cu_3SnS_4 phase.
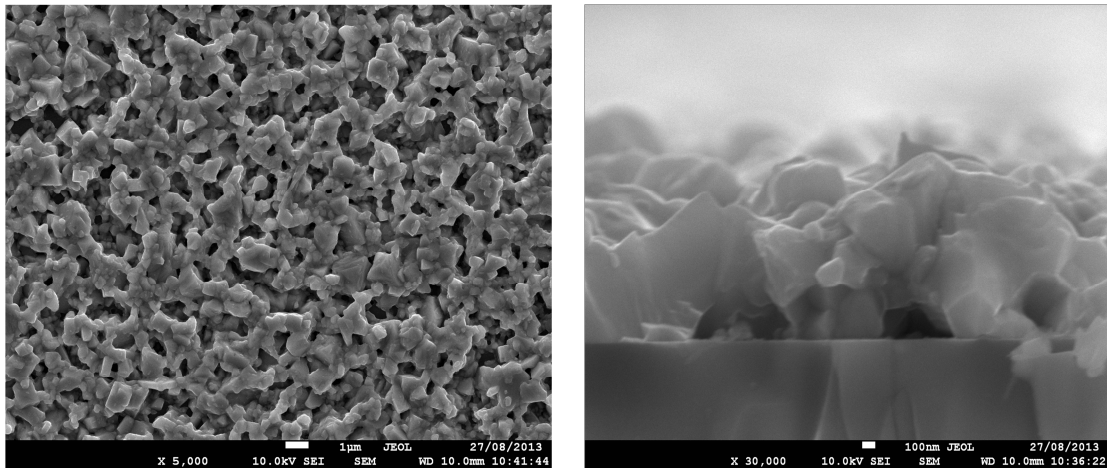
Figure 23. SEM and cross section images of $Cu_{1.8}Zn_{1.2}SnS_4$ thin film from the precursor solution S2B recorded on a lump morphology at 10 kV accelerating voltage with a magnification at (left) 1 μm and (right) 100 nm respectively.

On the other hand, the morphology shows a non-uniform distribution of agglomerated particles with well-defined voids and boundaries; it is also seen where the tin source affects the quality and microstructure of the resulting material. The soluble but volatile anhydrous tin chloride ($SnCl_4$) used for the solutions S [1, 2, 3, 4] A (see Table 2) is always employed in the literature. The less dangerous pentahydrate ($SnCl_4\bullet5H_2O$) [101] used for the synthesis of the S2B solution (solution with the best results reported), gives less contamination and a reduced tendency, for the films, towards island growth, which is shown in the cross section of the Figure 23 (right). Further, tin (IV) pentahydrate does not evaporate and can thus guarantee a better stoichiometry control.

3.5 Tentative test of the S2B specimen for solar cell applications

This section reports the optical properties of the specimen S2B deposited and annealed in the UNITN laboratory and measured in collaboration with ENEA-Research Center in Rome. The cross section and the band gap energy were analyzed, in order to develop a test device. However, these analyses correspond just to an attempt to verify the quality of the material, despite the morphological problems described in the previous section.

The cross section of the final CZTS thin-film solar cell can be observed in Figure 24 (left). The CZTS absorber layer is clearly visible with a thickness of about 1.5 μm, as well as kesterite crystals of a few hundred nanometers in size. No MoS_2 layer was detected under the absorber layer. The CdS buffer layer and the sputtered ZnO/ZnO:Al top electrode are observed on top of the absorber layer. Following the theory explained in the section 2.5, the CZTS layer does not show any trace of impurities like SnO_2^{++} Cu_2S^{++}. However, owing to flaws of the final morphology (most probably, short-circuits), it was not possible to measure current-voltage characteristic curve for the CZTS thin film device; therefore, the CZTS was tested measuring the optical properties in order to obtain the band-gap of the CZTS thin film after the annealing step.

Starting from the transmittance spectra of a CZTS films and using the film thickness, the absorption coefficient α is obtained as:

$$\alpha = 1/t \ln 1/T$$

where t is film thickness and T is the transmittance of the film. Figure 24 (right) shows the Bandgap from the absorption coefficient (α) of CZTS films from two different samples using the S2B precursor solutions.

The transmittance spectra of two S2B precursors and the corresponding CZTS film are reported. The latter was used to obtain the absorption coefficient (α) of the final materials and the energy gap was estimated using E04 [84], [86], defined as the energy value at $\alpha = 10^4$ cm^{-1}. In the sample reported in Figure 24 (left) the resulting value of E04 for the sample S2B is 1.52 eV (red Tauc-plot); this can be considered as an acceptable value in comparison with those reported in the literature [24], [86], taking into account the morphological defects. As a comparison, 1.61 eV (blue Tauc-Plot) is the value of a typical example of CZTS done by sputtering method (from ENEA laboratories). The absorption edge of the precursor S2B has a high wavelength, thus revealing optimal bandgap energy around 1.52 eV of the deposited materials. This effect of the wavelength together with the morphological effects can be consistent both with a strongly disordered CZTS and with the presence of secondary phases such as Cu_2SnS_3 (Eg~1.35 eV) or SnS (Eg~1.30 eV) [11], [16, 17], [84].
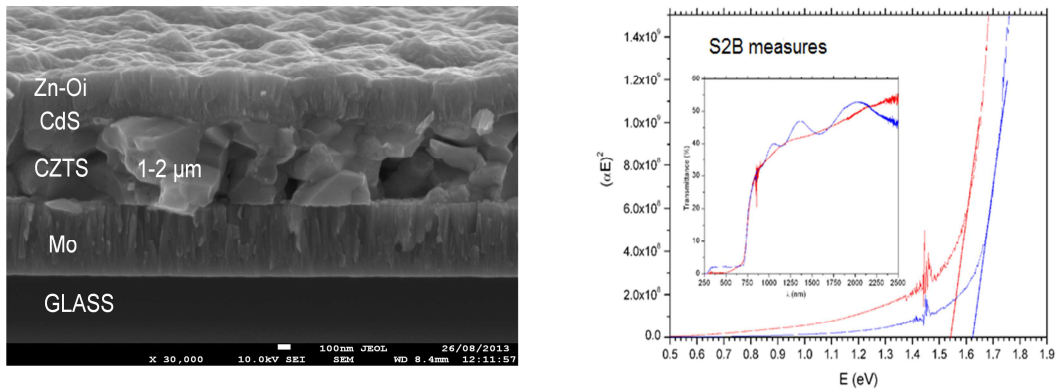
Figure 24. CZTS thin film cross section of specimen S2B (to the left) produced at the University of Trento. CZTS optical properties of specimen S2B (to the right): the red line refers to a sample deposited at the UNITN and mesured by ENEA; blue line is for a reference film produced by ENEA labs by sputtering.

3.6 Conclusions

The optical properties obtained are in accordance with the data reported in literature [4], [24] while the cross section for the thin film device showed grain growth that can cause short-circuit, decreasing the V_{oc} value. This behavior of a high band gap and low V_{oc} has been already described in section 1.3. More efforts are necessary to optimize the process, and this requires improved experimental conditions, besides possibly changing precursor (tin chloride): specific attention should be devoted to improve the morphology of the CZTS absorber layer, avoiding formation of large pores while, at the same time, controlling the stoichiometry and absence of spurious phases, so to increase the overall solar-cell performance.

Chapter 4

Monodisperse CZTS processed by colloidal method synthesis

The following chapter describes a new approach based on a hot injection method for large scale synthesis of CZTS nanoparticles, minimizing the use of organic solvents. Nanocrystals were synthesized starting from metal chlorides and pure sulfur powder and using Oleylamine (OLA) as a capping agent. The first part shows the microstructure characteristics (size distribution, shape, and stoichiometry) and optical properties evaluated. The investigation confirmed that the use of metal chlorides, though low-cost precursors, makes difficult the control of composition, size and final shape of the nanoparticles. Since stoichiometry is fundamental for high efficient films, the second part of this chapter is focused on the control of the composition. In particular, the effects of the amount of sulfur powder (sulfur source), solvent and zinc precursor on the chemical and physical properties were investigated

Part A of this chapter has been published in:

"**Chloride-based route for monodisperse CZTS nanoparticles preparation**".

C. L. Azanza Ricardo[a], F. Girardi[a], E. Cappelletto[a], R. D'Angelo[a], R. Ciancio[b], E. Carlino[b], P. C. Ricci[c], C.Malerba[d], A. Mittiga[d], R. Di Maggio[a] and P. Scardi[a].

a University of Trento, DICAM, Via Mesiano 77, 38121, Trento, Italy.

b CNR-IOM, TASC Laboratory, Area Science Park, Basovizza S.S. 14 Km 163.5, 34149 Trieste, Italy

c University of Cagliari, Italy

d ENEA C.R. Casaccia, (S.P. 064), Via Anguillarese 301, 00123, Roma, Italy

This part A of the project was carried out with the collaboration of several researchers. A brief description of the responsibilities of each author is shown below:

Cristy Leonor Azanza Ricardo worked as an advisor throughout all this part of the project. The hot-injection synthesis was carried out by R. D'Angelo in collaboration with F. Girardi and E. Cappelletto. Depositions on glass were done by R. D'Angelo. R. Ciancio and E. Carlino performed the TEM measurements and analysis. P.C. Ricci was responsible of the Raman measurements and analysis. Alberto Mittiga and Claudia Malerba were responsible of carrying out the optical and SEM cross-section analysis at ENEA labs; more observations were made by R. D'Angelo at the University of Trento. Rosa Di Maggio and Paolo Scardi worked as supervisors of the entire work, with specific contributions in interpretation of the results and part of the writing of papers.

4.1   Introduction

The production of high quality Cu_2ZnSnS_4(CZTS) nanoparticles still receives a growing attention for fabrication of absorber layers in photovoltaic devices. Recent work outlined the possibility of obtaining different CZTS polymorphs [102], tetragonal or hexagonal, depending on the capping agent and/or the metal sources. The major influence of the sulfur source on the final shape of nanocrystals has also been investigated and fully acknowledged. Complex and expensive metal sources are required to achieve a fine control of composition [103]. When using cost-effective and simpler starting materials such as chlorides, a large amount of Zn cations is not actively used in the synthesis, as an effect of the large difference between the stability of zinc complex and copper and tin ones [104]. This is the main reason why most authors use a Zn excess to compensate for its loss in the preparation [105]. The best performance, for a device using CZTS as absorber layer in thin film solar cells, has been historically obtained working within a narrow compositional window, with Cu-poor and Zn-rich stoichiometry [64-66]. In fact, this condition is desirable to prevent formation of both detrimental copper-sulfide phases [64] and harmful intrinsic defects predicted by ab-initio calculations (such as Cu^{3-}_{Sn} and $Cu_{Zn}+Cu_{Sn}$) [63], [73, 74]. It

follows a new simple approach to gram-scale CZTS nanoparticle production minimizing the amount of organic solvents. It is based on the hot injection method, a widely used procedure for colloidal nanocrystals production in which three main elements may be identified: precursors, organic surfactants and solvents (in some cases, surfactants also serve as solvents). This method consists of injecting a cold solution of precursors into a hot surfactant, leading to the immediate nucleation and growth of nanocrystals. This is a convenient route to the synthesis of a wide range of semiconducting nanocrystals, providing good control over composition and morphology.

A key point of this work is that the nanocrystal synthesis was performed starting from metal chlorides as metal sources and pure sulfur powder, and using Oleylamine (OLA) as capping agent (acting as surfactant and solvent at the same time) [2]; in this way we avoid organic stabilizers or more complex and therefore more expensive reagents, such as metal acetylacetonates. Through the optimization and the control of synthesis parameters, it is possible to obtain a good (gram-scale) amount of high quality nanoparticles, in terms of morphology and composition, even if prepared by using commercial (70% grade) OLA [33, 34]. This approach will enable low-cost fabrication of solar cell devices through techniques such as drop casting, dip coating, spin coating, or printing of the resulting CZTS nanocrystal solution.

4.2 Experimental details

Copper (II) chloride dihydrate ($CuCl_2$ $2H_2O$, Aldrich,>99.0%), Zinc chloride ($ZnCl_2$, Aldrich >98%), Tin (II) Chloride ($SnCl_2$ $2H_2O$, Aldrich 98%) were dehydrated at 200 °C under vacuum. Sulfur powder (Aldrich), oleylamine (OLA, Aldrich, 70%), Toluene (Aldrich, 99.9%) and Ethanol (Aldrich, >99%) were used without further purification.

CuCl₂
ZnCl₂
SnCl₂
+
Oleylamine

vacuum
|
heated to 130 °C
|
when the mixture turned brow
degassed and refilled with N₂
|
vacuum
|
heated to 270 °C
injected 3 mL of Sulfur source
|
30 min
|
cooled down to 60 °C
|
+
5 mL Toluene and 25 mL ETOH
|
centrifugal separation at 4000 rpm for 10 min
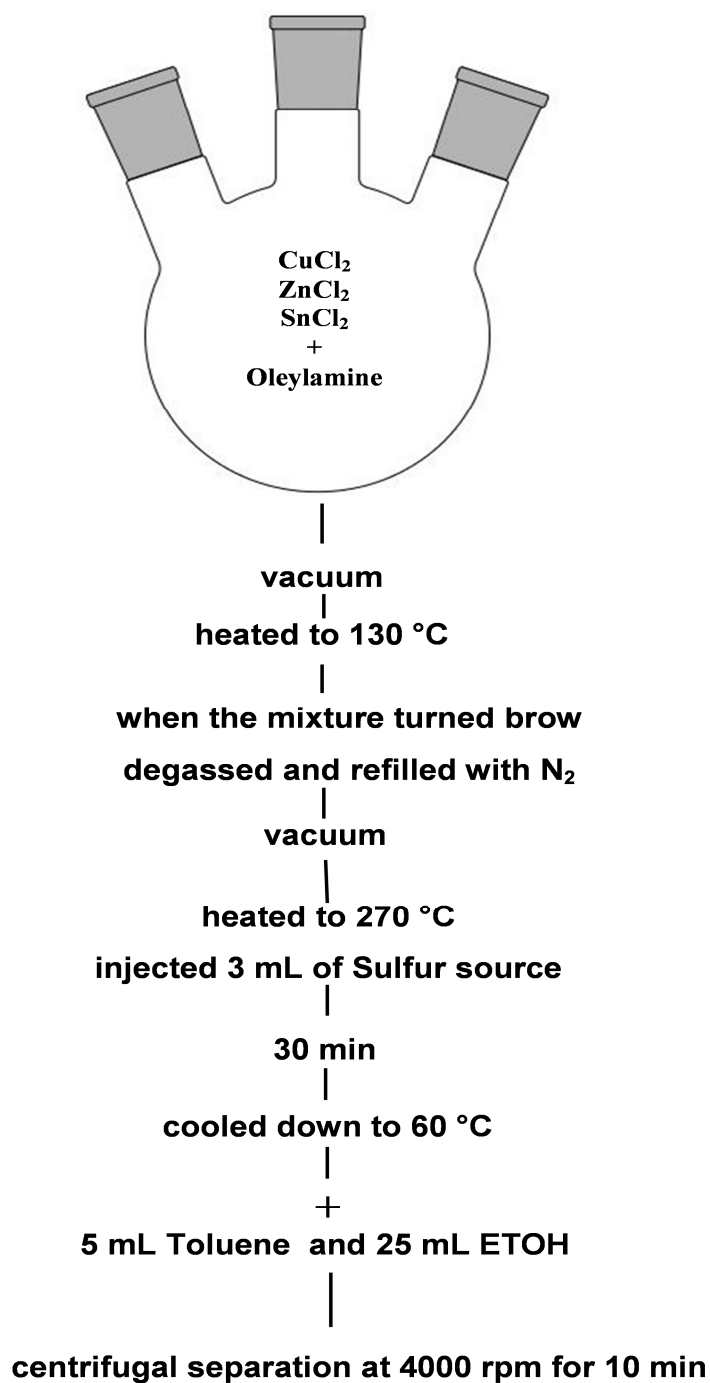
Figure 25. Scheme of the principal steps to synthetize the CZTS nanoparticles by hot injection method.

CZTS nanoparticles were synthesized according to the scheme in Figure 25. In a typical reaction, 4 mmol of $CuCl_2$, 6.22 mmol of $ZnCl_2$ and 2.16 mmol of $SnCl_2$ (Cu:Zn:Sn=2:3.11:1.08) were mixed into a 100 mL three-neck round bottom flask

containing 20 mL of OLA. The system was connected to a Schlenk line apparatus, in order to carry out all the experiments in a standard air-free condition. Oleylamine was added both as solvent and as capping agent for the nanocrystals.

The mixture was heated to 130 °C, when the color became brown. At this temperature the flask was degassed and refilled with nitrogen six times and kept under vacuum for 10 minutes. The temperature was raised to 270 °C and then 8 ml of a sulfur/OLA 1M solution was rapidly injected under strong stirring and N_2 flux. After the hot injection the mixture turned black. The mixture was kept at 270 °C for 30 minutes and then naturally cooled to room temperature [2]. The final suspension of nanoparticles was first mixed with a solution of toluene:ethanol 1:5 by volume and centrifuged for 10 min at 4000 rpm in order to separate the solvent from the "ink" containing the CZTS nanoparticles. At the end of the synthesis process, an amount of 1.10 g of dried nanoparticles was obtained.

Figure 26. Final Ink suspended in toluene

The ink was prepared adding 1–2 ml of toluene to the nanoparticles and sonicating for 15 min (Figure 26). Films were obtained by spin-coating technique and residual toluene was removed in oven at 150 °C for 5 min. Silicon wafers, which provide

minimal background contribution beside a smooth surface, were used as substrate for X-ray diffraction (XRD) measurements, whereas soda lime glasses for Raman spectroscopy and optical characterization. A drop of a suspension of the CZTS nanoparticles in toluene (1:10) was spread onto a Cu grid, dried in air and observed by Transmission Electron Microscopy (TEM).

The hydrodynamic size of the CZTS nanoparticles was characterized using a DelsaNano (Beckman Coulter) instrument for Dynamic Light Scattering (DLS). DLS measures the intensity of a laser light scattered by suspended particles. The average hydrodynamic diameter of the particles is derived from the temporal evolution of the scattered light intensity using the Stokes-Einstein equation [106]. Mixtures were sonicated for 15 min using a bath sonicator (40 W, 35 kHz, Elma 460/H) before the size analysis. All data were collected at room temperature (25 °C), kept constant by the DelsaNano C instrument. Reliability of hydrodynamic size values was ensured, according to a standard procedure, by 10 scans for each analysis. The optical properties were investigated by transmittance and reflectance measurements in the 250-2500 nm wavelength range, using a Perkin Elmer Lambda9 spectrophotometer equipped with an integrating sphere. Raman scattering measurements were carried out in backscattering geometry with the 1064 nm line of a Nd:YAG laser. Measurements were performed in air at room temperature with a compact spectrometer BWTEK i-Raman Exintegrated system. The powder diffraction pattern was collected on a Phillips XPert MRD diffractometer, using $Co_{K\alpha}$ radiation filtered by a diffracted-beam graphite analyzer. This instrument provides a pseudo-parallel beam with a divergence of about 0.3° by using a polycaplillary lens. Preliminary morphological analysis was carried out using a Zeiss Supra 40 field-emission gun (FEG) scanning electron microscope (SEM) equipped with a Gemini column and In-lens detectors yielding increased signal-to-noise ratio. The nanostructure of the CZTS nanoparticles was thoroughly determined by high resolution transmission electron microscopy (HRTEM) and high angle annular dark field (HAADF) scanning TEM (STEM) analyses. The TEM/STEM experiments were carried out using a JEOL 2010 UHR field emission gun microscope operated at 200 kV with a measured spherical aberration coefficient Cs of 0.47 ± 0.01 mm, resulting in a spatial resolution at optimum defocus of 0.19 nm.

The microscope is equipped with an Oxford system for energy dispersive X-ray spectroscopy (EDXS) studies. High-Angle Annular Dark-Field (HAADF) images were acquired using an illumination semi-angle of 12 mrad and a collection angle $88 \leq 2\theta \leq 234$ mrad to enhance the sensitivity and detect variation in the specimen average atomic number [107, 108]. EDXS analyses were carried out in STEM mode by scanning an electron probe of 0.5 nm to determine accurately the chemical composition of nanoparticles.

4.3   Results

The nanoparticles synthesized by hot injection were spherical and monodisperse. The HRSEM micrograph shown in Figure 27 (left) points out that they tend to self-assemble with a planar and homogeneous distribution. Nano-particle size distribution was determined by analyzing a large set of SEM images. Figure 27 (right) shows the size distribution measured by DLS (providing a hydrodynamic average diameter of 16.2 nm and a Polydispersity Index (PI) of 0.014, which indicates a monodisperse suspension) compared to that measured by SEM images; giving a size distribution peaked at 17±4 nm. HRTEM investigations confirm the nanoparticles tend to form self-organized close-packed monolayers. Rounded nanoparticles with a diameter of about 16 nm were observed by HRTEM in Figure 28a, along with a minor fraction of smaller-size irregularly shaped particles. The corresponding Selected Area Electron Diffraction (SAED) pattern in Figure 28b is compatible both with hexagonal structure of CZTS as well as those of the tetragonal CZTS.
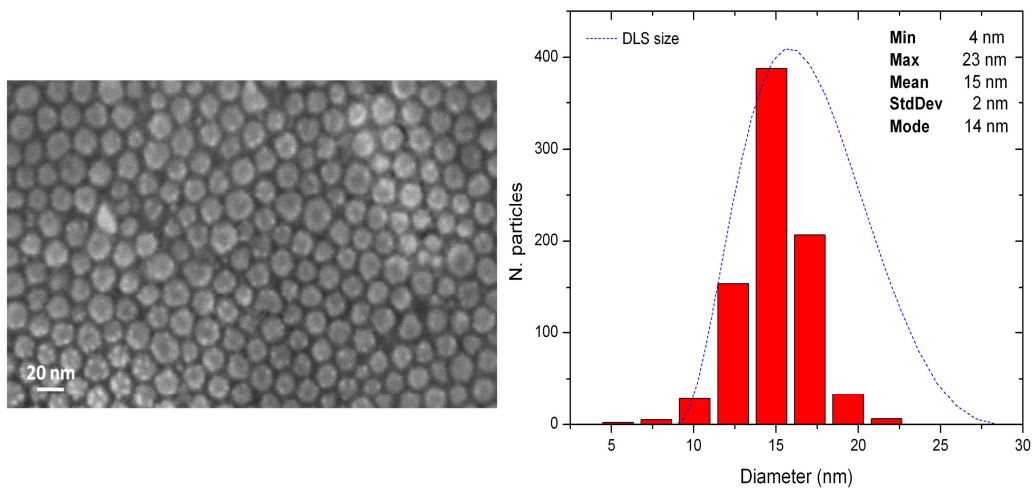
Figure 27. HRSEM micrograph showing the self-assembling behaviour of the nanoparticles (left); size distribution obtained from HRSEM and corresponding DLS measurements (right).
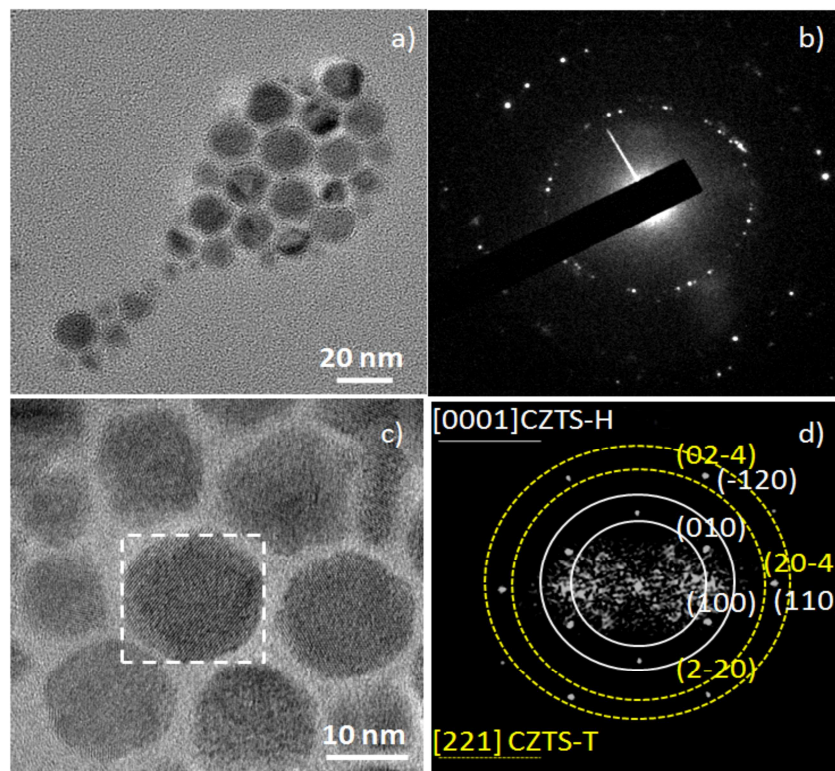
Figure 28 (a) HRTEM micrograph of a representative cluster of nanoparticles and (b) related Selected Area Electron Diffraction showing rings compatible with the CZTS hexagonal and tetragonal crystal structure; (c) HRTEM image highlighting the presence of contrast variation within the nanoparticles compatible with a core-shell structure (dashed box area); (d) representative diffractogram of an individual nanoparticle showing the presence of both the CZTS hexagonal and CZTS tetragonal pattern, respectively in the [0001] and [221] zone axis.
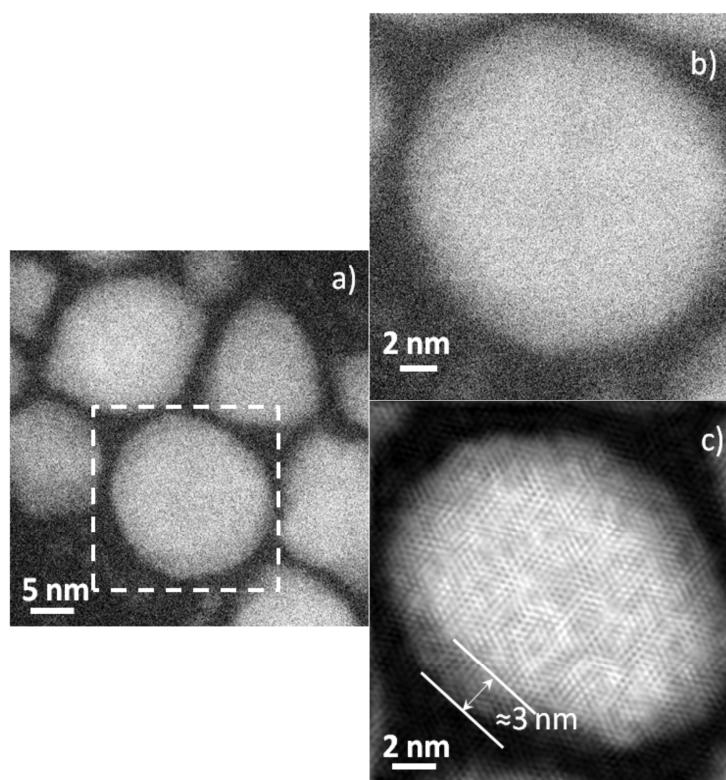
Figure 29. HAADF-STEM images of the nanoparticles. In a) a rounded CZTS nanoparticle is marked by the dashed box where the presence of contrast variation between core and shell can be seen and appreciated in better detail in b). An isolated CZTS nanoparticle with evidence of a core-shell structure is shown in c), with the corresponding Inverse Fast Fourier Transform shown.

A closer HRTEM inspection of nanoparticles reveals a slight contrast difference between the core and the peripheral areas, as shown in Figure 28c. Diffractograms recorded over those nanoparticles show a pattern with the characteristic spots of the [0001] zone axis of the CZTS/ZnS hexagonal cell along with those of the [221] zone axis of the CZTS tetragonal cell. A representative diffractogram is displayed in Figure 28d where the spots are indexed and the two contributing patterns are highlighted by circles (dotted for CZTS tetragonal and solid for CZTS hexagonal/ZnS hexagonal) for an easy visualization. These observations point out a possible core-shell structure: further support to this interpretation stems from HAADF/STEM and EDXS. The HAADF image contrast of Figure 29a indicates a compositional variation across the nanoparticles. As visible in the higher magnification image of Figures 29b and in the HAADF image in Figure 29c, (obtained after Gaussian filtering in the reciprocal space to highlight the lattice fringes visibility in the particle), image contrast variations can

be appreciated between the core and the periphery of the nanoparticles. The brighter contrast of the core is compatible with a higher density region. From the HAADF image of Figure 29c the shell thickness can be estimated in about 3 nm. EDXS line-scan profiles collected across the nanoparticles provide further insight into the core-shell architecture and reveal the possible presence of additional phases segregating during the synthesis.
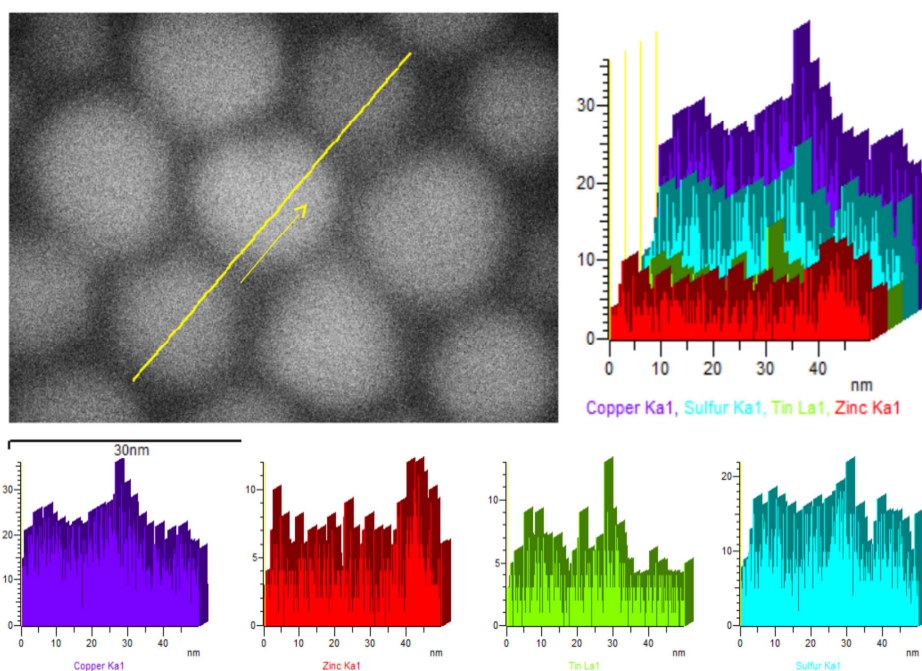
Figure 30. HAADF/STEM image of self-assembled nanoparticles. Line and arrow indicate the area where the EDS line-scan profiles have been acquired, providing the EDS elemental profile of Cu (violet), Zn (red) Sn (green), S (blue) shown below.

Figure 30 shows the STEM-EDXS line-scan taken along the yellow line. The signals of Cu, Zn and S follow an almost constant and homogeneous profile across the first two nanoparticles on the left-bottom, whereas a clear increase in the Zn signal (red profile) and a corresponding drop in the Cu (violet) and in the Sn (green) profiles is measured in the last nanoparticle on the right-upper part of the line-scan. This evidence is consistent with the presence of ZnS nanoparticles, segregating apart as a result of the large zinc excess in the starting precursor. The sampling across the TEM specimen confirms that most nanoparticles are CZTS with a rounded shape, whereas

the minority ZnS nanoparticles are of smaller size and/or characterized by different and irregular shapes (i.e., triangular or trapezoidal prisms). It is worth noting that the presence of ZnS in CZTS samples is often reported in the literature and seems not to be detrimental to the device performance. Further structural information was provided by XRD and Raman spectroscopy [109].
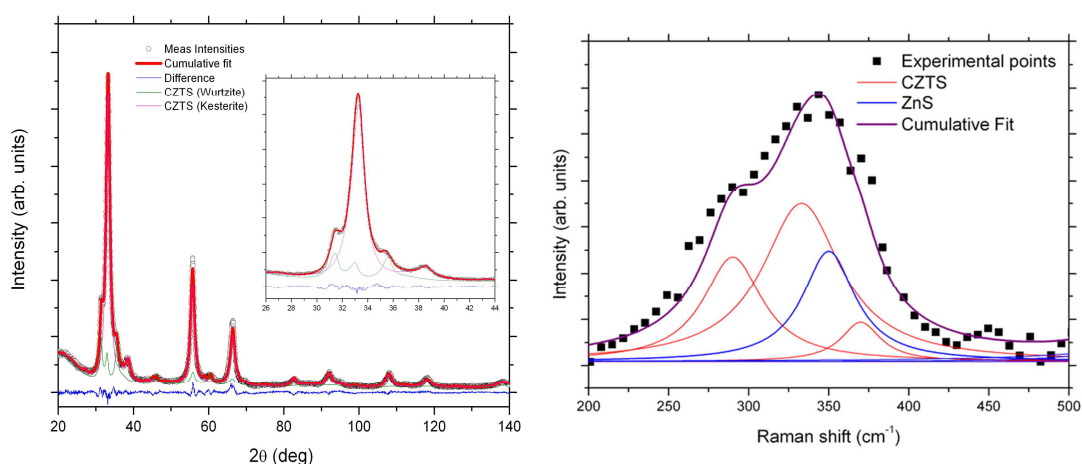
Figure 31. a) XRD pattern (left) and b) Raman profile (right) of nanoparticles deposited on silicon wafer and soda lime glass respectively.

The XRD pattern in Figure 31a shows two phases: tetragonal kesterite (CZTS-T) and hexagonal wurtzite (CZTS-H). The highly disordered hexagonal phase has been first reported in [109] and frequently considered afterwards for understanding the process of nucleation and growth of CZTS nanoparticles [110]. The XRD pattern was analyzed by the Rietveld method using TOPAS 4 [111], assuming two independent phases, as stated before. The tetragonal phase was modelled with the kesterite space group (I-4) leading to cell parameters compatible with a pseudo-cubic structure (a=0.5427 nm and c=1.0854 nm; c/2a=1), whereas the resulting average crystalline domain size was ~20nm, compatible with microscopy and DLS results. A quantitative phase analysis revealed about 25% of hexagonal phase. It is worth noting that to accurately fit the data a high microstrain level (2%) was required for modelling the hexagonal phase. The inset in Figure 31(a) shows the details of the XRD data analysis for the principal peak of the tetragonal (112) and hexagonal (001) phases. The Raman spectroscopy pattern shown in Figure 31(b) clearly identifies the CZTS phase (338;

54

293, 335, 372 cm^{-1}) with a small amount of ZnS (352 cm^{-1}). There is no positive evidence of the presence of CTS ternary compounds, although small amounts cannot be totally ruled out based on the observed data quality (large peak broadening).

Optical properties were investigated by spectrophotometric measurements in the 250-2500 nm wavelength range. Transmittance (T) and Reflectance (R) spectra were collected to measure the absorption coefficient (α) according to the expression:

$$\alpha = \frac{-1}{d} ln \left[\frac{T}{(1-R)^2} \right]$$

where d is the film thickness, evaluated from SEM cross-sections of the specimen.

To avoid any subjectivity in the band gap energy (Eg) evaluation from graphical method (Tauc plot in Figure 32b and c), Eg can be estimated with the parameter E04, i.e., the energy value at $\alpha=10^4$ cm^{-1}[86, 99, 112] (see Figure 32a). In this way, the energy gap was found to be 1.6 – 1.65 eV, which is within the range, 1.48 – 1.65 eV of the Eg values reported in the literature [24], [100], [113, 114]. As expected, no band gap widening effect due to quantum confinement is observed.

The widening effect ($\Delta E=E_g-E_{g0}$) can be estimated using the approximated expression:

$$E_g - E_{g0} = \frac{h^2}{8m_{eh}R^2}$$

where R is the nanoparticle radius and m_{eh} is the reduced mass of electron and hole [$m_{eh} = m_e m_h/(m_e + m_h)$]. Using m_e=0.186 m_0 and m_h=0.48 m_0 [115] (where m_0 is the free electron mass), the quantum confinement effect on the band gap energy expected in our sample (with R 10 nm) is found to be negligible ($\Delta E = 7$ meV). It is worth to notice that the ZnS phase, with an energy gap wider than that of CZTS, would not give any contribution to the measured absorption spectra.
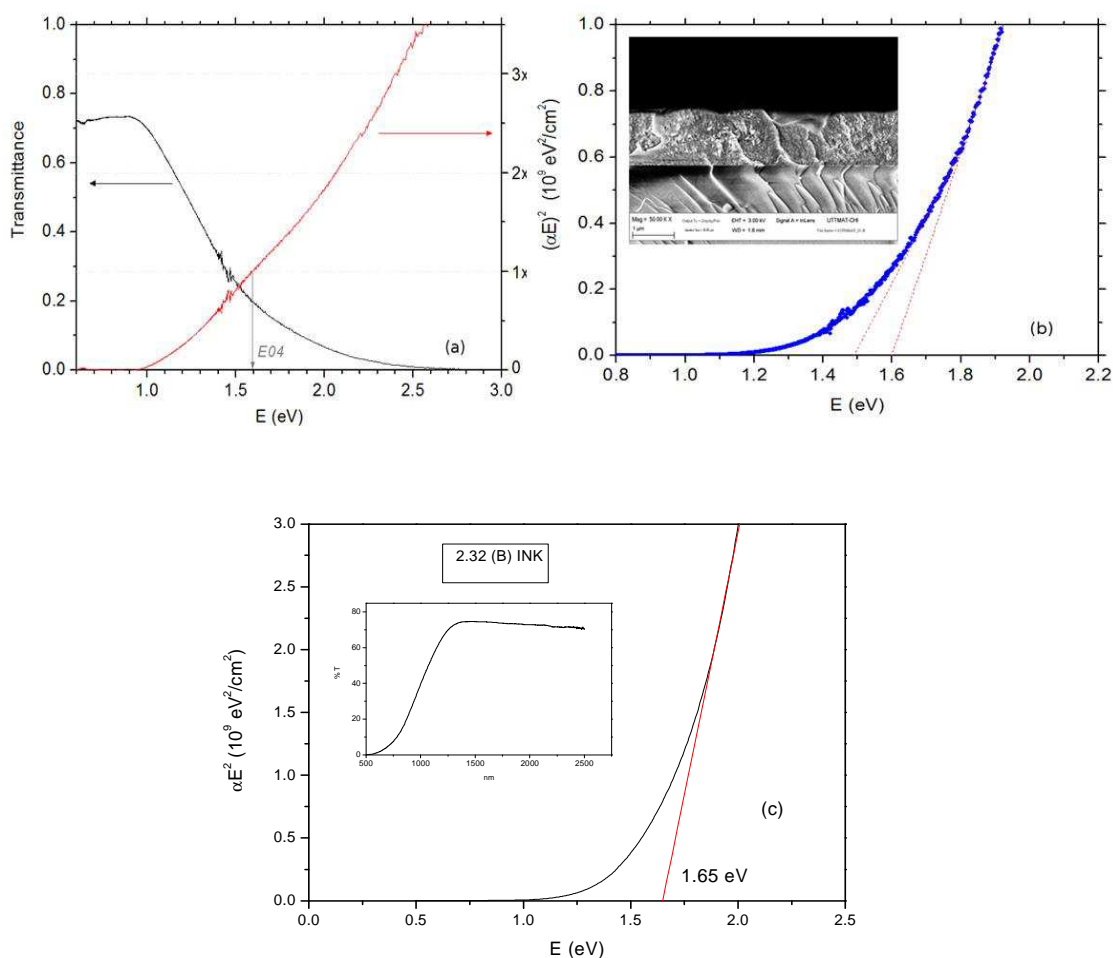
Figure 32. Transmittance, absorption spectra (a) Tauc plot and corresponding SEM cross section analyzed at ENEA (b) and Tauc plot, transmittance - absorption spectra measurements at UNITN (c) of a typical nanoparticle film deposited at UNITN by spin-coating on soda lime glass.

4.4 Discussion

As suggested by Tan et al. 2014 [116], the formation of CZTS nanoparticles can be considered as a three-step process: (i) formation of $Cu_{2-x}S$; (ii) diffusion of Sn cations leading to the CTS ternary compound, and (iii) diffusion of Zn cations to form the final CZTS phase. Exploiting the copper stoichiometry defect with an excess of Zn prevents the formation of CuS and CTS, the most undesirable phases in these systems and also in our samples favors the formation of ZnS [108], confirmed by Raman and STEM-EDXS analysis, in a such low amount to be negligible in the modelling of XRD data. At this regard, tetragonal (pseudo-cubic) and hexagonal CZTS phases are

shown by XRD spectra and SAED analysis. The evidence on the actual distribution of the two phases comes from the high level of microstrain revealed by the XRD analysis, which may originate from the presence of an interface between the two polymorphs. Indeed, it is known that the strong correlation between the two structures can induce a phase transformation (from hexagonal to tetragonal and vice-versa) by atomic layer faulting [117]. The mechanism is similar to the well-known fcc-hcp phase transformation, where the $[111]_{fcc}$ and $[001]_{hcp}$ directions are equivalent [117]. As a consequence of the self-assembling tendency of nanoparticles in the most favorable hexagonal-like crystallographic orientation, SAED would not be sufficient to identify the two polymorphs: as a matter of fact, in the diffractogram of Figure 29(b), the d-spacings of the some diffraction spots of the (tetragonal) [221] zone axis closely match those of the (hexagonal) [0001] zone axis (e.g., T(02-4)/H(-120), T(20-4)/H(110), T(-220)/H(2-10)). Moreover, it is relevant to point out that HRTEM images of particles, slightly misoriented with respect to the electron beam, enlighten the presence of defective areas (see Figure 33).
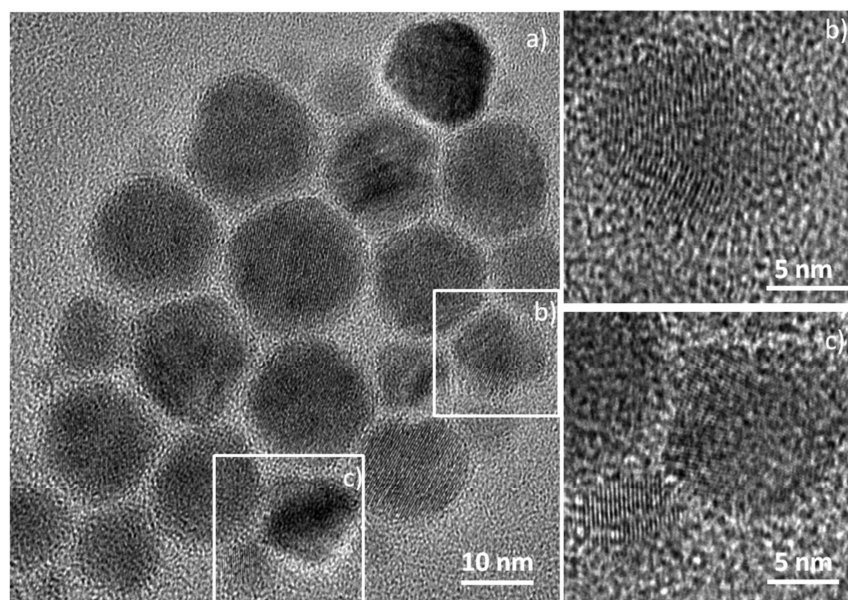
Figure 33. HRTEM images showing structural defects.

According to the layer faulting mechanism, both structures may coexist within a single nanoparticle. Several hypotheses can be made on their distribution, and the simplest

one is a core-shell structure: hexagonal core and tetragonal shell. This last is supported by (i) HAADF-STEM images and (ii) stability of the hexagonal phase in the synthesis conditions [118]. The slightly brighter contrast in the HAADF-STEM images of the nanoparticles' core identifies this last as a higher density region, compatible with a CZTS hexagonal core surrounded by a lower density tetragonal shell. Although the opposite configuration (tetragonal core and hexagonal shell) cannot be completely ruled out, it is unlikely. In fact, in order to justify our results of the quantitative phase analysis by Rietveld refinement, hexagonal shell thickness should be 0.7 nm instead of 3 nm, which is the realistic value determined both by HRTEM and by HAADF-STEM observations.

4.5   Conclusions

High quality CZTS nanoparticles were produced in gram-scale, minimizing the amount of organic solvents and using cost effective, simple, and widely available starting materials as metal chlorides. The procedure is easily scalable and extendable for technological applications. The final product is made of equiaxial core-shell nanoparticles, having CZTS hexagonal core and CZTS tetragonal shell, with a monodisperse and narrow size distribution. Measured optical properties confirm the expected semiconducting behavior, a promising result for possible applications in the thin-film photovoltaic devices.

Part B: shows unpublished data

4.6 Composition control of CZTS nanoparticles
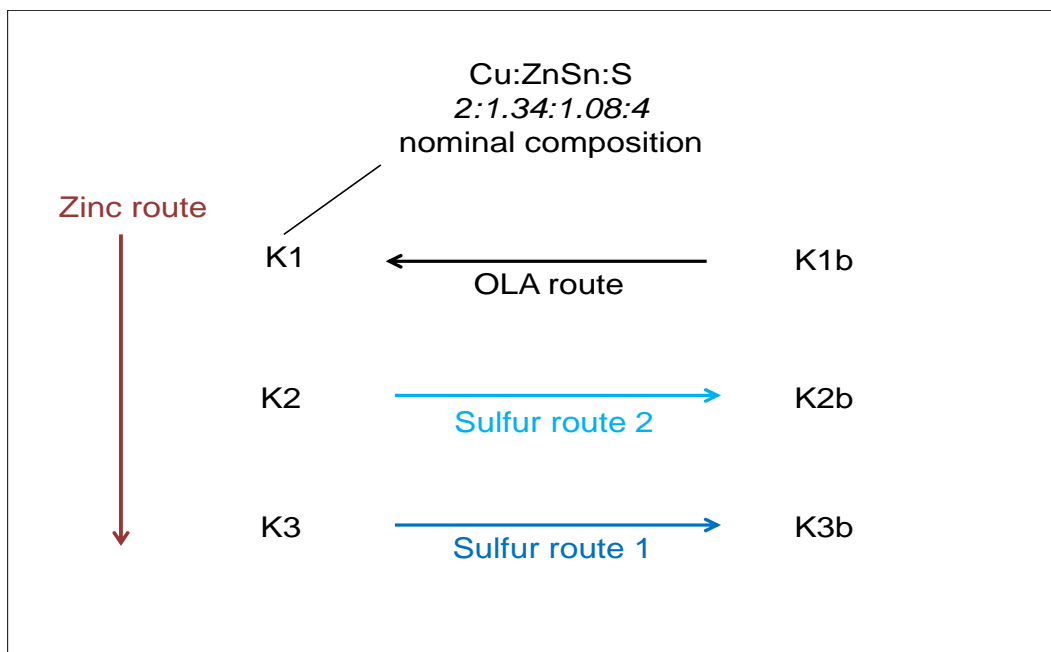
Figure 34. Scheme of the routes for the CZTS composition control.

4.7 Introduction

As mentioned previously, the use of the metal chlorides certainly lowers costs, but makes control of composition, size and final shape of CZTS nanoparticles more difficult. Stoichiometry is fundamental for the development of films with high efficiency. In order to achieve a control of the chemical composition, three different synthesis routes were carried out and samples having different amount of Zn, S and solvents were investigated. The following nominal composition was taken as a reference point for this study: Cu:Zn:Sn=2:1.34:1.08. To avoid Zn-poor compositions of CZTS, the conventional approach is to use an excess of the zinc precursor to compensate for its loss during the synthesis. So, the first step was to increase the starting zinc amount (mmol) with respect the desired nominal composition (Zinc route). Moreover, we studied the effect of the increase of sulfur in the synthesis of CZTS (S1 and S2 route). The third route (OLA route) consisted in varying the amount

of OLA used as solvent and capping agent. Once the desired stoichiometry was obtained, the sulfurization process and the thermal annealing have been examined (next chapter). All the experimental details are summarized in Table 4 and 5, described in the following experimental part.

4.8   Experimental details

The chemicals used for these activities were the same used in. The CZTS nanoparticles were synthesized by hot-injection method, as described above (4.2 Part A). The details of the starting elemental compositions are presented in Table 4. The inks were deposited on glass using the spin-coating method. X-ray florescence (XRF) spectroscopic studies were carried out to determine the elemental composition using a Thermo-Arl X'tra high-energy powder diffractometer.

Table 4. Details of the starting elemental composition of CZTS

Starting mmol values							
Route	Sample ID	Cu	Zn	Sn	S	S/(Cu+Zn+Sn)	OLA (mL)
Zn	**K1**	2	2.68	1.08	4	0.69	20
	K2	2	3.11	1.08	4	0.65	20
	K3	2	4.02	1.08	4	0.56	20
S1	**K3**	2	4.02	1.08	4	0.56	20
	K3b	2	4.02	1.08	6	0.85	20
S2	**K2**	2	3.11	1.08	4	0.65	20
	K2b	2	3.11	1.08	5.6	0.90	20
OLA	**K1**	2	2.68	1.08	4	0.69	20
	K1b	2	2.68	1.08	4	0.69	6.6

4.9   Results and discussion

The resulting compositions of the CZTS (Cu:Zn:Sn:S=2:1.34:1.08:4) films, as measured by XRF, are shown in the Table 5.

Table 5. Starting elemental composition and % of Zn loss for CZTS nanoparticles deposited on glass (determined using XRF).

Route	Sample ID	Cu	Zn	Sn	S	S/(Cu+Zn+Sn)	OLA (mL)	Zn XRF	Sn XRF	% Zn Zn(XRF)/Zn(start) *100	%Zn loss Zn(start.)/Zn(XRF) *100
Zn	K1	2	2.68	1.08	4	0.69	20	0.94	1.14	35	65
	K2	2	3.11	1.08	4	0.65	20	0.89	1.16	29	71
	K3	2	4.02	1.08	4	0.56	20	0.97	1.11	24	76
S1	K3	2	4.02	1.08	4	0.56	20	0.97	1.11	24	76
	K3b	2	4.02	1.08	6	0.85	20	3.28	1.18	81	19
S2	K2	2	3.11	1.08	4	0.65	20	0.89	1.16	29	71
	K2b	2	3.11	1.08	5.6	0.90	20	1.78	1.11	57	43
OLA	K1	2	2.68	1.08	4	0.69	20	0.94	1.14	35	65
	K1b	2	2.68	1.08	4	0.69	6.6	2.43	1.10	91	9

First of all, CZTS nanoparticles were synthesized, increasing the amount of zinc and keeping fixed the other parameters, here called sample K1, K2 and K3. Starting from the right of Table 5, the second column shows the zinc amount (mmoles) of each CZTS thin film, measured by XRF. Even increasing the amount of zinc chloride, the composition of the nanoparticles did not approach that desired. On the contrary, the quantity of zinc lost is more or less the same for all three compositions (Table 5). Samples K3 and K2 were also studied in order to evaluate the effect of varying sulfur amount during hot injection. In both S1 and S2 routes, the loss of zinc was reduced with respect the first approach. In particular the sample K2b shows a composition very close to the desired one. Moreover, the final composition of the CZTS nanoparticles of sample K1, prepared by lowering the amount of oleylamine (OLA route), was closest to the desired composition, showing a negligible zinc loss (Table 5 and Figure 35).
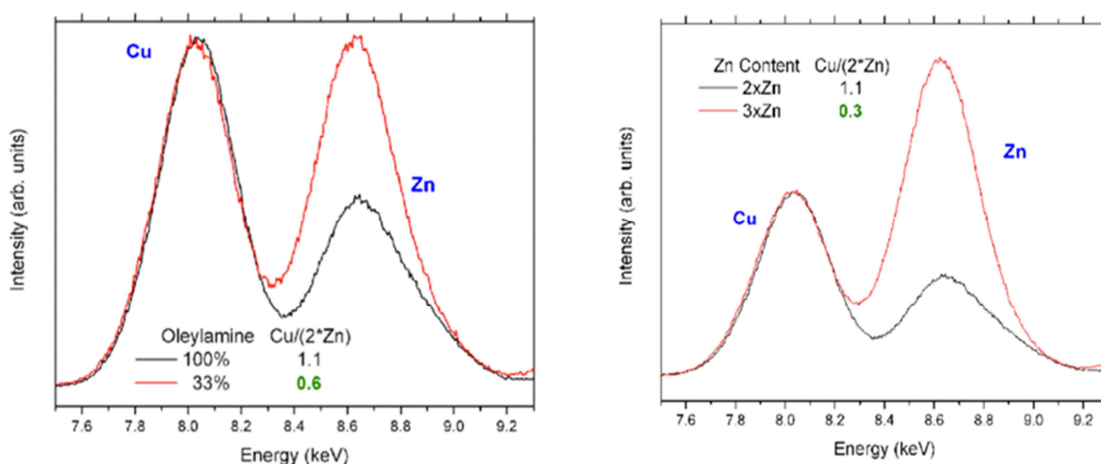
Figure 35. XRF results of the samples at different routes of starting changes.

This study has demonstrated that the first approach, based on the excess of zinc, does not lead to the desired elemental ratio. Zn-poor compositions were achieved also by increasing two or three times the amount of the starting zinc, with respect to the: after a certain amount, the zinc excess does not come into play in the formation of CZTS nano-crystals. Instead, a more effective control on the loss of zinc is reached by increasing the sulfur powder amount. It is possible to obtain a composition very close

to that of reference (Cu:Zn:Sn:S=2:1.34:1.08:4) by changing zinc and sulfur amounts together, as in sample K2b. However, the most important role in zinc loss is played by oleylamine: decreasing its amount increases the zinc content in the final composition of CZTS. In fact, OLA can act not only as solvent, but also as chelating/capping agent of the metallic ions. In this regard, OLA is effective in controlling the zinc availability during the CZTS formation reactions, hindering the zinc interaction with the CTS ternary compound (copper, tin and sulfur). In conclusion Figure 36 clearly shows a strategy for controlling the final composition, namely the loss of zinc varies in function of the initial sulfur/metal ion ratio.
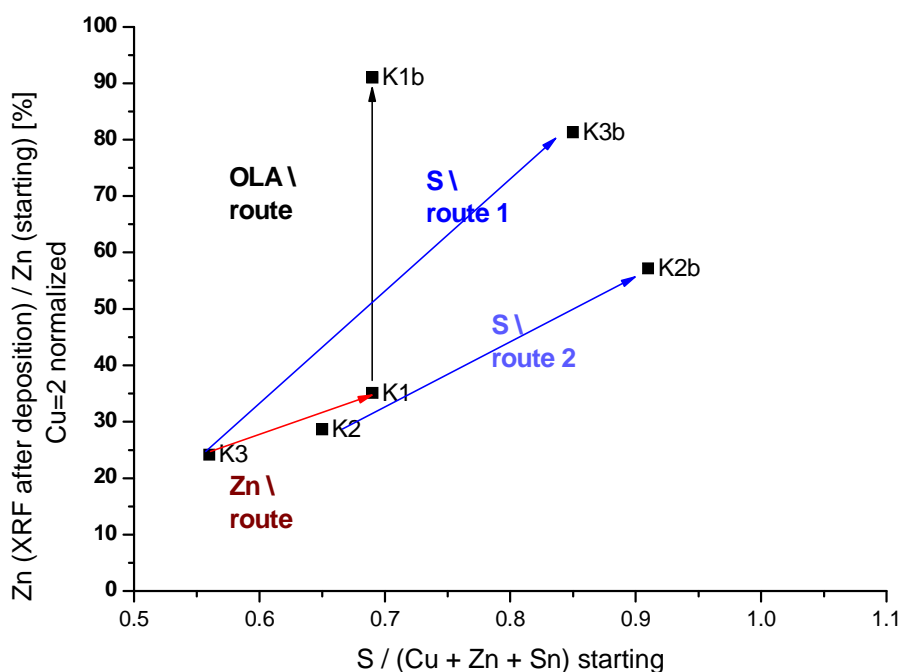
Figure 36. Plot of chemical composition ratios: starting Zn over measured Zn vs S/(Cu+Zn+Sn) starting ratio.

Chapter 5

Effect of the annealing time on CZTS thin films

In this chapter the effects of annealing conditions, time and gas atmosphere on the structure, morphology and photovoltaic properties of CZTS thin films has been described. Previous works on this subject suggest that heat treatment, under vacuum and/or a nitrogen atmosphere, facilitates grain growth and improves the electronic properties of the absorber layer. Furthermore, the sulfurization, e.g. annealing in sulfur, has been demonstrated to be advantageous, as it is non-toxic, compared to a treatment with selenium. CZTS nano-crystals with a specific Cu-poor/Zn-rich composition were synthesized through a hot injection method and the derived inks were annealed in a quartz tube furnace. Their grain growth, morphology and optical properties have been studied by a) varying the annealing time at 560 °C and b) carrying out a second annealing in sulfur vapor.

"Influence of annealing process on to morphological and optical properties of CZTS thin films".

R. D'Angelo[a], F. Girardi[a], C. L. Azanza Ricardo[a] , R. Di Maggio[a] and P. Scardi[a].

[a] *University of Trento, DICAM, Via Mesiano 77, 38121, Trento, Italy.*

5.1 Abstract

CZTS non-stoichiometric thin films [$Cu_2Zn_{1.34}Sn_{1.08}S_4$] have been successfully deposited on glass substrates by an effective and low cost simple spin-coating method for solar cells applications. Mono-disperse CZTS nanoparticles, produced in grams scale using hot-injection method, have been suspended in toluene forming an ink and used as starting material of thin films. These last underwent annealing treatments in order to form a continuous and effective layer of CZTS, suitable for measuring their optical properties. The present work shows how the different conditions of process correlate with the micro-structural and optical properties of the films. They underwent two consecutive annealing steps at 560 °C of different duration and with or without sulfur vapors during the second step. All these parameters affected not only roughness and porosity, but also stability of phases (SnS and ZnS were identified in some cases beside CZTS) and as a consequence a final optical properties. Actually, some studies claimed that spurious phases, such as SnS and ZnS, can limit the energy conversion efficiency of CZTS when used as absorber material in a thin photovoltaic device.

5.2 Introduction

Although thermal treatments and sulfurization are considered the best methods for growing CZTS absorbers films [36], [54] it is not common to find exhaustive studies correlating their properties with annealing and/or sulfurization process. In the previous chapter, it was described how synthesis can lead to a control of the chemical composition. Among all the prepared materials, for studying the effect of annealing we chose those having the composition closest to ideal CZTS (K2b). The present part describes how annealing time and sulfur vapor affect the structural and micro-structural features of the samples of CZTS, characterized by means of X-ray diffraction (XRD), FT-Micro-Raman spectroscopy, SEM micrographs and spectrophotometric measurements.

5.3 Experimental details

The synthesis of CZTS (having the following elemental ratio Cu:Zn:Sn=2:3.11:1.08) nanoparticles was carried out by hot injection processing as shown in the previous

chapter [3]. The particles were suspended in toluene forming ink, which was deposited on glass platelets by spin coating method. The residual toluene was removed in an oven at 150 °C for 5 min [3]. The films underwent two consecutive thermal treatments: TT1, under nitrogen atmosphere, and TT2 with sulfur vapor. The first was from room temperature up to 520 °C at 20 °C/min, then up to 560 °C at 10 °C/min with an isothermal step of variable length. The second thermal treatment differs from the first, because 20 mg sulfur powder was sprinkled around the sample in order to generate sulfur vapors under Ar atmosphere. The duration of each isothermal step is indicated in Table 6

Table 6. Summary of the samples and heat treatments used in this study.

		Isotherm at 560 °C	
Series	Sample	TT1 (min) without S	TT2(min) with S
I	I-0	20	-----
	I-120	20	120
	I-180	20	180
II	II-0	120	----
	II-20	120	20
	II-120	120	120
III	III-0	180	----
	III-20	180	20
	III-40	180	40
	III-60	180	60
	III-80	180	80
	III-180	180	180

Three sets of samples were studied, each of them, as shown in Table 6, underwent an isothermal step of increasing duration at 560 °C. Within each series, the time of the isothermal step was held constant at 560 °C of TT1, but increasing the isotherm of TT2 from 0 to 180 minutes.

5.4   Characterization of CZTS thin films

Raman spectra were collected on a LabRAM Aramis confocal microRaman system in backscattering configuration at 532 nm using a spectrometer with a grating of 1800 grooves/mm coupled to an air cooled 1024*256 VIS CCD. The X-ray diffraction (XRD) patterns were recorded on powder samples using theta-2theta incidence by a diffracted-beam graphite analyzer with a fixed $\Theta=0.25°$. Diffraction data were collected on a PANalytical X'Pert MRD diffractometer operated with a cobalt source (45kV, 30mA) and equipped with a polycapillary primary optics. A Jeol JMS 7401F Field-Emission SEM equipped with a Bruker EDX detector was employed for the compositional/morphological characterization. The optical properties were investigated by transmittance and reflectance measurements in the 250-2500 nm wavelength range, using a Perkin Elmer Lambda 750 spectrophotometer equipped with an integrating sphere.

5.5   Results (and discussion)

5.5.1   Micro-Raman Analysis

Raman spectrum (Figure 37) of the sample I-0 (Series I) shows a major peak at 329 cm^{-1} [92], [119, 120]. Other minor phases such as ZnS, SnS, Cu_2SnS_3 and $Cu_2SnS_{4)}$ are present. This indicated that a single short annealing is not sufficient to convert precursors into CZTS alone. The presence of copper sulfides (Cu_xS, $1<x<2$) is not clearly visible because, varying x, the main peak shifts from 260 to 270 cm^{-1}, where the signals of many phases can overlap. ZnS and SnS are the most important secondary phases, their presence suggests the low quality of the synthesis of nanoparticles, but their presence is difficult to confirm because the position of peaks is in a region crowded by peaks of other phases (e.g. ZnS could be hidden by Cu_2SnS_3 [54]) and the intensity of the peaks is very low, especially when the intensity of CZTS is high.
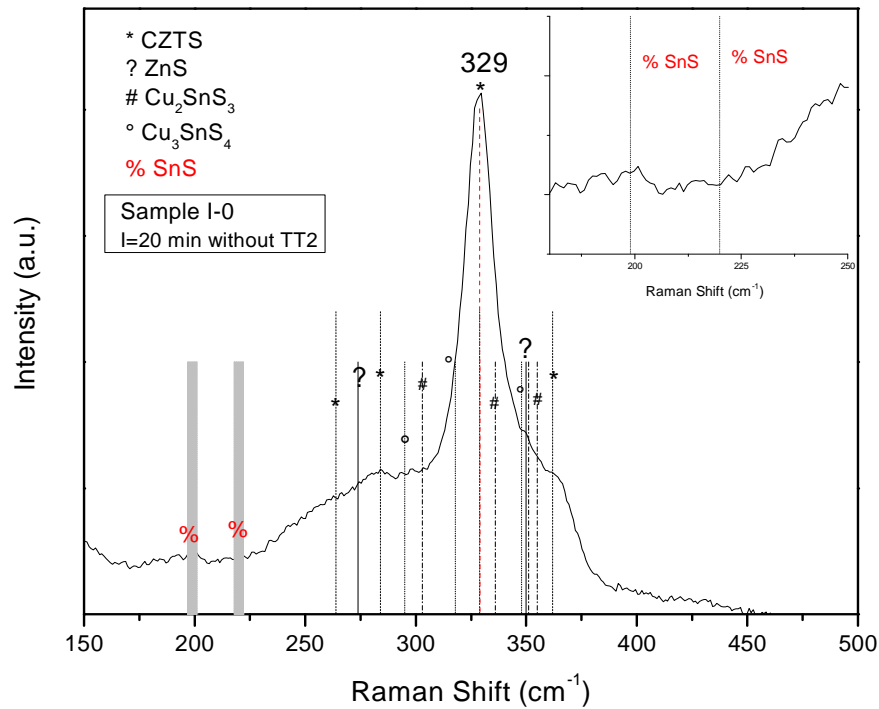
Figure 37. Micro-Raman spectra of a sample of series 1: I-0. The number indicates the main frequency of the main peak of its Raman spectrum.

5.5.2   *XRD Analysis*

In order to understand in detail the effect of the annealing time on the formation of one or more secondary phases, XRD spectra of the films were recorded (shown in Figure 38 (a), (b) and (c)). All XRD patterns exhibit peaks of kesterite (JCPDS 26-0575). The major peak, located at 33.2°, implies a preferential orientation in the (112) plane; in each XRD spectra all the diffraction peaks that belong to CZTS are highlighted. Within the Series I, the presence of the tin sulfide (SnS, ICDD card No 39-0354), which had been hypothesized on the basis of the results of Raman spectroscopy measurements, is confirmed. The peak at 37° (Figure 38 (a)) is characteristic of that phase and decreases with increasing the duration of the isotherm (TT2). Similarly in Series II (Figure 38 (b)) a second annealing with sulfur vapor favors the removal of this secondary phase (II-20), but longer treatments (II-120) again lead to SnS

formation. The XRD spectra of the series III show a higher content of SnS than in the previous ones. The peak at 37° disappears completely only in sample III-180. The other sulphide phase (ZnS) revealed by Raman cannot be directly identified, because its diffraction pattern is covered by that of CZTS, due to the similarity to zinc blend crystal [121].

In conclusion, the presence of pure single phase CZTS can be hypothesized only in samples I-180, II-20, III-180, which do not exhibit peaks attributable to secondary phases. The presence of these last phases in some annealed samples implies that the sulfurization was not effective in the given conditions of preparation.
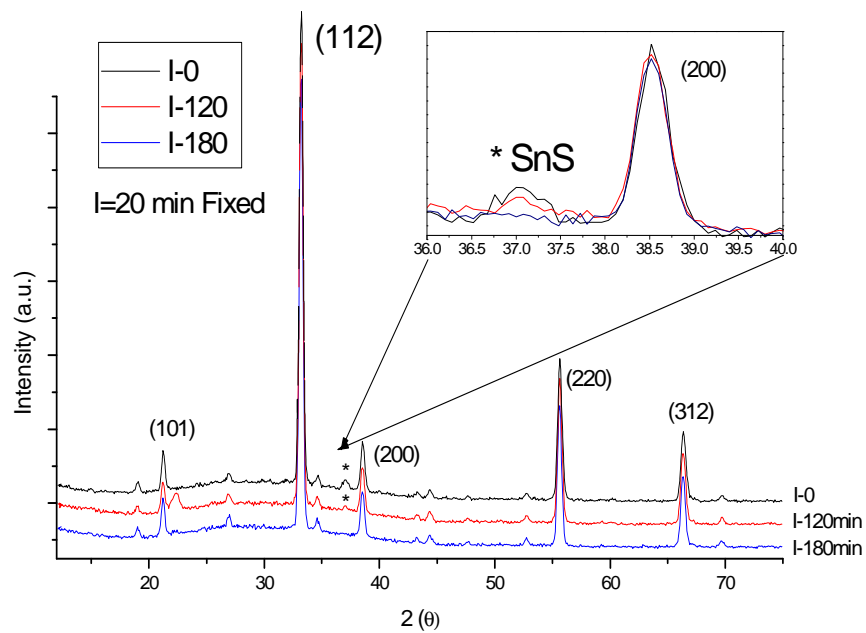
Figure 38 (a). XRD patterns of the thin films (Series I) annealed at different (TT2) times.
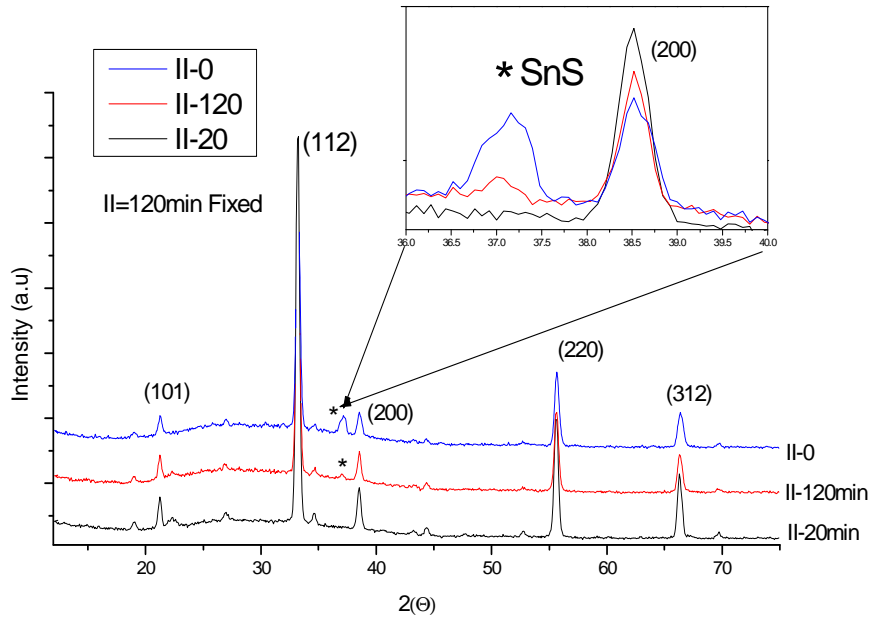
Figure 38 (b). XRD patterns of the thin films (Series II) annealed at different (TT2) times.
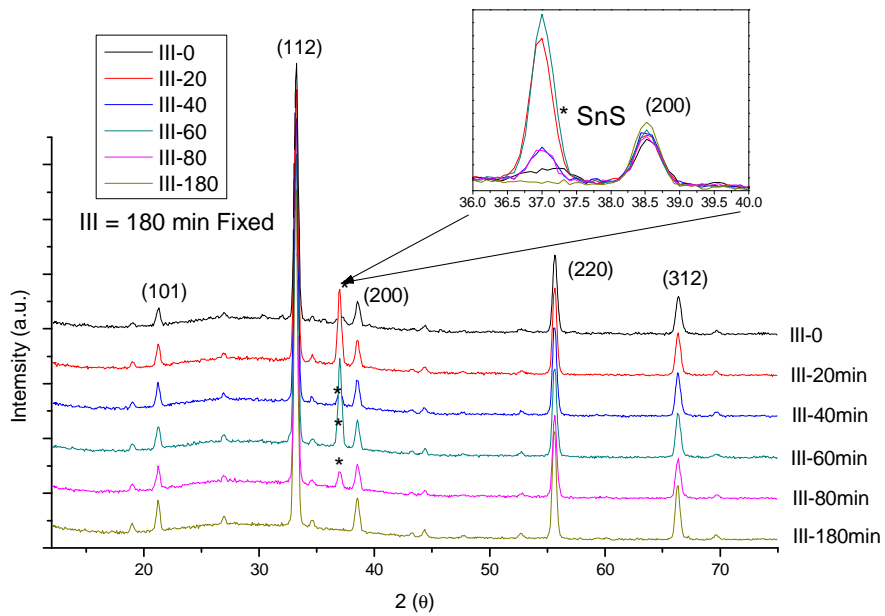
Figure 38 (c). XRD patterns of the thin films (Series III) annealed at different (TT2) times.

According to this extensive study, the first annealing in argon atmosphere seems to favor crystal growth but also the formation of phases such as tin sulfide: the longer the treatment the greater the amount of secondary phase (see Figure 39). Instead, the second treatment (sulfurization) does not entail an additional grain growth, but helps tin sulfide conversion into CZTS. As a consequence, the length of the second annealing has to be adapted to the amount of secondary phase formed after the first treatment
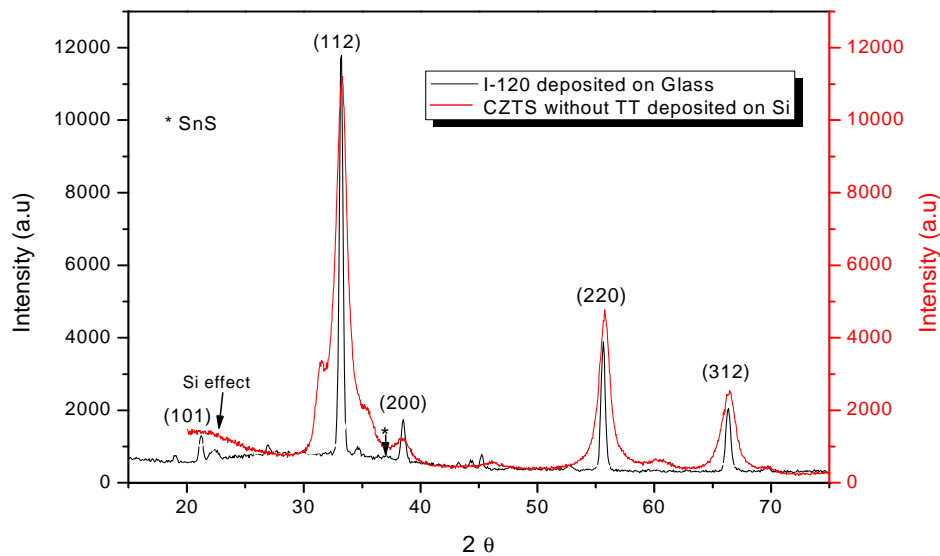
Figure 39. XRD patterns show the recrystallization of the thin films with and without TT. The red pattern (CZTS without TT) shows broad diffraction peaks, indicative of small crystalline domains. The black pattern (I-120) shows narrow or sharp diffraction peaks indicative of larger crystalline domains, suggesting that the TT leads grain growth.

5.5.3   *Compositional and Morphological study*

In order to evaluate the morphology of the layer after annealing, the cross-section of the samples was observed through SEM. Figure 40 shows some SEM micrographs taken on samples with a variable content of secondary phase (I-120, II-20, II-120). All the films have a similar thickness of about 1.5 μm. The samples, characterized by the presence of tin sulfide in the XRD patterns (I-120 and II-120), show a similar morphology: some distorted grains and voids/pores at the coating/glass interface, especially in the sample I-120 (at top left). It has not yet been fully understood

whether the voids develop during the film growth or during the annealing. Comparing the two samples from the series II, we see that the increase of the time of sulfurization leads to a low compact film. This is in contrast with that found in literature [122]. Instead II-20 sample appears more densely packed, although it seems detached from substrate, probably owing to the cutting step in the preparation of the cross-section. The higher apparent density of the CZTS nanoparticles in this sample could be correlated to the lower amount, or even the complete absence, of secondary phases, see XRD pattern (Figure 38 (b)).
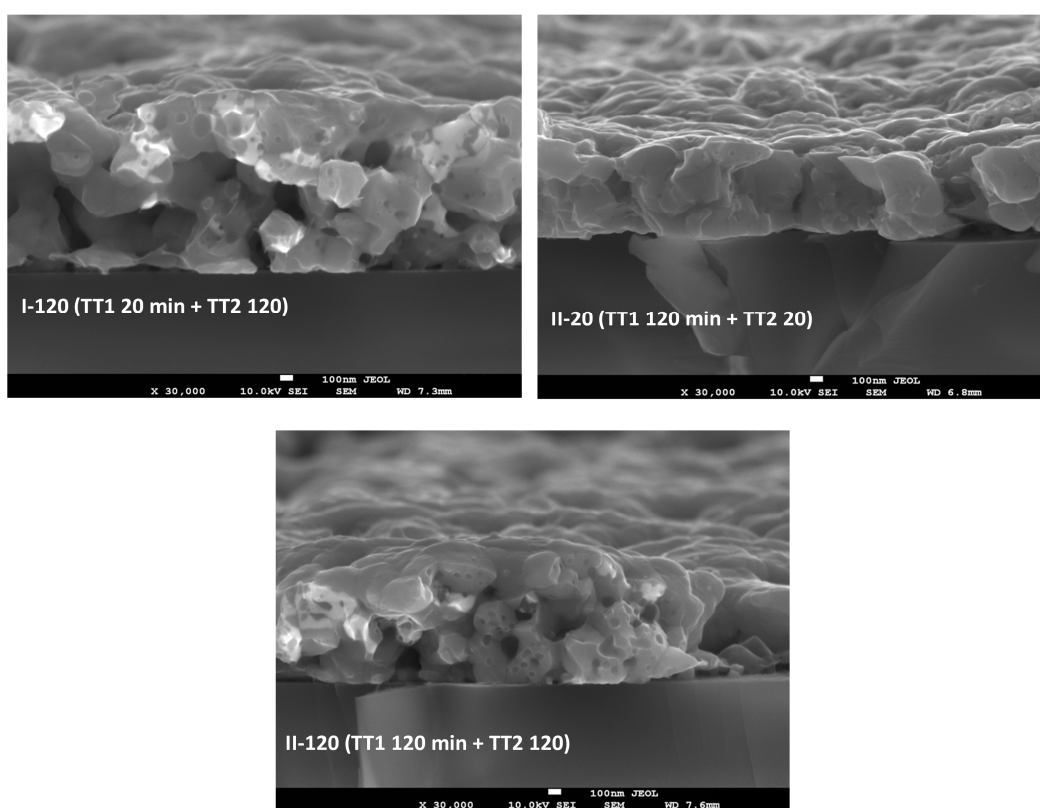
Figure 40. SEM micrographs of the cross-sections of some films. Operating conditions for the imaging (voltage and working distance WD) are reported in the micrographs, along with the labels and the times of annealing of the samples.

The elemental composition ratios of annealed films were determined by XRF and listed in Table 7. The first row shows the ideal ratios between the cations corresponding to the formula Cu:Zn:Sn:S = 2:1.34:1.08:4. All the samples are Zn-rich (Zn/Sn > 1) and slightly Cu-poor, with sample II-120 having Cu/(Zn + Sn)>1.

It was found that the higher Cu/(Zn+Sn) ratio the more porous the film [123].This is also confirmed by our analysis of the samples I-120, II-20 and II-120 (Figure 40). Accordingly, sample II-20 shows the best morphology in SEM micrograph, e.g. a compact layer without voids, and an elemental composition closest to that of nominal.

Table 7. Annealing conditions (all in flowing Ar background gas) and bulk compositions measured by XRF on the samples under discussion in this chapter.

Series	Sample name	Cu/Zn	Cu/Sn	Zn/Sn	Cu/(Zn+Sn)
		0.75	**0.93**	**1.24**	**0.83**
CZTS thin film	Without annealing	0.56	1.00	1.79	0.72
I	I-0	0.61	1.12	1.86	0.79
	I-120	0.78	1.29	1.58	0.97
	I-180	0.83	1.36	1.64	1.03
II	II-0	0.55	1.17	2.12	0.75
	II-20	0.77	1.01	1.31	0.87
	II-120	0.86	3.16	3.69	1.35
III	III-0	0.57	1.22	2.15	0.77
	III-20	0.64	1.58	2.48	0.91
	III-40	0.60	1.33	2.20	0.83
	III-60	0.63	1.38	2.19	0.86
	III-80	0.61	1.31	2.16	0.83
	III-180	0.76	0.85	1.11	0.80

5.5.4 Optical Properties

The optical properties of all the samples were analyzed by spectrophotometric measurements in the 250-2500 nm wavelength range. The method for calculating the energy gap through a Tauc-plot was described in chapter 4 (section 4.3 Results, pages 56) [124]. The band gap values were calculated using the following equation:

$$\alpha h\upsilon = A(h\upsilon - E_g)^{n/2}$$

where α is the absorption coefficient related to the incident photon energy, h is Planck's constant, υ is the frequency, E_g is the band gap, A is a proportionality constant and n conveys the nature of the radiative transition: in our case it is equal to 1 for direct band gap material. For all films, the value used for the absorption coefficient in the visible range was $>10^4 \, cm^{-1}$.

The values of band gap (Eg) of CZTS thin films were estimated from the absorption spectra and listed in Table 8. In the Table are also indicated the eventual presence of tin sulfide, the heat treatments employed for each sample and the thickness. The Figure 41 (a), (b) and (c), represent the Tauc plots of the annealed samples: the band-gap is obtained from the extrapolation of the linear part of the plot $(\alpha h\upsilon)^2$ vs. $h\upsilon$ at $(\alpha h\upsilon)^2$ equals zero.

Table 8. Values of E04 (energy at which $\alpha = 10^4 cm^{-1}$), SnS presence, and maximum transmittance measurement for all CZTS film Series.

Series	Sample name	TT1 (min) without S	TT2 (min) with S	SnS	T% (max)	Thickness (d, μm)	E04 (eV)
	I-0	20	-----	Found	45.38	1.55	1.507
I	I-120	20	120	Found	54.01	1.60	1.540
	I-180	20	180	Not F.	46.30	1.00	1.380
II	II-0	120	----	Found	65.70	1.00	1.480
	II-20	120	20	Not F.	47.60	1.67	1.445
	II-120	120	120	Found	42.04	1.10	1.459

Series	Sample name	TT1 (min) without S	TT2 (min) with S	SnS	T% (max)	Thickness (d, μm)	E04 (eV)
III	III-0	180	----	Found	35.78	1.00	1.404
	III-20	180	20	Found	54.87	1.26	1.530
	III-40	180	40	Found	54.30	1.28	1.471
	III-60	180	60	Found	52.75	1.22	1.464
	III-80	180	80	Found	47.40	1.22	1.402
	III-180	180	180	Not F.	27.58	1.17	1.372

Figure 41 shows the Tauc plots for all the CZTS thin film annealed with different conditions. Comparing the band gap values with the corresponding Tauc plots, it can be seen that the lowest gap values (I-180, II-20, II-120, III-0, III-40, III-60, III-80, III-180) correspond to the highest optical absorptions at energies lower than the gap itself, in a region in which the samples should be transparent. This anomalous absorption is due to the poor quality of material; in particular the exponential and irregular tail of the absorption curve (Figure 41 (c)) is associated with a high conductivity, which depends on high defects concentration and/or the presence of secondary phases. Taking into account this, the analysis of Tauc plots suggests short annealing processes, e.g. within the series I the longer the sulfurization time (from 0 to 180 min) the shorter the band gap (from 1.530 to 1.372 eV), rather than a higher optical absorption below the gap. The increase of isothermal segment in the first annealing (I-0, II-0, III-0) seems to affect less the optical absorption behaviour and the relative shift of Tauc plot (Figure 42). The worst samples were those of series III, but III-180, which may be partly explained by the presence of SnS shown by the analyses of XRD spectra. In the case of III-180 the trend of Tauc plot (and the lowest value of band gap) may be due to a high concentration of defects or to spurious phases, such as the Cu_2SnS_3 that was identified in the sample I-0 by Raman spectroscopy, not visible in the XRD spectra.
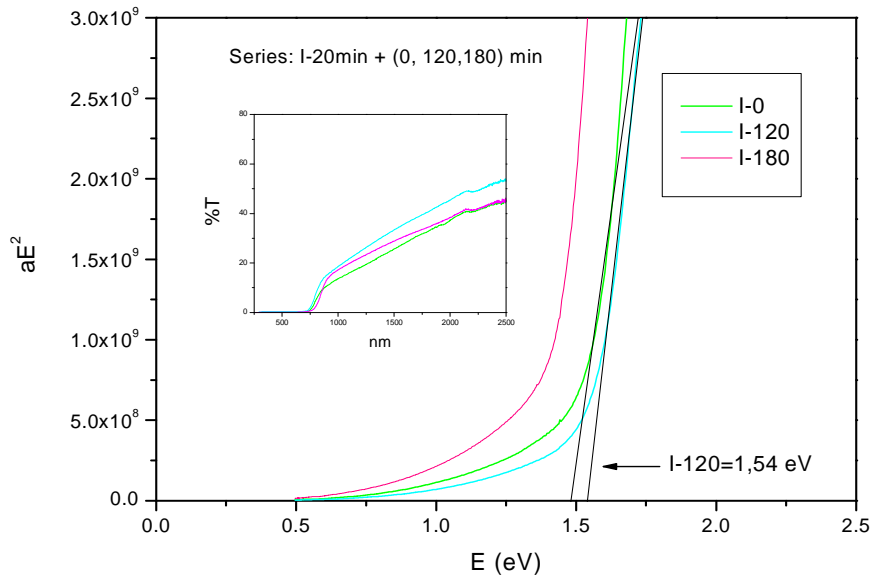
Figure 41 (a) Evolution of the CZTS Series I. Band gap for fixed (20 min) TT1 and different TT2 time.
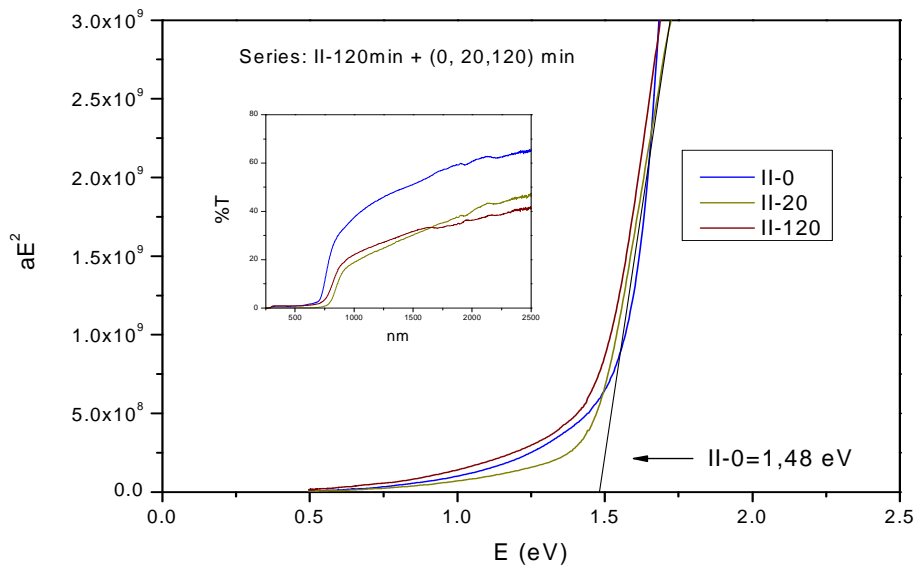
Figure 41 (b) Evolution of the CZTS Series II. Band gap for fixed (20 min) TT1 and different TT2 time.
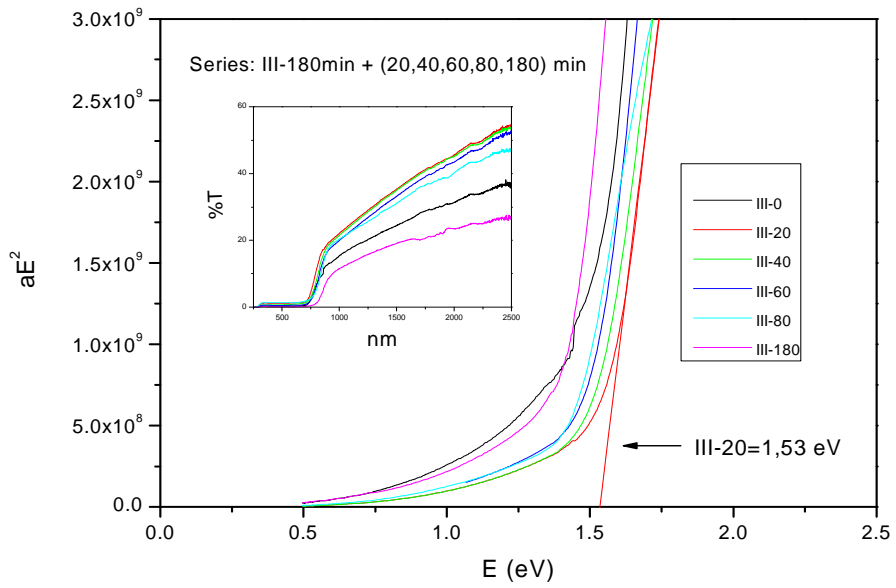
Figure 41 (c) Evolution of the CZTS Series III. Band gap for fixed (20 min) TT1 and different TT2 time.
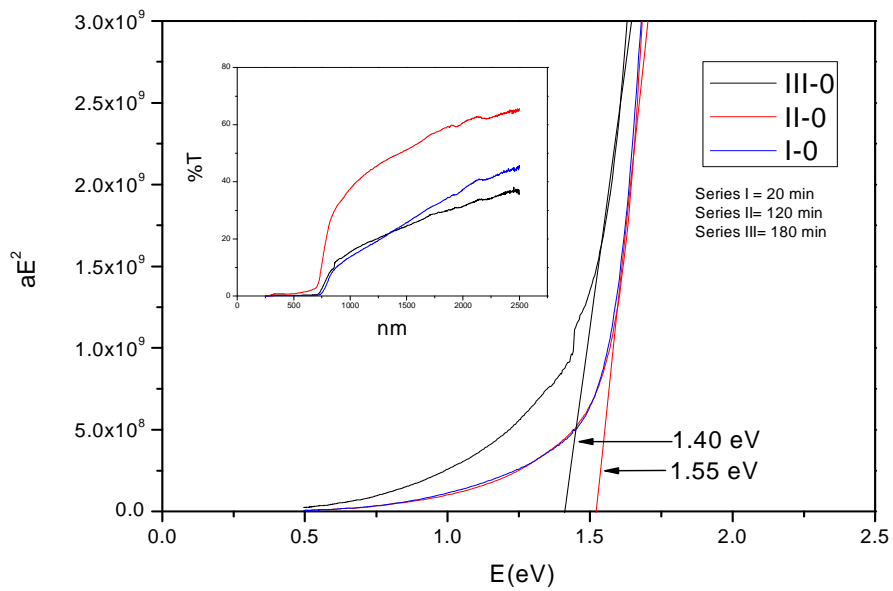
Figure 42. Evaluation Band gap (eV) of CZTS Series I, II, III without TT2

Previous works explained the Eg variation with the presence of secondary phases and in particular Sn-rich spurious phases. SnS (Eg of 1.3 eV [85]) would give rise to a Eg decrease, however, in these samples there is not a direct correlation between the presence of SnS (XRD spectra) and the value of band gap.

5.6   Conclusions

The first annealing process (without vapor of S) causes a grain growth, but the analyses by Raman spectroscopy and X-ray Diffraction identified also the presence of spurious phases, such as SnS, the only secondary phase easily identifiable in XRD spectra. Sulfurization reduces the amount of tin sulfide. Increasing the duration of the first annealing also increases SnS. This secondary phase can contribute to CZTS formation during the second annealing of proper duration. A very long isothermal step for both the first and the second treatment (e.g. I-180) leads to the disappearance of SnS phase, but also to both the formation of defects and/or other spurious phases, which cause a lowering of the band gap.

Chapter 6

Conclusion and future outlook

The present research project was focused on synthesis and characterization of non-stoichiometric Cu_2ZnSnS_4 (CZTS) absorber layers obtained by non-vacuum growth processes. The main goals of this work were a) to avoid the use of toxic, expensive, rare or explosive reagents; b) the use of reproducible and scalable procedures.

Two different processes were investigated: the first approach, described in Chapter III, was based on the synthesis of CZTS layers starting from metal salts–thiourea precursor solutions i); the second one, reported in Chapter IV-V, was focused on the hot injection method that consists in the injection of a sulfur source into a hot solution of metal precursors and surfactant ii).

In the first part of the thesis, several metal–thiourea complexes were prepared changing the organic solvents used to prepare the starting solutions of metal salts and thiourea. In general, the mixing of these two solutions leads the formation of complex sulfides: a comprehensive characterization (by X-ray diffraction, EDXS analysis and Raman spectroscopy measurements) led to conclusion that the synthesis in methanol/ethylene glycol gives pure kesterite without spurious phases. This study has demonstrated that Zn-rich/Cu-poor CZTS layers can be obtained without vacuum or sulfurization steps. Additional investigations were performed to understand the reactions sequence leading to the formation of CZTS, and a feasible reaction mechanism, that involves the coordination of the metal ions by thiourea and the intermediate formation of thiols, was proposed.

In conclusion, with a careful control of the reaction conditions, it is possible to develop a green route for the production of CZTS absorber layers.

The second and parallel activity was based on the synthesis of high-quality CZTS nano-crystals via the thermolysis of low-cost precursors: monodisperse nano-crystals were obtained by the thermal decomposition of metal chlorides into a hot organic surfactant (oleylamine) with a dissolved sulfur source. The extensive investigation, presented in chapter IV determined that the final product is made of equiaxial core-shell nanoparticles, having a hexagonal core and a tetragonal shell, with a narrow size distribution. The main objectives have been reached, indeed the developed procedure is cheaply, easily scalable and extendable to technological applications.

Part of chapter IV was also devoted to the compositional control of the CZTS nanoparticles. The main problem of this growth process is the loss of zinc due to the different stability of the zinc complex with respect to those of copper and tin: while the formation of the complexes and of the quaternary chalcogenide takes place, a large amount of zinc cations is not active leading to the production of a material poor in this element. This work has demonstrated that the chemical composition of the obtained CZTS nano-crystals can be tuned by changing some reaction conditions, in particular the amount of sulfur source and surfactant used. Therefore, the balancing of the metal precursors, the sulfur source and the surfactant could be the key for the production of quaternary chalcogenides with highly predictable composition.

In the typical process, the resulting powders are dispersed in toluene to form inks that are later deposited by spin coating technique; the obtained films are subjected to thermal treatments at high temperature. In Chapter V, two different types of treatments were studied in order to study the effect of the post-deposition annealing on the morphology and the optical properties of CZTS films. The investigation performed on annealed CZTS thin films has shown that: a) annealing without sulfur powder gives grain growth, but also the formation of secondary phases such as tin sulfide; b) SnS is converted back to CZTS during the sulfurization process; c) long isothermal segments, longer than 120 minutes, seem to favor the formation of defects, or of other spurious phases in the CZTS. This involves a lowering of the band gap, i.e. the best Tauc-Plot was obtained after a first isotherm of 20 min followed by a second one of 120 min.

Additional investigations are necessary to clarify completely the effect of the heat treatment conditions on the absorber thin layer.

This study showed that the spin-coating method could have some limitations even if it is often preferred in the laboratory practice for reproducibility and cost effectiveness. In particular, the SEM investigation highlighted a non-homogeneous distribution on the surface, which might partly be ascribed to this deposition method. The macroscopic defects, such as cracks due to the spin-coating, together with the secondary phases could become factors limiting the use of CZTS inks in the overall deposition of PV devices. Moreover the spin-coating is neither high-throughput nor scalable, and has the fatal drawback of wasting a good deal of material.

For these reasons the future step will be to test alternative deposition methods, e.g. spray coating and ink-jet printing that are able to perform large-area depositions and a direct scaling-up to industrial production.

References

[1] D. Alain, C. Pierre. Introduction to Sol-Gel Processing. Kluwer academic publisher. Second edition, 1-2 and 91, (2002).

[2] R. D'Angelo, C. L. Azanza Ricardo, A. Mittiga, P. Scardi, M. Leoni. A water- and sulphurization- free solution route to $Cu_{2-x}Zn_{1+x}SnS_4$. J. Sol-Gel Sci. Technol. 72, 490-495, (2014).

[3] C. L. Azanza Ricardo, F. Girardi, E. Cappelletto, R. D'Angelo. R.Ciancio, E. Carlino, P. C. Ricci,C. Malerba, A. Mittiga, R. Di Maggio and P. Scardi. Chloride-based route for monodisperse CZTS nanoparticles preparation. J. Renewable Sustainable Energy, 7, ID 043150, (2015).

[4] C. Hao, Y. Qinyan, H. Xulin, D. Jingjing, Z. Yongzheng, H. Junfeng, L. Jiang. L. Cheng, Jun Meia and L. Woonming. Electrodeposited CZTS solar cells from Reline electrolyte. Green Chem. 16, 3841-3845, (2014).

[5] Y. B. Kishore Kumar, P. Uday Bhaskar, G. Suresh Babu and V. Sundara Raja. Effect of copper salt and thiourea concentrations on the formation of Cu_2ZnSnS_4 thin films by spray pyrolysis. physica status solidi (a), 207, 1, 149–156, (2010).

[6] G. Korotcenkov. Handbook of Gas Sensor Materials: Properties, Advantages and shortcoming for applications (2), new trends and technologies. Integreted analytical systems, (2), 396, (2014).

[7] R. W. Schwartz and M. Narayanan, Solution Processing of Chalcogenide Semiconductors via Dimensional Reduction, chapter 2, 33–76, John Wiley & Sons, Inc. (2008).

[8] Feynman, Richard. Feynman Lectures on Physics. Basic Books, (1963).

[9] A. Walsh, S. Chen, S. H. Wei, and X. G. Gong. Kesterite. Thin-Film Solar Cells: Advances in Materials Modelling of Cu_2ZnSnS_4. Adv. Energy Mater. 2, 400–409, (2012).

[10] S. Schorr, H.-J. Hoebler, M. Tovar. A neutron diffraction study of the stannite-kesterite solid solution series. Eur. J. Mineral. 19, 65, (2007).

[11] W. Shockley and H. Queisser. Detailed Balance Limit of Efficiency of p-n Junction Solar Cells. J. Appl. Phys. 1640, 510–519, (1961).

[12] K. Mitchell, A. L. Fahrenbruch, R. H. Bube. Structure and electrical properties of CdS and CdTe thick films for solar cell applications. J. Vacuum Sci. Technol. 12, (4), 909-911, (1975).

[**13**] D. Cusano. CdTe solar cells and photovoltaic heterojunctions in II–VI compounds. Solid-State Electronics, 6, (3), 217-218, (1963).

[**14**] A. Shah, R. Platz, H. Keppner. Thin-film silicon solar cells: A review and selected trends. Sol. Energy Mater. Sol. Cells. 38, (1-4), 501–520, (1995).

[**15**] A. Shah, P. Torres, R. Tscharner, N. Wyrsch, H. Keppner. Photovoltaic technology: the case for thin-film solar cells. Science, 285, (5428), 692-8, (1999).

[16] G. Zoppi, I. Forbes, R. W. Miles, P. J. Dale, J. J. Scragg and L. M. Peter. $Cu_2ZnSnSe_4$ thin film solar cells produced by selenisation of magnetron sputtered precursors. Prog. Photovoltaics, 17, 315–319, (2009).

[17] K. Ito and T. Nakazawa. Electrical and optical properties of stannite-type quaternary semiconductor thin films. J. Appl. Phys. 27, 2094–2097, (1988).

[18] C. Lee and C. Kim. Optical properties of undoped and Co^{2+} - doped $Cu_2ZnGeSe_4$ crystalas. J. Am. Chem. Soc. 37, (3), 364–367, (2000).

[19] S. Chen, X. Gong, A. Walsh and S.-H. Wei. Electronic structure and stability of quaternary chalcogenide semiconductors derived from cation cross-substitution of II-VI and I-III-VI 2 compounds. Phys. Rev. B, 79, 1–10, (2009).

[20] H. Zhou, W.-C. Hsu, H.-S. Duan, B. Bob, W. Yang, T.-B. Song, C.-J. Hsu and Y. Yang. CZTS nanocrystals: a promising approach for next generation thin film photovoltaics. Energy Environ. Sci. 6, 2822–2838, (2013).

[21] C. Wadia. A. P. Alivisatos. and D. Kammen. M. Materials Availability Expands the Opportunity for Large-Scale Photovoltaics Deployment. Environmental Science & Technology, 43, (6), 2072–7, (2009).

[22] R. Nitsche, D.F. Sargent, P. Wild, Crystal growth of quaternary I(2)II-IV-VI(4) chalcogenides by iodine vapour transport. Journal of Crystal Growth, 1, (1966).

[23] K. Ito and T. Nakazawa. Electrical and Optical Properties of Stannite-Type Quaternary Semiconductor Thin Films. Japanese Journal of Applied Physics, 27, 1, 11, (1988).

[24] K. Hironori, J. Kazuo, Maw, W, Shwe, O. Koichiro, Y. Makoto, A. Hideaki, T. Akiko. Development of CZTS-based thin film solar cells. Thin Solid Films, 517, (7), 2455–2460, (2009).

[25] J. Ge, J. Chu, J. Jiang, Y. Yan and P. Yang. Characteristics of In-substituted CZTS thin film and bifacial solar cell. ACS Applied Materials & Interfaces, 6, (23), 21118–21130, (2014).

[26] T. K. Todorov, K. Tang, S. Bag, O. Gunawan, T. Gokmen, Y. Zhu, D.B. Mitzi. Beyond 11 % efficiency: characteristics of state of- the-art $Cu_2ZnSn(S, Se)_4$ solar cells. Adv. Mater. 3:34–38, (2012).

[27] W. Wang, M.T. Winkler, O. Gunawan, T. Gokmen, T. K. Todorov, Y. Zhu, D. B. Mitzi. Device Characteristics of CZTSSe Thin-Film Solar Cells with 12.6% Efficiency. Advanced Energy Materials. 4, 7, (2014).

[28] Y.E. Romanyuk, C.M. Fella, A.R. Uhl, M. Werner, A.N. Tiwari,T. Schnabel, E. Ahlswede. Recent trends in direct solution coating of kesterite absorber layers in solar cells. Solar Energy Materials & Solar Cells, 119, 181–189, (2013).

[29] Q. Guo, H. Hillhouse and R. Agrawal. Synthesis of Cu_2ZnSnS_4 Nanocrystal Ink and Its Use for Solar Cells. J. Am. Chem. Soc., 131 (33), 11672–11673, (2009).

[30] F. London. The general theory of molecular forces. Transactions of the Faraday Society 33: 8–26, (1937).

[31] W. H. Keesom. The second viral coefficient for rigid spherical molecules, whose mutual attraction is equivalent to that of a quadruplet placed at their centre. KNAW, 18 I, 636-646, (1915).

[32] S. E. Habas, H. A. S. Platt, M. F. A. M. van Hest, and D. S. Ginley. Low-Cost Inorganic Solar Cells: From Ink To Printed Device. Chem. Rev., 110 (11), 6571–6594, (2010).

[33] V. S. Aradhya, M. Frei, M. S. Hybertsen and L. Venkataraman. Van der Waals interactions at metal/organic interfaces at the single-molecule level. Nature Materials, Letters, (2012).

[34] M. Seipenbusch, S. Rothenbacher, A. P. Weber, G. Kasper. Interparticle forces in Nanoparticle Agglomerates. Title, European Aerosol Conference, Salzburg, (2007).

[35] B. Bhushan, D. Luo, S. R. Schricker, W. Sigmund, S. Zauscher. Handbook of Nanomaterials Properties. Springer Science & Business Media, 462, (2014).

[36] S. Magdassi. In The Chemistry of Inkjet Inks. World Scientific Publishing Co. Pte. Ltd.: Hackensack, NJ, (2010).

[37] H. W. Hillhouse. Energy Research Area: Developing nanocrystal-ink and molecular-ink based solar cells, nanowire-based devices, and novel fuel cells. Retrieved from https://www.washington.edu/research/energy/researcher/hugh-w-hillhouse. University of Washington, (2012).

[38] P. C. Duineveld, The stability of injek-jet printed lines of liquid ith zero receding contact angle on a homogeneous substrate. J. Fluid Mech. 477, 175-200, (2003).

[39] P. J. Smith, D. Y. Shin, J. E. Stringer, B. Derby, N. Reis. Direct ink-jet printing and low temperature conversion of conductive silver patterns. Journal of materials science 41, (13), 4153-4158, (2006).

[40] M. Guglielmi. Glass: Sol–Gel Coatings. Encyclopedia of Materials: Science and Technology, 3575–3579, (2001).

[41] M. Guglielmi, P. Colombo, F. Peron. Dependence of thickness on the withdrawal speed for SiO_2 and TiO_2 coatings obtained by the dipping method. Journal Of Materials Science, 27, 5052-5056, (1992).

[42] M. Guglielmi and S. Zenezini. The thickness of sol-gel silica coating obtained by dipping. J. Non-Cryst. Solids, 303-309, (1990).

[43] J. Livage, F. Beteille, C. Roux, M. Chatry, P. Davidson. Sol–gel synthesis of oxide materials. Acta Materialia, 46, (3), 23, 743–750, (1998).

[44] R. Caballero J. M. Cano-Torres E .Garcia-Llamas, X. Fontané, A. Pérez-Rodríguez, D. Greiner, C. A. Kaufmann, J. M. Merino, I. Victorov, G. Baraldi, M. Valakh, I. Bodnar,

V. Izquierdo-Roca, M. León. Towards the growth of $Cu_2ZnSn_{1-x}GexS_4$ thin films by a single-stage process: Effect of substrate temperature and composition. Solar Energy Materials & Solar Cells, 139, 1–9, (2015).

[45] H. Araki, A. Mikaduki, Y. Kubo, T. Sato, K. Jimbo, W. S. Maw, H. Katagiri, M. Yamazaki, K. Oishi, A. Takeuchi. Preparation of Cu_2ZnSnS_4 thin films by sulphurization of stacked metallic layers. Thin Solid Films, 517, 1457–1460, (2008).

[46] J. Muller, J. Nowoczin, H. Schmitt, Composition, structure and optical properties of sputtered thin films of $CuInSe_2$. Thin Solid Films, 496, (2), 364-370, (2006).

[47] X.T. Hao, J. Ma, D.H. Zhang, et al., Thickness dependence of structural, optical and electrical properties of ZnO: Al films prepared on flexible substrates, Applied Surface Science, 183, 137–142, (2001).

[48] A. Emrani, P. Vasekar, C. R. Westgate. Effects of sulphurization temperature on CZTS thin film solar cell performances. Solar Energy, 98, 335–340, (2013).

[49] H. Katagiri, K. Jimbo, W.S. Maw, K. Oishi, M. Yamazaki, H. Araki, A. Takeuchi.. Development of CZTS-based thin film solar cells. Thin Solid Films 517, 2455–2460, (2009).

[50] S. Delbos. Kesterite thin films for photovoltaics: a review. EPJ Photovoltaics 3, 35004, (2012).

[51] J. Ge, Y. Wu, C. Zhang, S. Zuo, J. Jiang, J. Ma, P. Yang and J. Chu. Comparative study of the influence of two distinct sulphurization ramping rates on the properties of Cu_2ZnSnS_4 thin films Appl. Surf. Sci., 258, (19), 7250-7254, (2012).

[52] A. J. Cheng, M. Manno, A. Khare, C. Leighton, S. Campbell, E. Aydil, J. Vac. Sci. Technol. A Vac. Surf. Films, 29, 051203, (2011).

[53] O. Volobujeva, J. Raudoja, E. Mellikov, M. Grossberg, S. Bereznev, R. Traksmaa. $Cu_2ZnSnSe_4$ films by selenization of Sn-Zn-Cu sequential films. J. Phys. Chem. Solids, 70, 567-570, (2009).

[54] R. Schurr, A. Hölzing, et al. The crystallisation of Cu_2ZnSnS_4 thin film solar cell absorbers from co-electroplated Cu–Zn–Sn precursors. In: Thin Solid Films, 517, 2465–2468, (2009).

[55] M. Ganchev, J. Iljina, L. Kaupmees, T. Raadik, O. Volobujeva, A. Mere, M. Altosaar, J. Raudoja and E. Mellikov. Phase composition of selenized $Cu_2ZnSnSe_4$ thin films determined by X-ray and Raman spectroscopy. Thin Solid Films, 519, (21), 7394-7398, (2011).

[56] K. Maeda, K. Tanaka, Y. Nakano and H. Uchiki, Annealing temperature dependence of properties of Cu_2ZnSnS_4 thin films prepared by sol-gel sulphurization method. Jpn J. Appl. Phys. 50, (5), ID. 05FB08, (2011).

[57] A. Redinger and S. Siebentritt. Coevaporation of Cu_2ZnSe_4Thin films. Appl. Phys. Lett. 97, ID. 092111, (2010).

[58] S. Ahmed, K.B. Reuter, O. Gunawan, L. Guo, L.T. Romankiw and H. Deligianni. A High Efficiency Electrodeposited Cu_2ZnSnS_4 Solar Cell. Adv. Energy Mater. 20, 1-7, (2011).

[59] H. Yoo and J. Kim. Growth of $CuZnSnS_4$ thin films using sulphurization of stacked metalie films. Thin Solid Films, 518, (22), 6567-6572, (2010).

[60] I. Repins, C. Beall, N. Vora, C. DeHart, D. Kuciauskas, P. Dippo, B. To, J. Mann, W.-C. Hsu, A. Goodrich and R. Noufi. Co-evaporated $Cu_2ZnSnSe_4$ films and devices. Solar Energy Materials and Solar Cells, 101, 154-159, (2012).

[61] A. Khalkar, K.-S. Lim, S.-M. Yu, D.-W. Shin, T.-S. Oh, and J.-B. Yoo. Effects of Sulfurization Pressure on the Conversion Efficiency of Cosputtered Cu_2ZnSnS_4 Thin Film Solar Cells. International Journal of Photoenergy, 2015, 750846, 7, (2015).

[62] K. Tanaka, N. Moritake, and H. Uchiki, Preparation of Cu_2ZnSnS_4 thin films by sulfurizing sol-gel deposited precursors. Solar Energy Materials & Solar Cells, 91, 13, 1199–1201, (2007).

[63] J. J. Scragg, Studies of Cu_2ZnSnS_4 Films Prepared by Sulphurization of Electrodeposited Precursors, Ph.D. thesis, University of Bath, Department of Chemistry, Bath, (2010).

[64] M. Kauk, K. Muska, M. Altosaar, J. Raudoja, M. Pilvet, T. Varema, K.Timmo, O. Volobujev. Effects of sulphur and tin disulphide vapour treatments of $Cu_2ZnSnS(Se)_4$ absorber materials for monograin solar cells. Energy Procedia, 10, 197-202, (2011).

[65] A. Nagoya, R. Asahi, R. Wahl, G. Kresse. Defect formation and phase stability of Cu_2ZnSnS_4 photovoltaic material. Phys. Rev. B, 81, ID. 113202, (2010).

[66] S. Chen, X.G. Gong, A. Walsh, S.H. Wei. Defect physics of the kesterite thin-film solar cell absorber Cu_2ZnSnS_4. Appl. Phys. Lett., 96, ID 021902, (2010).

[67] I. Repins, N. Vora, C. Beall, S.-H. Wei, Y. Yan, M. Romero, G. Teeter, H. Du, B. To, M. Young and R. Noufi. Kesterites and Chalcopyrites: A Comparison of Close Cousins. MRS Online Proceedings Library, 1324, (2011).

[68] G. Teeter, H. Du, J.E. Leisch, M. Young, F. Yan, S. Johnston, P. Dippo, D. Kuciauskas, M. Romero, P. Newhouse, S. Asher, D. Ginley, Combinatorial study of thin-film Cu_2ZnSnS_4 synthesis via metal precursor sulphurization, in 35th IEEE-PVSEC, (2010).

[69] A. Weber, R. Mainz, H.W. Schock. On the Sn loss from thin films of the material system Cu–Zn–Sn–S in high vacuum. J. Appl. Phys., 107, (1), ID 013516, (2010).

[70] H. Yoo, J. Kim, L. Zhang, Curr. Sulphurization temperature effects on the growth of Cu_2ZnSnS_4 thin film. Appl. Phys. 12, (4), 1053-1057, (2012).

[71] A. Redinger, D.M. Berg, P.J. Dale, R. Djemour, L. Gutay, T. Eisenbarth, N. Valle, S. Siebentritt. Route Toward High-Efficiency Single-Phase CuZnSn(S, Se) Thin-Film Solar Cells: Model Experiments and Literature Review. IEEE J. Photovoltaics, 1, 200-206, (2011).

[72] A. Redinger, D.M. Berg, P.J. Dale, S. Siebentritt. The consequences of kesterite equilibria for efficient solar cells. J. Am. Chem. Soc. 16; 133 (10), 3320-3323, (2011).

[73] C. M. Fella, G. Ilari, A.R. Uhl, A. Chiril˘a, Y.E. Romanyuk, A.N. Tiwari, Non-vacuum deposition of $Cu_2ZnSnSe_4$ absorber layers for thin film solar cells, in 26 EUPVSEC, (2011).

[74] F. Biccari, R. Chierchia, M. Valentini, P. Mangiapane, E. Salza, C. Malerba, C.L.A. Ricardo, L. Mannarino, P. Scardi, A. Mittiga. Fabrication of Cu_2ZnSnS_4 solar cells by sulfurization of evaporated precursors. Energy Procedia 10, 187-191, (2011).

[75] S. Guha, D.B. Mitzi, T.K. Todorov, K. Wang. Annealing Thin Films. US Patent United States Patent Application, ID. 2012007093622, (2012).

[76] P. M. P. Salomé, J. Malaquias, P. A. Fernandes, M. S. Ferreira, J. P. Leitão, A. F. da Cunha, J. C. González, F. N. Matinaga, G. M. Ribeiro, E. R. Viana, The influence of hydrogen in the incorporation of Zn during the growth of Cu_2ZnSnS_4 thin films, Solar Energy Materials and Solar Cells, 95, 12, 3482-3489, (2011).

[77] K. Wang, B. Shin, K.B. Reuter, T. Todorov, D.B. Mitzi, S. Guha. Structural and elemental characterization of high efficiency Cu_2ZnSnS_4 solar cells. Appl. Phys. Lett. 98, (5), ID 051912, (2011).

[78] R. Juškėnas, S. Kanapeckaitė, V. Karpavičienė, Z. Mockus, V. Pakštas, A. Selskienė, R. Giraitis and G. Niaura. A two-step approach for electrochemical deposition of Cu–Zn–Sn and Se precursors for CZTSe solar cells. Solar Energy Mater. Solar Cells, 101, 277-282, (2012).

[79] I. D Olekseyuk. I.V Dudchak and L.V Piskach. Phase equilibria in the Cu_2S-ZnS-SnS_2 system. Journal of Alloys and Compounds, 368, (1-2), 135–143, (2004).

[80] T. Maeda, S. Nakamura and T. Wada. First-principles calculations of vacancy formation in In-free photovoltaic semiconductor $Cu_2ZnSnSe_4$. Thin Solid Films, 519, 21, 3, 7513–7516, (2011).

[81] A. Weber, Wachstum von Dünnschichten des Material systems Cu-Zn-Sn-S. PhD thesis, Friedrich-AlexanderUniversität Erlangen-Nürnberg, (2009).

[82] C. Malerba. Cu_2ZnSnS_4 thin films and solar cells:: material and device characterization. PhD thesis, University of Trento, (2014).

[83] P. S. McLeod, L. D. Partain, D. E. Sawyer and T. M. Peterson. Photoconductivity of sputtered Cu_xS films. Applied Physics Letters, 45, (4), 472–474, (1984).

[84] P. Lukashev, W. R. L. Lambrecht, T. Kotani and M. van Schilfgaarde. Electronic and crystal structure of $Cu_{2-x}S$: Full-potential electronic structure calculations. Physical Review B, 76, (19), ID 195202, (2007).

[85] A. Sanchez-Juarez and A. Ortíz. Effects of precursor concentration on the optical and electrical properties of Sn_xS_y thin films prepared by plasma-enhanced chemical vapour deposition. Semiconductor Science and Technology, 17, (9), 931, (2002).

[86] P. A. Fernandes, P. M. P. Salomé and A. F. da Cunha. A study of ternary Cu_2SnS_3 and Cu_3SnS_4 thin films prepared by sulfurizing stacked metal precursors. Journal of Physics D: Applied Physics, 43(21), ID 215403, (2010).

[87] M. Green, K. Emery, Y. Hishikawa, W. Warta, E. Dunlop. Solar cell efficiency tables (version 41). Prog. Photovolt Res Appl., 21, 1–11, (2013).

[88] P. Jackson, D. Hariskos, E. Lotter, S. Paetel, R. Wuerz, R. Menner, W. Wischmann, M Powalla. New world record efficiency for $Cu(In, Ga)Se_2$ thin-film solar cells beyond 20 %. Prog. Photovolt. Res Appl., 19, 894–897, (2011).

[89] S. Dongwan, L Sangwoo. Effect of sulfur and copper amounts in sol–gel precursor solution on the growth, crystal properties, and optical properties of Cu_2ZnSnS_4 films. J. Mater Sci. Mater Electron, 24, 3756–3763, (2013).

[90] C. T. Kumar, D. Tiwari. Earth-abundant non-toxic Cu_2ZnSnS_4 thin films by direct liquid coating from metal–thiourea precursor solution. Sol. Energy Mater. Sol. Cells, 101, 46–50, (2012).

[91] Y. Sun, K. Zong, H. Zheng, H. Wang, J. Liu, H. Yan, M. Zhu. Ethylene glycol-based dip coating route for the synthesis of Cu_2ZnSnS_4 thin film. Mater. Lett. 92, 195–197, (2013).

[92] H. Park, Y.H. Hwang, B.S. Bae. Sol–gel processed Cu_2ZnSnS_4 thin films for a photovoltaic absorber layer without sulphurization. J. Sol-Gel Sci. Technol. 65, 23–27, (2012).

[93] S. Chen, X.G. Gong, A. Walsh, S.H. We. Defect physics of the kesterite thin film solar cell absorber Cu_2ZnSnS_4. Appl. Phys. Lett. 96, ID 021902, (2010).

[94] H. Wang. Progress in thin film solar cells based on Cu_2ZnSnS_4. Int. J. Photoenergy, 2011, ID 801292, (2011).

[95] L Shnidman. The solubility of thiourea in water, methanol, and ethanol. J. Phys. Chem. 37, 693–700, (1932).

[96] J. M. Alía, H. G. M. Edwards, M. D. Stoev. A systematic FT-Raman spectroscopic study of twelve bis-thiourea complexes, $A(tu)_2B_2$ (A = Zn, Cd, Hg; B = Cl, Br, I, SCN). Spectrochim Acta A Mol Biomol Spectrosc. 55, 2423–2435, (1999).

[97] B. U. Maheshwari, S. V. Kumar. Synthesis and characterization of Cu_2ZnSnS_4 thin film by solution growth technique for the application of solar cell. Int. J. Adv. Renew Energy Res. 1, 448–451, (2012).

[98] P. A. Fernandes, P. M. P. Salomé, A. F. da Cunha. Study of polycrystalline Cu_2ZnSnS_4 films by Raman scattering, Journal of Alloys and Compounds, 509, 7600–7606, (2011).

[99] P. A. Fernandes, P. M. P. Salomé and A. F. da Cunha. Growth and Raman scattering characterization of Cu_2ZnSnS_4 thin films. Thin Solid Films, 517, 2519–2523, (2009).

[100] C. M. Sutter-Fella. Solution-processed kesterite absorbers for thin film solar cells. PhD Thesis. University of Erlangen-Nurnberg, (2014).

[101] V Vasu, A Subrahmanyam. Electrical and optical properties of sprayed SnO_2 films: dependence on the oxiding agent in the starting material. Thin Solid Films, 193–194, 973–980, (1990).

[102] R. P. Andres, R. S. Averback, W. L. Brown, L. E. Brus, W. A. Goddard III, A. Kaldor, S. G. Louie, M. Moscovits, P. S. Peercy, S. J. Riley, R. W. Siegel, F. Spaepen and Y. Wang. Research opportunities on clusters and cluster-assembled materials. Journal of Materials Research, 4, 03, 704-736, (1989).

[103] X. Zhang, G. Guo, C. Ji, K. Huang, C. Zha, Y. Wang, L. Shen, A. Gupta and N. Bao. Efficient Thermolysis Route to Monodisperse Cu_2ZnSnS_4 Nanocrystals with Controlled Shape and Structure. Scientific Reports, 4, 5086, (2014).

[104] L. Li, B. Zhang, M. Cao, Y. Sun, J. Jiang, P. Hu, Y. Shen and L. Wang. Facile synthesis of Cu_2ZnSnS_4 nanocrystals and its use for dye-sensitized solar cells applications. Journal of Alloys and Compounds, 551, 24–29, (2013).

[105] M. Edler, T. Rath, A. Schenk, A. Fischereder, W. Haas, M. Edler, B. Chernev, B. Kunert, F. Hofer, R. Resel and G. Trimmel. Copper zinc tin sulfide layers prepared from solution processable metal dithiocarbamate precursors. Materials Chemistry and Physics, 136, 582–588, (2012).

[106] P. Hiemenz and R. Rajagopalan. Principles of Colloid and Surface Chemistry, Marcel Dekker, New York, 3rd edn. 237–242, (1997).

[107] E. Carlino, S. Modesti, D. Furlanetto, M. Piccin, S. Rubini and A. Franciosi. Atomic resolution compositional analysis by scanning transmission electron microscopy high-angle annular dark-field imaging. Appl. Phys. Lett. 83, 662, (2003).

[108] T. Kato, H. Hiroi, N. Sakai, S. Muraoka and H. Sugimoto. Characterization of Front and Back Interfaces on Cu_2ZnSnS_4 Thin-Film Solar Cells. Proc. Of the 27th EU-PVSEC, 2236–2239, (2012).

[109] X. Lu, Z. Zhuang, Q. Peng and Y. Li, Chem. Wurtzite Cu_2ZnSnS_4 nanocrystals: a novel quaternary semiconductor. Chem. Commun. 47, 3141–3143, (2011).

[110] R. Mainz, A. Singh, S. Levcenko, M. Klaus, C. Genzel, K. M. Ryan and T. Unold. Phase-transition-driven growth of compound semiconductor crystals from ordered metastable nanorods. Nat. Commun, 5, 3133, (2014).

[111] Bruker-AXS, TOPAS Version 4, Karsrluhe, Germany, 2000, http://www.bruker-axs.com/topas.html.

[112] C. Malerba, F. Biccari, C. L. Azanza Ricardo, M. Valentini, R. Chierchia, M. Mller, A. Santoni, E. Esposito, P. Mangiapane, P. Scardi and A. Mittiga. CZTS stoichiometry effects on the band gap energy. Journal of Alloys and Compounds, 582, 528–534, (2014).

[113] H. Katagiri, K. Saitoh, T. Washio, H. Shinohara, T. Kurumadani and S. Miyajima. Development of thin film solar cell based on Cu_2ZnSnS_4 thin films. Solar Energy Materials and Solar Cells, 65, 141–148, (2001).

[114] C. A. Cattley, C. Cheng, S. M. Fairclough, L. M. Droessler, N. P. Young, J. H. Warner, J. M. Smith, H. E. Assender and A. A. R. Watt. Low temperature phase selective synthesis of Cu (2) Zn Sn S (4) quantum dots. Chem. Commun., 49, 3745–3747, (2013).

[115] N. Arul, D. Yun, D. Lee and T. Kim. Strong quantum confinement effects in kesterite Cu_2ZnSnS_4 nanospheres for organic optoelectronic cells. Nanoscale, 5, 11940–3, (2013).

[116] J. M. R. Tan, Y. H. Lee, S. Pedireddy, T. Baikie, X. Y. Ling and L. H. Wong. Understanding the Synthetic Pathway of Single Phase Quarternary Semiconductor using Surface-enhanced Raman Scattering: A Case of Wurtzite Cu_2ZnSnS_4 Nanoparticles. J. Am. Chem. Soc., 136, 6684–6692, (2014).

[117] A. Longo, L. Sciortino, F. Giannici and A. Martorana. Crossing the boundary between fcc and hcp: the structure of nanosized cobalt is unraveled by a model of size distribution, shape and stacking faults allowing simulation of XRD, XANES and EXAFS. Journal of Applied Crystallography, 47, 1562–1568, (2014).

[118] U. Ghorpade, M. Suryawanshi, S. W. Shin, K. Gurav, P. Patil, S. Pawar, C. W. Hong, J. H. Kim and S. Kolekar. Chem. Commun, 50, 11258–11273, (2014).

[119] M. Grossberg, J. Krustok, J. Raudoja, K. Timmo, M. Altosaar and T. Raadik. Photoluminescence and Raman study of Cu_2ZnSnS_4 monograins for photovoltaic applications. Thin Solid Films 519, (21), 7403–7406, (2011).

[120] K. Woo, Y. Kim and J. Moon. A non-toxic, solution-processed, earth abundant absorbing layer for thin-film solar cells. Energy Environ Sci. 5, (1,), 5340–5345, (2012).

[121] S. Chia-Ying, C. Chiu-Yen and T. Jyh-Ming. Cu_2ZnSnS_4 absorption layers with controlled phase purity. Scientific reports, 5, 9291, (2015).

[122] M. Abusnina, H. Moutinho, M. Al-Jassim, C. DeHart, and M. Matin. Fabrication and Characterization of CZTS Thin Films Prepared by the Sulfurization of RF-Sputtered Stacked Metal Precursors. Journal of Electronic Materials, 43, 9, 3145-3154, (2014).

[123] C. Y. Su, C. Y., Chiu, J. M. Ting. Cu_2ZnSnS_4 absorption layers with controlled phase purity. Scientific Reports, 5, 9291, (2015).

[124] J. Tauc, R. Grigorovici, A. Vancu. Optical properties and electronic structure of amorphous germanium. Phys. Status Solidi B, 15, 627, (1966).

Congress, schools and Publications

Congress and schools

- Determination of real area of contact and elastostatic friction for self-affine surfaces by means of the finite element method. Dr. Alessandro Rigazzi From: Institute of Computational Science, University of Lugano. DICAM. University of Trento. **15th May, 2015.**

- I-Flexis summer school: Flexible electronic sensors. Lille Grand Palais, France. May 15th, 2015.

- Spring 15: Reach, Out workshop on science communication. Thursday, Lille Grand Palais, France. May 14th, 2015

- **E-MRS 2015 Spring Meeting. (Oral presentation). 13th May.** Lille Grand Palais, France.

- Summer school: Carbon dioxide recovery. Sunday, May 10th, 2015. Lille Grand Palais, France.

- IEEE Italy Section School of Career Boosting. (DII). University of Trento. **February 09th-13th, 2015**

- **TOPAS – advanced modeling of diffraction data from polycrystalline materials.** (DICAM). University of Trento. **October 28-30th, 2014**

- *IX Workshop Italiano SOL-GEL Parma. (Oral presentation).* Dipartament of Chemistry**.** University of Parma. **June 17-18th, 2014.**

- School: AIC International School joined with 10th Paolo Giordano Orsini School. University of Trento, Italy, **September 15-20th, 2012.**

Publications:

1. Cristy L. Azanza Ricardo, Fabrizio Girardi, Elisa Cappelletto, **Renato D'Angelo**, Regina Ciancio, Elvino Carlino, Pier Carlo Ricci, Claudia Malerba, Alberto Mittiga, Rosa Di Maggio and Paolo Scardia. "Chloride-based route for monodisperse CZTS nanoparticles preparation". **Journal of Renewable and Sustainable Energy. 7, 043150 (2015); DOI: 10.1063/1.4929959** / **Accepted: 21 August 2015.**

2. **Renato D'Angelo**, Cristi Leonor Azanza Ricardo, Alberto Mittiga, Paolo Scardi and Matteo Leoni. "A water- and sulfurization-free solution route to $Cu_{2-x}Zn_{1+x}SnS_4$". **Journal of Sol-Gel Science Technology**. **DOI: 10.1007/s10971-014-3462-x**./ **Accepted: 28 July 2014.**